INTERFACIAL CHARGE RECOMBINATION AND ALTERNATIVE CHROMOPHORES RELEVANT TO DYE-SENSITIZED SOLAR CELLS

by

Erinn C. Brigham

A dissertation submitted to Johns Hopkins University in conformity with the requirements for the degree of Doctor of Philosophy in Chemistry

Baltimore, Maryland

June, 2015

Abstract

The need for cleaner and cheaper electricity and fuel drives this research into the fundamental electron transfer processes in dye-sensitized solar cell (DSSC) model systems. This thesis comprises the elucidation of the mechanism of interfacial charge recombination and the investigation of new, cheaper chromophores for DSSCs. The introduction explains the operating principles of DSSCs and covers specific topics that are useful in understanding the chapters that follow.

Chapter 2 explores interfacial charge recombination between electrons in nanocrystalline TiO_2 films and photo-oxidized molecular sensitizers anchored to the TiO_2. The order of the reaction in both electrons and oxidized sensitizers is established, allowing the rate law for recombination, $rate = k^*[TiO_2(e^-)]^n[S^+]^m$ to be written for the first time with experimental support for $m = n = 1$. The second order rate constant, k, was measured as 1.8 (±0.1) x $10^{12}\ \Gamma^{-1}s^{-1}$ at high $[S^+]$. A mechanism for recombination based on the data presented and previous reports is proposed. A pre-equilibrium where the hole and electron diffuse within their respective volumes until an encounter complex is formed, where upon electron transfer can occur. Because of this, the diffusion, the

electron transfer or both could control the rate depending upon the relative rates of diffusion and electron transfer.

Chapter 3 is an investigation of the extent to which each of the processes, diffusion and electron transfer, control the rate of recombination with a variety of forward applied biases. Applying a forward bias is one way to increase the rate of diffusion and increase the electron concentration, minimizing the contribution of diffusion to the overall rate of recombination. In order to test whether the electron transfer even had an influence on the rate, a series of sensitizers with a range of reduction potentials was tested. This change in driving force is expected to produce a difference in rate constants for electron transfer, according to the Marcus equation. In order to choose wavelengths to monitor charge recombination, the excited state and charge separate state difference spectra of $Ru(dcb)_2(CN)_2$, the Black Dye, N719, and YS12 were collected and are given herein. The kinetic data support driving force dependence with applied potentials of -200, -300, and -350 mV, but at -400 and -500 mV, the behavior changed. The reasons for this change is unclear, but it does seem that 1) electron transfer does contribute to the rate of recombination to oxidized sensitizers at potentials relevant to operating DSSCs and 2) there is a driving force dependence, although at very negative potentials other factors may become more influential.

Chapter 4 reports on the excited state electron transfer after light excitation of cob(I)alamin anchored to TiO_2. This is an important discovery on a fundamental level because excited state electron transfer has never before been observed from any cobalamin species. The reduction potentials of the cob(I)alamin are not suitable for application to traditional DSSCs, it does offer insight into the nature of the excited states that most efficiently inject into TiO_2, and it offers the opportunity for future study of charge recombination in the Marcus normal region under conditions of very negative applied potential, which emphasizes the contribution of the electron transfer to the rate.

Chapter 5 reports on a potential new organic, highly asymmetric porphyrinoid sensitizer called a phlorin. The sensitizer was evaluated with incident photon to current efficiency (IPCE) measurements, transient absorption in solution and anchored to TiO_2, and spectroelectrochemical measurement of the density of states in free energy of the phlorin reduction and oxidation, in addition to the TiO_2 acceptor states. It is proposed that an equilibrium exists between the electrons in the TiO_2 and the reduced phlorin, which has a very positive reduction potential. This equilibrium is at least part of the reason why the sensitizer has very low IPCE. In sum, it does not appear to be a promising sensitizer, but the large color changes that are possible in a

fairly small potential range might suggest it for use in electrochromic devices.

Thesis Committee: Professors Gerald J. Meyer (Advisor), Kenneth D. Karlin, and John D. Toscano

Acknowledgements

First, I would like to thank my advisor, Professor Gerald J. Meyer, for the wonderful opportunity to work in his lab, and for his patience and encouragement. Jerry was very kind to me in the face of unexpected illness, even though it kept me from lab work for some time. He had the generosity to gently correct my blunders, of which there were many, and to praise my accomplishments. Jerry always conveys that he believes in his students, through his words and his actions. Learning from him and his brilliant students has been an amazing experience.

I would also like to thank Professor Kenneth D. Karlin, or as he's known in the chemical hood, Kenny Danger, King of Copper. Thank you for being very understanding and supportive, giving excellent advice, reminding me of the importance of A+B → C+D, and for mentoring my mentors, Suzanne Sherman and Jerry.

I cannot go any longer without thanking my parents, Marika and Peter Matthew Brigham. I can feel there influence in every success I have ever had, and it's fair to say that I owe them everything twice over. They are the best parents I could possibly dream of, and I am forever grateful for their sacrifices and support. I can't even begin to estimate how many times I've told my mother about this or that experiment, and heard her encouragement in return. Neither could I estimate how many emails I have from my father about some new solar technology. As it turns out, he doesn't really care about solar, he's just that supportive. Thank you both for always being there for me, and for being the hardest act to follow that I've ever seen.

My brother, Eric Brigham, has a special function in my motivation: I cannot disappoint him; that would be completely unbearable.

The steadfast belief in me and my abilities of my partner and fellow data analysis junkie, Ingmar T. Gorman, has been a powerful force keeping me on track. Working alongside Ingmar pushed me to work longer and harder than I would have otherwise. Thank you for your encouragement, support, and understanding.

Close friends are the pillars of everyone's lives, and I have some sturdy ones: Danielle Wohlgemuth, Leah Burger, Leland Widger, Sarah O'Connor, Ryan Oliver, Katriana Nugent, Shane "Booger" Danner, Eric Hill, and Kekoa Tepara….thank you for keeping me sane these past few years. I could not have done this without you. I love you all.

My housemates in Chapel Hill made me feel at home when I could have felt like a stranger in a strange land. Thank you Greg Wells, Maria

Lindell, Colleen O’Neill, Mark Moog, and Erin Wilson for being great to party, laze around, rock climb, commiserate, and hash out science problems with. Particularly, thanks to Maria and Colleen for cooking me dinner so many times. You will all kick life’s butt.

My mentors in the lab, Darren, Atefeh, Patrik, and Ke all contributed significantly to my training, and I am eternally grateful for their time, effort, and expertise. Ryan, by virtue of working in his own room, escaped my questions until we moved to UNC, which brought us all closer together. All of my lab mates, Professor Darren Achey, Dr. Atefeh Taheri, Dr. Patrik Johansson, Dr. William Ward, Dr. Byron Farnum, Dr. Ryan O’Donnell, Dr. Ke Hu, Dr. Renato Sampaio, Evan Beauvilliers, Timothy Barr, Brian DiMarco, Tyler Motley, Wesley Swords, Dr. Cassandra Ward, Dr. Guocan Li, Tilden Hagan, Eric Piechota, Catherine Burton, and Andrew Maurer have special places in my heart. You are amazing people and scientists with bright futures. I will miss every one of you.

Table of Contents

List of Tables

List of Figures

List of Schemes

List of Equations

Chapter 1. Introduction

1.1 Energy Demands & the Case for Solar Technologies

Global energy demand is increasing with increasing human population and societal industrialization. Regardless of concerns about running out of fossil fuels, the environmental and health effects of using fossil fuels[1] exclusively to satisfy new energy demands are likely to be very costly.[2] Each alternative energy technology has advantages and disadvantages, but all of them are side-effects of the light from the sun irradiating the Earth, with the exceptions of nuclear and geothermal. The surface of the Earth is bombarded by sunlight at a rate of 174,000 TW. For perspective, the global energy consumption rate in 2001 was 13.5 TW, and the rates in 2050 and 2100 are estimated to be 27.6 and 43, respectively.[3] Although sunlight is not evenly distributed over the Earth's surface, it is more evenly distributed than fossil fuels.[4]

Economic opportunities are another incentive to develop renewable energy technologies that can be used in isolated locations with no grid access, or on the grid in residential, commercial, and utility contexts. The valuation of the global market for solar energy installations is shown for the 2000-2013 time period in Figure 1.1. Rapid growth was seen in the 13 year period, and growth is expected to continue for decades.[5]

There are several solar and wind technologies that have reached grid parity with fossil fuel energy sources (in some areas),[6] so now the basic research challenge is to make technologies that are even cheaper than fossil fuels without additional subsidization.

Silicon production and purification has been made much less expensive by extensive use of the material in sophisticated electronics, but silicon still needs to be purified to very high purity for use in solar cells. If a cheaper and/or more efficient option were developed, it would be a breakthrough in an economic sense as well as an environmental sense.

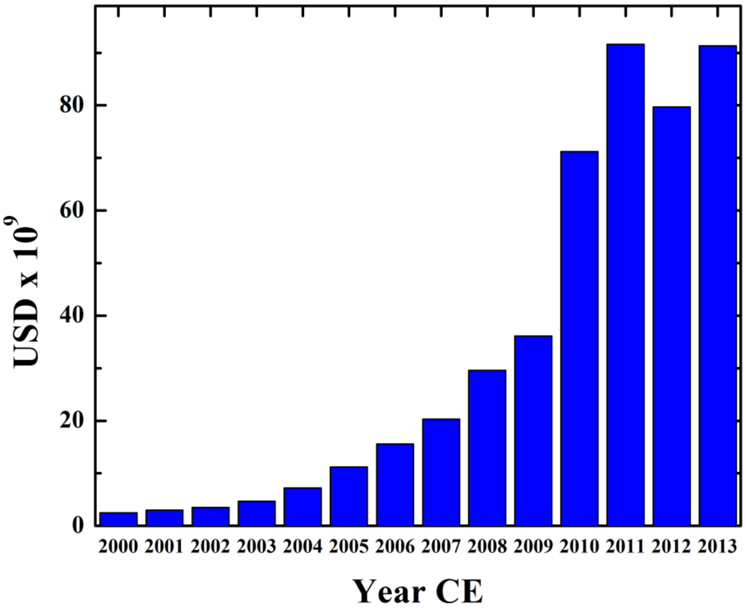

Figure 1.1 Global solar energy market value. Data taken from 2014 report by Clean Edge.[5]

The certified efficiencies of major types of photovoltaics are plotted versus time in Figure 1.2. There are several areas of interest outside silicon-based technologies. The type of cell that has most rapidly improved in recent years is the perovskite solar cell (red circles with yellow fill), so named for the structure of their lead-halide based crystal structure. However, stability is still currently a problem for these devices. Another type of interest is the tandem cell, which uses multiple junctions to absorb more of the solar spectrum. They are generally highly efficient under very high irradiance; therefore, they are best used in solar concentrator farms, which minimize the amount of expensive material used to fabricate the tandem devices. Recently, four junction tandem cells were certified at 46% efficiency under concentrated irradiation.[7]

High efficiency is not the only way to make marketable solar cells. Lower efficiency but cheaper cells could also have a niche, particularly if they can be utilized in new contexts. In the lower efficiency portion of Figure 1.2, the dye-sensitized solar cell (DSSC) is shown in open orange circles. These cells have the potential to be cheaper than silicon-based modules with the added benefit that they can be made translucent (for use in buildings as windows, for example) or flexible with relative ease.

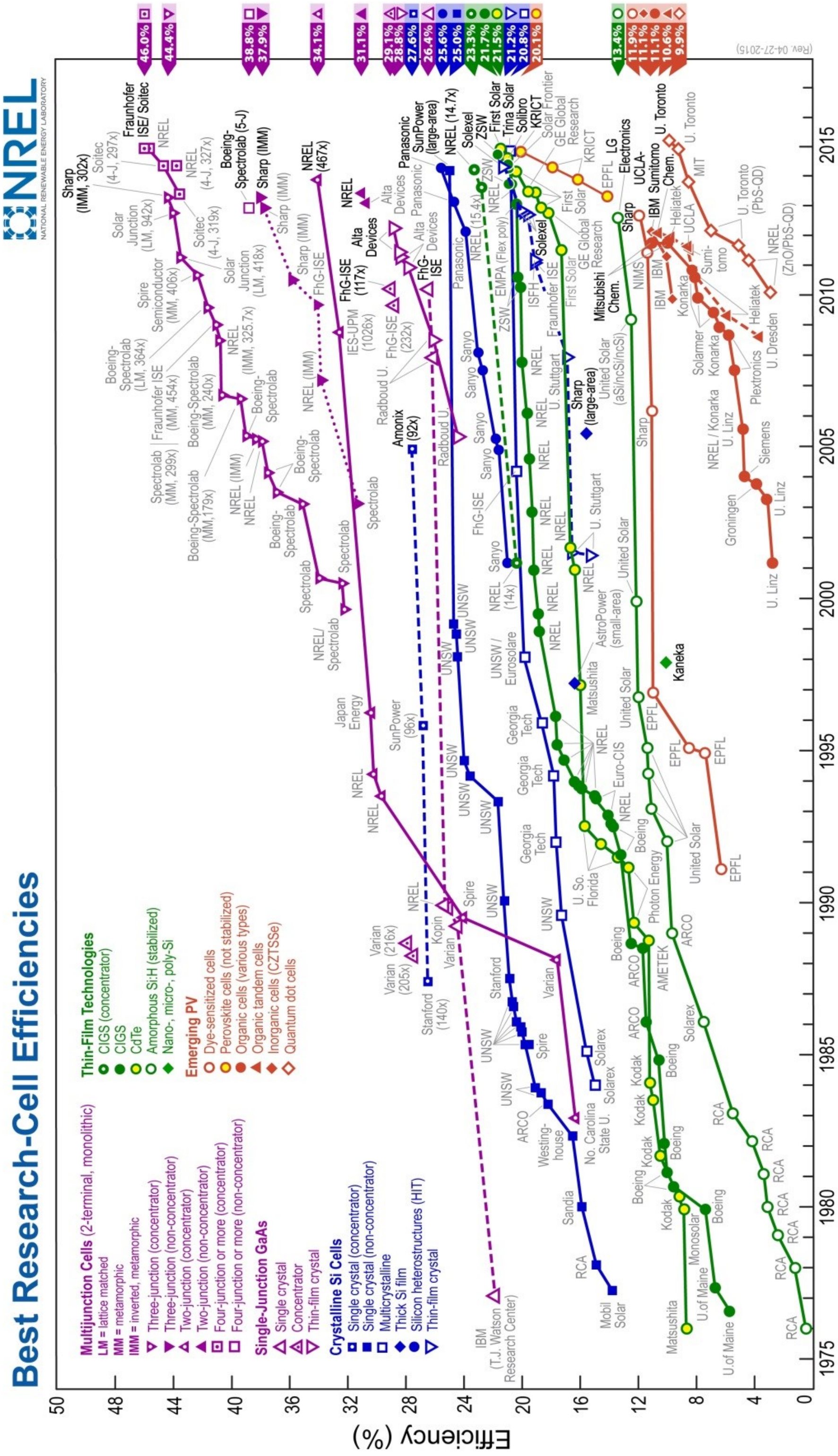

Figure 1.2 The National Renewable Energy Laboratory certified efficiency of various solar cell types. This plot is courtesy of the National Renewable Energy Laboratory, Golden, CO.

1.2 Dye-Sensitized Solar Cells

The defining characteristic of the DSSC is that it employs a wide band gap semiconductor that is sensitized to visible light by molecular dyes, which are typically anchored to the surface of the semiconductor. In the early days of study, DSSCs were an object of fundamental interest, but they emerged as a promising technology for solar to electrical energy conversion in the early 1990s. Brian O'Regan and Michael Grätzel combined their expertise in mesoporous TiO_2 and ruthenium sensitizers, respectively, to create the first modern DSSC in 1988,[8] published an exploratory paper in 1990,[9] and the seminal paper on the first high efficiency cell in 1991.[10] Prior to their breakthrough, DSSCs were based on planar TiO_2 electrodes, which limited the surface area on which sensitizers could bind. Their breakthrough came because using mesoporous instead of planar TiO_2 gave rise to an increase in surface area of approximately 1000 fold. The increase in surface area for anchoring sensitizers allowed increased light absorption and overall efficiency. The next few pages are dedicated to an explanation of the operating principles of DSSCs, and more specific discussions of the aspects of the DSSC that are most relevant to this dissertation follow.

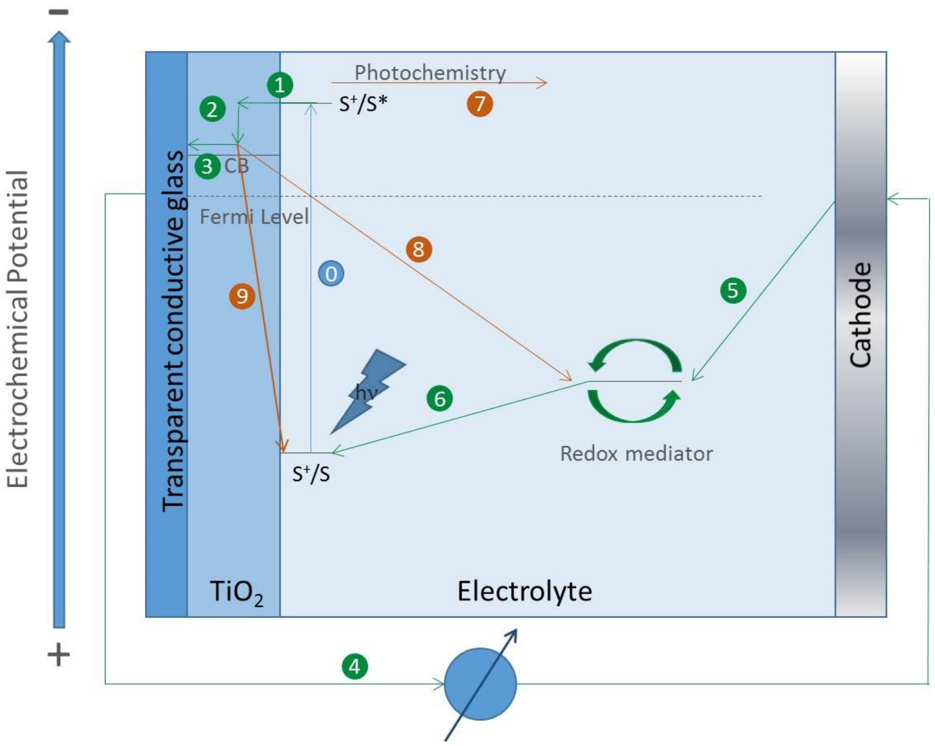

Scheme 1.1 The major photoelectrochemical processes in the DSSC are shown. Light absorption is shown in blue. Green arrows denote favorable electron transfer (ET) processes, and detrimental ET processes are shown in red. An explanation of each step can be found in the main text.

Scheme 1.1 depicts the DSSC in potential space (vertical) and physical space (horizontal, not to scale). In the scheme, light is absorbed by a sensitizer (S, step 0), and in the excited state, S*, the sensitizer injects an electron into the acceptor states of TiO_2 (step 1). The injected electron thermalizes (2) and diffuses through the TiO_2 to the conductive glass electrode (3). The electron travels through an external circuit (4), doing some useful work, and at the cathode the electron reduces a redox mediator in solution (5). The reduced redox mediator travels through the electrolyte to the photoanode and reduces the oxidized sensitizer (6).

Ideally, there is no net chemical change once the entire sequence is complete, so the DSSC is referred to as a regenerative cell.

Several unwanted elementary reactions disrupt the desired flow of electrons. Some of these processes are represented in Scheme 1.1 by numbered red arrows. After excitation from the ground state, the sensitizer is not restricted only to injection of an electron to dissipate the added energy. In addition, it could undergo radiative and non-radiative decay (not shown), and it could undergo photochemical reactions (7). These photochemical reactions primarily go through activation to ligand field states that facilitate ligand loss. The likelihood of ligand loss is related to the energy barrier to accessing the ligand field states, which depends upon the specific character of metal-ligand bonding in the complex.[11]

If the electron is injected, the alternatives to migration to the external circuit (3) include interfacial recombination to species in solution (e.g. the oxidized redox mediator, 8) or to the surface-anchored oxidized sensitizer (9). Gaining deeper mechanistic understanding of the latter recombination process is a main goal of this dissertation, but some aspects of the DSSC should be explained further before proceeding.

1.3 Mesoporous Anatase TiO_2 Nanocrystallite Films

A representative sample of the breakthrough material, mesoporous, nanocrystalline anatase-TiO_2, is shown in Figure 1.3. As synthesized by a sol-gel method in the G. J. Meyer lab, the nanocrystallites are ~10-20 nm in diameter, and are roughly spherical. The aqueous nanocrystallite suspension is mixed with an organic polymer and doctor bladed or screen printed onto the transparent conductive oxide, followed by sintering at high temperature. The image taken by scanning electron microscopy, Figure 1.3, shows the resulting porosity, which has been estimated to be approximately 50%. In this dissertation, the doctor blading technique was used, which resulted in films approximately 10 µm thick.

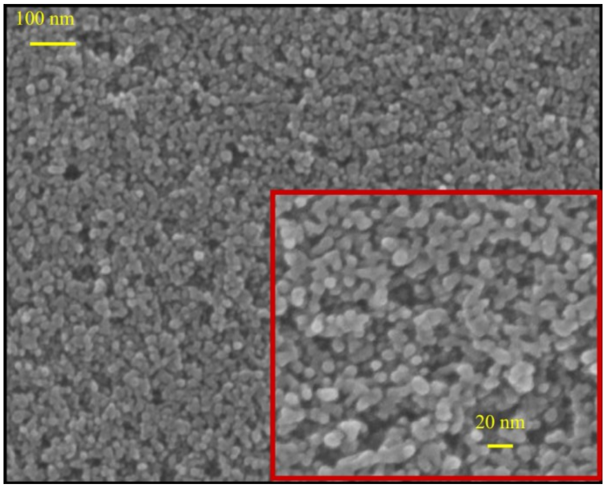

Figure 1.3 A scanning electron microscopic image of a thin film of TiO_2 nanocrystallites.

These films can be characterized spectroelectrochemically to measure the concentration and energy level of the electron acceptor states. A density of states in free energy like that shown in Figure 1.4 is the result.

The chemical capacitance (horizontal axis) is calculated from the absorbance of the electrons in the range of 800-1000 nm at each potential, which reflects the number of TiO_2 acceptor states that are filled by an electron.[12] If one assumes that the electrons are evenly distributed in space and the film thickness and porosity are known, then the 'concentration' of electrons can be calculated from the absorbance as well.[13]

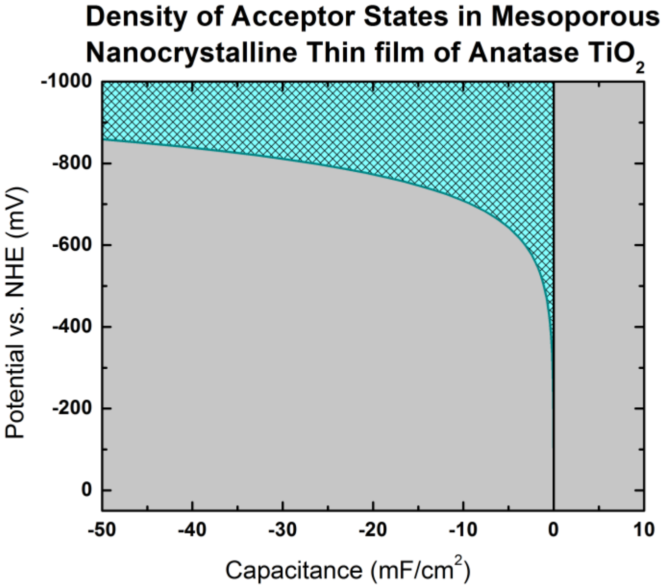

Figure 1.4 The density of acceptor states in free energy of a mesoporous thin film of nanocrystalline TiO_2 as a function of applied potential.

The electron transport in TiO_2 is also of importance in understanding interfacial charge recombination, and has been conceived of in many ways. Several of the most influential models of electron transport as it relates to recombination are summarized briefly below:

- Multiple trapping (MT): Hagfeldt, Boschloo, Walker, Peter,[14] Reynolds[15]
    - Based on the work of Scher and Montroll[16] in their description of the dispersive kinetics of electron transport in highly disordered materials.
    - Transfer occurs through extended states at the conduction band edge (E_{cb})
    - Uses chemical diffusion coefficient D_n, diffusion length, and electron lifetime to model transport and recombination.
    - The diffusion coefficient for free electron transport D_0 is reduced to D_n by multiple trapping and detrapping events.
- Reinterpretation of MT: Bisquert[17–19]
    - Trap states are localized
    - D_n calculated using hopping model
    - Transfer occurs from the transport level (E_{tr}) and $E_{tr} < E_{cb}$
- Reinterpretation of MT: Katoh and Furube[20]
    - Recombination can occur from trap states
    - Differences in ΔG of recombination between different trap states is neglected

  - Majority of traps assumed to be on or near the surface of the nanoparticle
  - "Random flight" of electron:[21] once electron has been activated it can be trapped by any vacant site in the nanoparticle with equal likelihood
- Continuous-time random walk (CTRW): Jenny Nelson, Haque, Durrant[22]
  - Transfer only to nearest neighbor sites on a regular cubic lattice with each site having trap energy E drawn from the distribution g(E), giving each a corresponding frequency of activation.
  - Attempts to justify the use of the stretched exponential Kohlrausch-Williams-Watts (KWW) function in fitting recombination kinetics by using a distribution of waiting times which is representative of the energetic and/or configurational disorder of the electrons in TiO_2.
  - Electric fields neglected, only electrons can diffuse (not holes); motion of "untrapped" carriers is neglected because they are few. Neglects recombination with defects and the electrolyte.
  - If CTRW were to use the Miller-Abrahams jump rates, then CTRW would be very similar to MT

These models are important context for the section 1.5 Interfacial Charge Recombination. Next, the molecular aspect of the interface is considered.

1.4 Chromophores

The intense color of transition metal compounds can be exploited for solar energy conversion applications. Metal-to-ligand or ligand-to-metal charge transfer (MLCT or LMCT) absorption bands have greater extinction coefficients than do the metal-centered d-d bands,[23,24] so these transitions are typically more competent solar light harvesters [24–26]. Compounds with LMCT excited states are often found to be unstable and undergo ligand loss photochemistry,[27] which limits their practical utility. On the other hand, compounds with MLCT excited states have been used extensively for light-harvesting in dye-sensitized solar cells and in artificial photosynthetic assemblies [28–33]. In this role, the transition metal compound serves to absorb light, and then initiate electron transfer reactions that may result in transiently stored free energy, generated electrical power, and/or chemical fuels. In a typical MLCT transition, light absorption promotes a dπ electron from the metal to a low-lying π* orbital of a ligand (Equation 1.1) [24].

$$[d\pi]^n[\pi^*]^0 \rightarrow [d\pi]^{n-1}[\pi^*]^1 \qquad 1.1$$

The classic example is $Ru(bpy)_3^{2+}$, where bpy is 2,2'-bipyridine, which is possibly the most well characterized transition metal compound in the world [30,34–42]. A variety of other $d\pi^6$ transition metals, in particular Re(I), Ir(III), and Os(II), also have well characterized MLCT excited states useful for solar energy conversion.[43–51] One desirable characteristic of these compounds is that they frequently have a high quantum yield for excited state electron transfer. Additionally, they generally display high stability in the ground and the MLCT excited states,[52] as well as in their one-electron reduced and/or oxidized forms. However, the scarcity and expense of these precious metals is disadvantageous for large-scale applications.

There is considerable interest in developing first row transition metal compounds for applications in solar energy conversion.[53] A logical choice would be Fe(II) polypyridyl compounds that also have a $d\pi^6$ electronic configuration.[54–59] However, in spite of many attempts, iron compounds have performed very poorly in artificial photosynthetic assemblies relative to their Ru(II) counterparts. The ~ 30% smaller crystal field splitting energy of Fe relative to Ru results in the unfilled Fe d-orbitals being the lowest lying electronic excited states.[23,60,61] Internal conversion or intersystem crossing from the MLCT to the d-d (often called ligand field states) is quantitative (Equation 1.2). Since the ligand field states are anti-bonding with respect to metal-ligand bonds, their population leads to ligand loss photochemistry and/or rapid excited state relaxation.[62]

$$[t_{2g}]^5[\pi^*]^1 \rightarrow [t_{2g}]^5[e_g{}^*]^1 \qquad 1.2$$

Interestingly, the same general photochemical behavior is observed with hemes, where the π→π* excited states of the porphyrin are rapidly quenched by the iron ligand field states. Indeed, to our knowledge all first row transition metal compounds with unfilled d-orbitals are essentially non-emissive with short excited state lifetimes, behavior that is generally attributed to the presence of low-lying ligand-field states.[62,63] For this reason, many experimentalists have turned to $d\pi^{10}$ transition metal compounds such as Cu(I), where excited state deactivation through this pathway is not possible. Lazorski[64] and Bozic-Weber[53] together provide a thorough review of the development of Cu(I) sensitizers. Likewise, Zn(II) compounds have a $d\pi^{10}$ electronic configuration and are also of interest as they do not quench the π→π* excited states of organic macrocycles.[65–67]

In recent years, it has been discovered that several cobalt (I) compounds broadly absorb visible light and initiate efficient excited state electron transfer reactions [68–70]. Such compounds have long been known to possess MLCT excited states, but photo-induced electron transfer reactivity was not investigated, presumably because low-lying ligand field states were expected for these $d\pi^8$ coordination compounds. A novel feature of oxidative quenching of these excited states is that the Co(II) product adopts a different geometry and coordination number than does the Co(I) compound that was initially photo-excited [71,72]. This property is absent in most light-absorbing second and third row metal compounds that generally remain octahedral or pseudo-octahedral. It may be possible to exploit this structural change to inhibit unwanted recombination reactions in artificial photosynthetic assemblies, and there already exists some evidence that this is the case [73]. In addition, electron transfer reactions with large inner-sphere reorganization energy changes are of interest in their own right. Chapter 4 will elaborate on some if these sensitizers.

Although metal-based sensitizers have many fine qualities, attempting to design organic sensitizers is of merit because they do not contain rare or expensive elements, and are frequently less toxic. Extended conjugation with broad light absorption is not enough though; the excited state must be of the right energy to inject electrons into the semiconductor acceptor states, and the oxidized state must be at the appropriate potential to oxidize an appropriate redox mediator with minimal loss in V_{oc}. This set of criteria has led to the use of porphyrins with modifications to allow increased breadth of absorption.[74–76] This will be elaborated upon in Chapter 5.

1.5 Interfacial Charge Recombination

Interfacial charge recombination, where injected electrons flow in the undesired direction (8 and 9 in Scheme 1.1), is one of the sources of efficiency losses in DSSCs and dye-sensitizer photoelectrosynthesis cells (DSPECs). There are two main charge recombination processes: electrons are transferred from TiO_2 to either oxidized redox mediator (Equation 1.3) or to the oxidized sensitizer (Equation 1.4).

$$TiO_2(e^-) + \mathrm{O} \rightarrow TiO_2 + \mathrm{R} \tag{1.3}$$

$$TiO_2(e^-)|S^+ \rightarrow TiO_2|S \tag{1.4}$$

Both processes have been studied thoroughly, but the second will be elaborated upon more fully as it is a main topic of this dissertation research.

1.5.1 Recombination to Oxidized Sensitizers

Fortunately for the developers of DSSCs, the rate constants for recombination to oxidized sensitizers are typically very small in comparison to the rate constants for injection, which allows a DSSC to function as a photovoltaic.[77] In general, the electron recombination reaction is of much greater significance for DSPECs than for DSSCs, as many desirable catalytic reactions require the accumulation of multiple charges, and each successive charge transfer brings with it a greater driving force, and possibly coulombic attraction, for recombination [32,78,79].

1.5.1.1 ***Driving Force vs. Electron Diffusion Dependence***

The rate of any reaction with more than one reactant is controlled either by the diffusion of the reactants, or by the reaction after diffusion. In the case of recombination, the diffusion involves charge hopping on the surface from sensitizer to sensitizer[79,80] and diffusion of electrons within the nanoparticles (Equation 1.5), while the reaction after diffusion is electron transfer in the pre-formed, ill-defined encounter complex of the electron and oxidized sensitizer (Equation 1.6). One or the other can control the rate of recombination or the control can be intermediate.

$$TiO_2(e^-) + S^+ \rightleftharpoons [TiO_2(e^-)|S^+] \tag{1.5}$$

$$[TiO_2(e^-)|S^+] \rightarrow TiO_2|S \tag{1.6}$$

There are several conflicting models of interfacial charge recombination to oxidized sensitizers. Despite their complexity, the models can be roughly divided into two of the categories above: controlled by electron transport (Equation 1.5) or interfacial charge transfer (Equation 1.6).

In the interfacial transfer-limited case, transport is unimportant and the rate constant for charge recombination, k_{cr}, depends only on the terms of the Marcus equation for electron transfer, Equation 1.7.[77]

$$k_{et} = \frac{H_{AB}^2}{\sqrt{4\pi\lambda k_B T}} e^{\frac{-(\Delta G^0 + \lambda)^2}{4\lambda k_B T}} \tag{1.7}$$

Thus, the terms of importance are the electronic overlap (H_{AB}, which in turn depends on the distance), the reorganization energy (λ), the temperature (T), and the change in Gibbs free energy for the transfer (ΔG^0). Some of these aspects have been investigated,[81] and the effect of the change in Gibbs free energy is contested. Most researchers believe recombination to common sensitizers resides deep in the Marcus inverted region, which could help explain the fortuitous sluggishness of charge recombination.

The case of electron transport limited recombination is much less straightforward than that of interfacial transfer limited recombination. In the electron transport limited case, we must consider the characteristics of the acceptor states in the semiconductor. There is a good deal of contention in the literature over how to consider and model these states.[82–86]

A number of research groups have reported observing driving force dependence in the rate of recombination.[87–89] Meanwhile, a number of notable research groups have reported that the diffusion of electrons is likely the controlling factor.[13,90–94] Furthermore, the ability to move between domains of control has been reported.[89] Chapters 2 and 3 will address this further. Some particular cases are described below.

1.5.1.2 ***Effect of Applied Potential***

The effect of applied potential on the recombination dynamics in DSSC model systems was first reported by Haque et al. in 1998.[90] The behavior of DSSCs under the condition of applied negative bias is of interest because in the operational DSSC, the Fermi level is raised due to the constant irradiation. Raising the Fermi level electrochemically allowed a way to model the electron occupancy under operating conditions but also used time-resolved spectroscopic techniques. “Light bias,” where a constant source of irradiation is used in addition to the transient excitation beam, has also been used for the same purpose, and has many merits.

In general, the effect of increased negative bias on recombination is a super-linear increase in the rate constant for recombination with respect to both electron occupancy and applied potential, and a decrease in initial amplitude (at ~10 ns), which could reflect increased recombination before the instrument response time and/or decreased injection into TiO_2.[13,68,90–92,95–97]

Specifically, the results of Haque et al. are shown in Figure 1.5, with analysis by Nelson.[92] The effects on both dynamics and initial amplitude can be seen. On the right, the power law dependence of the time at which 50% of the recombination has occurred, $t_{50\%}$, on the ratio, n, of electrons to oxidized ruthenium-based sensitizers (termed “cations” in the figure) is shown on a log-log scale.

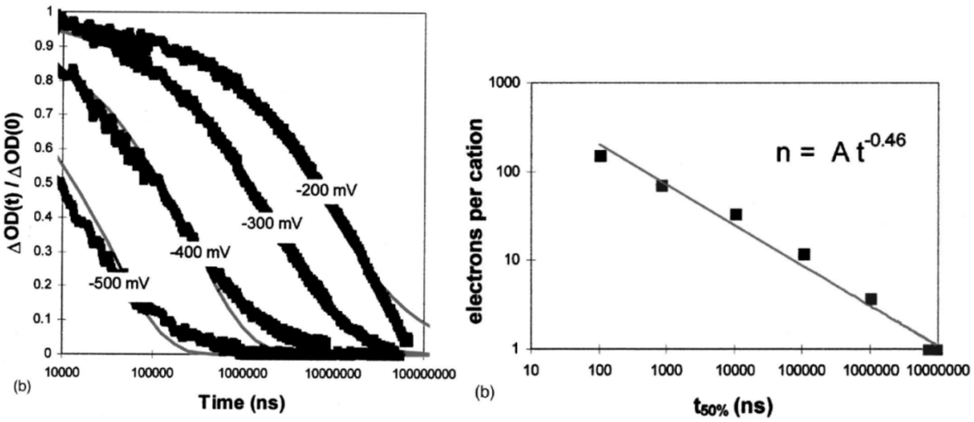

Figure 1.5 On the right, the change in absorbance over time after pulsed laser excitation of $TiO_2|S$ in $LiClO_4$ CH_3CN electrolyte. The kinetic data reflects the $TiO_2(e^-)|S^+ \rightarrow TiO_2|S$ recombination reaction at the indicated applied biases vs. Ag/AgCl. On the right, the $t_{50\%}$ of the same data is shown as a function of the ratio, n, of electrons to oxidized sensitizers ("cations"). The data is fit to a power function with the parameters shown. This figure was adapted with permission from Nelson *et al.*[92]

Recombination in typical DSSCs with ruthenium-based sensitizers is thought to lie in the Marcus inverted region, where the increase in driving force for recombination would be expected to slow the reaction if electron transfer was the rate-limiting step.[13,87,98–100] In contrast, Co(I) sensitizers have sufficiently negative reduction potentials that recombination to them is in the Marcus normal region. In the cases of cobyrinate and a cobalt porphyrin (CoP), the applied potential was varied and the lifetime of the $TiO_2(e^-)|Co(II)$ charge separated state was abstracted from fits of the change in absorbance at 410 nm.[68] Figure 1.6 A and B display the change in absorbance of $TiO_2|Co(I)P$ with various applied potentials at 410 nm, indicative of Co(II), as a function of delay time.

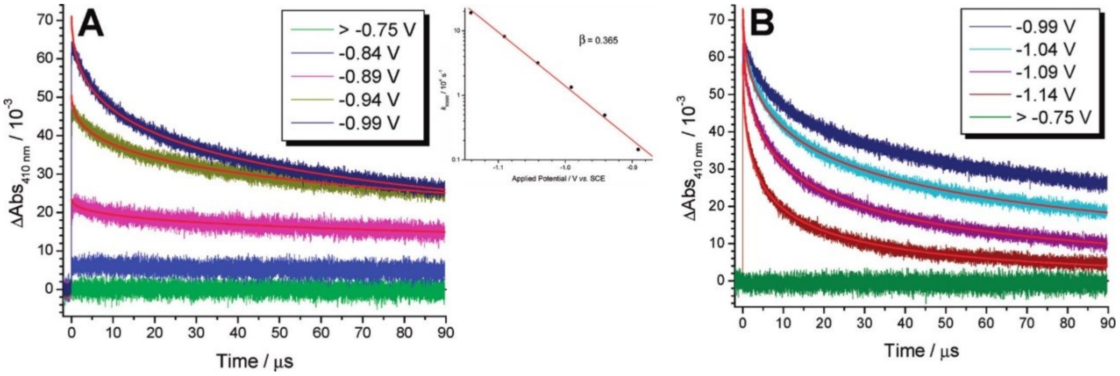

Figure 1.6 A) The change in absorbance at 410 nm after 532 nm pulsed laser excitation of $TiO_2|Co(I)P$ at the indicated applied potentials *vs.* SCE. B) The continuation of part A with more negative applied potentials. Overlaid in red are fits to Equation 1.13 (see section 1.5.1.4) with β = 0.365. Inset: the inverse of the lifetimes ($1/\tau$ = k) on a log scale as a function of applied negative potential. Reproduced from Brigham *et al.* [101]

At potentials where the sensitizer was in the Co(II) state (-750 mV *vs.* SCE), no evidence for excited state injection was observed. An increasingly negative applied bias elevated the concentration of Co(I) and hence the injection yield (Figure 1.6A). As the applied potential became more negative than -990 mV *vs.* SCE (Figure 1.6B), the initial change in absorbance remained near constant as essentially all of the cobalt compounds were reduced to the formal oxidation state of I, while the lifetime of the charge-separated state decreased exponentially (inset). Similar effects were observed with cobyrinic acid heptamethyl ester.[69]

Further study of the recombination kinetics of a larger family of compounds where the Co(II/I) reduction potentials were systematically varied could lead to a better understanding of the kinetics of interfacial electron transfer from TiO_2 to anchored molecules and electron diffusion in TiO_2. Ruthenium sensitizers are generally substitutionally inert octahedral coordination compounds, so tuning the reduction potentials is usually accomplished by structural and electronic perturbations of the ligands. This often requires relatively complicated synthetic and purification procedures. In comparison, the Co(II/I)P formal reduction potential was tuned by 130 mV through the simple addition of pyridine to the electrolyte solution.[73] As additional substitutionally labile sensitizers based on first-row metals are developed, this facile tunability could prove to be a useful tool in controlling electron recombination through interfacial energetics.

1.5.1.3 ***Distance Dependence***

The distance dependence of charge recombination has been investigated.[88,94,95,102–104] When the electron in TiO_2 was forced to travel further through space to recombine with the hole on the oxidized sensitizer, the recombination was considerably slower. In some cases it was found that excited state injection was also slower, with a decrease in injection yield.[104]

1.5.1.4 ***Mathematical Fitting Functions***

Kinetic data for recombination has been fit in a variety of way, each with its own merits and defects. Below, the Kohlrausch Williams-Watts stretched exponential, sums of exponentials, and the bi-second-order equal concentration model are discussed with references for examples and origins.

1.5.1.4.1 *Sum of Exponential Functions*

The earliest attempts at quantifying charge recombination to oxidized sensitizers at the interface of mesoporous nanocrystalline semiconducting particles and molecular sensitizers utilized sums of exponential functions,[105] and some recent researchers take this approach as well.[106] The potential advantage to this approach is that, theoretically, one could separate different types of recombination and quantify each process separately, allowing the separate comparison of each under various conditions. This is an extremely attractive option, but it is questionable whether the designation of types is meaningful. Furthermore, it has been shown that this type of analysis is of limited value when the concentration is not accounted for,[100] as has been done recently.[106]

1.5.1.4.2 *Bi-Second-Order Equal Concentration Kinetic Model*

The most satisfying approach that has been used was based on second-order equal concentration kinetics, Equation 1.8.[107]

$$\frac{d[S^+]}{dt} = -k[S^+][e^-] = -k[S^+]^2 \qquad 1.8$$

Because the oxidized sensitizer concentration, [S^+], is linearly related to the absorbance of the sensitized thin film, the integrated (and rearranged) form of Equation 1.8 can be represented by Equation 1.9,[93] where A refers to the change in absorbance, Δε refers to the change in molar extinction associated with oxidation of the sensitizer, and

$$\Delta A = \frac{A}{1 + Ak\Delta\varepsilon dt} \qquad 1.9$$

However, reported data has never been ideal enough to be fit by one of these equal concentration terms, so a sum of two terms was introduced,[93] with the explanation that there are at least two populations with two rate constants of reaction, Equation 1.10.

$$\Delta A = \frac{A_1}{1 + A_1 k_1 \Delta\varepsilon dt} + \frac{A_2}{1 + A_2 k_2 \Delta\varepsilon dt} \qquad 1.10$$

This model has been used by several notable research groups since its introduction.[87,99]

1.5.1.4.3 ***Kohlrausch Williams-Watts Stretched Exponential Function***

Rudolf Kohlrausch introduced the stretched exponential function (Equation 1.11) in 1854 as an empirical relation to describe the discharge of a Leiden Jar, which was an early capacitor.[108,109]

$$f(\beta, t) = e^{-t^{\beta}} \qquad 1.11$$

Since then, the stretched exponential function has been used in modeling many relaxation phenomena. Most relevant to the present discussion, Graham Williams and David C. Watts described a similar function (Equation 1.12) to model non-symmetrical α-relaxation in polymers,[110] which was also derived by Scher and Montroll several years later to describe charge transport in amorphous solids.[16] This stretched exponential function is commonly referred to as the Kohlrausch Williams-Watts function (KWW).

$$\gamma(\beta, t, \tau_0) = e^{-\left(\frac{t}{\tau_0}\right)^{\beta}} \qquad 1.12$$

Adapted to transient absorption data, the equation becomes Equation 1.13, where ΔA is the change in absorbance and A_0 is the initial amplitude of the absorbance change.

$$\Delta A(\beta, t, \tau_0) = A_0 \cdot e^{-\left(\frac{t}{\tau_0}\right)^{\beta}} \qquad 1.13$$

In both Kohlrausch's and the KWW equations, $0 < \beta \leq 1$ and t is time. In the Williams-Watts expression, a time constant, τ_0, is introduced. However, the τ_0 term cannot be used directly as a lifetime. Although β gives rise to a non-symmetrical distribution of lifetimes, it is possible to obtain an average lifetime (‹τ›, Equation 1.14) without explicit knowledge of the distribution.[111]

$$\langle\tau\rangle = \frac{\tau_0}{\beta} \cdot \Gamma\left(\frac{1}{\beta}\right) \qquad 1.14$$

Fitting kinetic data with the stretched exponential is very sensitize to a number of factors, including the time range of the data, the point at which t = 0, and whether the β parameter is shared among datasets or allowed to float. In this work, we have chosen to set the time zero to the initial peak of the signal for all data sets. The β parameter is of great importance, and must be explained further.

The parameter β reflects the underlying distribution of time constants. In the ideal case, β = 1 and the expression becomes a single exponential (the distribution becomes a delta function). In the other extreme, as $\beta \to 0$, the distribution of time constants widens, reflecting a more dispersive process. The details of the Williams-Watts distribution function, $\rho(\tau,\beta)$, are beyond this work. Lindsey and Patterson give an excellent explanation.[111] However, to illustrate the dependence of the distribution on β, ρ is frequently expressed in the form of Equation 1.15.

$$G(\tau,\beta) = \tau\rho(\tau,\beta) \qquad 1.15$$

This distribution function is plotted in Figure 1.7 with values of β ranging from 0.1 to 0.9.[111]

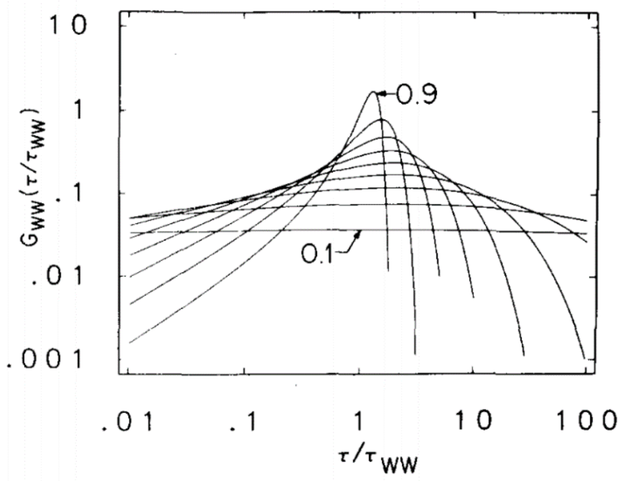

Figure 1.7 Reproduced with permission from Lindsey and Patterson.[111] The distribution function of lifetimes, G_{WW} or $G(\tau,\beta)$, as a function of the ratio τ/τ_{WW}, which is the same as τ/τ_0 in this work. Each curve is G at fixed values of β ranging from 0.1 to 0.9. At $\beta = 1$, G is a delta function centered at 1.

As the value of β decreases, the width of the distribution increases. When $\beta < 0.2$, the distribution is so wide that the first-order rate constants span over more than four orders of magnitude. The average lifetime (Equation 1.14) is the first moment of the distribution function, and this average loses meaning as the distribution widens. When comparing fits of data, it is generally preferable to fit all data with the same β parameter. With a shared β value, the fits of the kinetic data have the same distribution function describing the rate constants, so the "average" lifetime has the same meaning for all of them, regardless of its width. This allows comparison even when confidence in the absolute values is lacking due to a very wide distribution.

Another reason that the β parameter must be discussed is that the calculation of the average lifetime (Equation 1.14) relies heavily on the Γ function of the inverse of β (Equation 1.16).

$$g(\beta) = \Gamma\left(\frac{1}{\beta}\right) \tag{1.16}$$

The Γ function is defined in Equation 1.17, where x includes all real and imaginary numbers.

$$\Gamma(x) = (x - 1)! \tag{1.17}$$

Figure 1.8 depicts the real portion of Equation 1.16, with the top horizontal axis showing the value of β^{-1}.

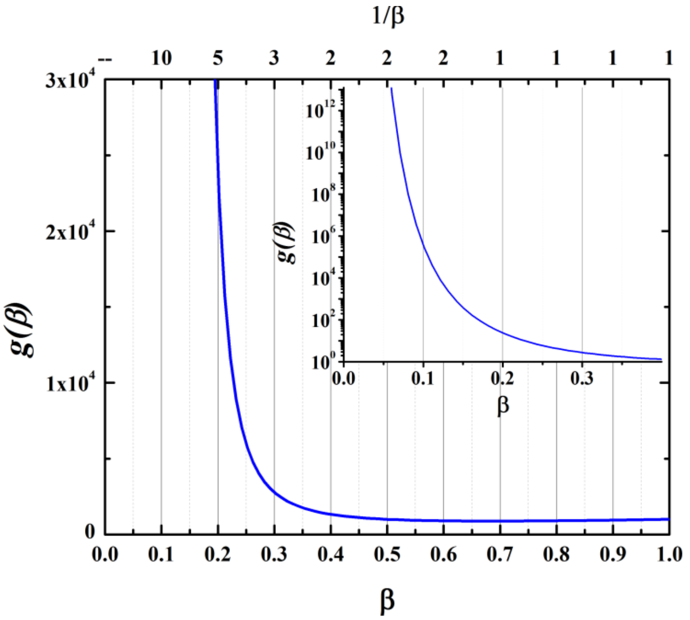

Figure 1.8 Equation 1.16, *g(β)*, is depicted for the relevant values of β (bottom horizontal axis) with corresponding values of β^{-1} shown on the top horizontal axis. The inset shows *g(β)* on a log scale with a smaller range of β to illustrate the magnitude of the increase in *g(β)* for $\beta < 0.2$.

Clearly, as β decreases, the value of *g(β)* increases with increasing acceleration as β approaches 0. Increasing error in the calculation of the average lifetime for smaller β values is implicit in this behavior. To make this explicit, the average lifetime (Equation 0) is plotted as a function of β with a typical KWW time constant $\tau_0 = 1 \times 10^{-7}$ s in Figure 1.9. The red line is the exact value, and the blue lines show the deviation in average lifetime associated with an uncertainty in β = ±0.01. Importantly, the ordinate axis is on a log scale, and the abscissa is on a reciprocal scale. This was done for clarity.

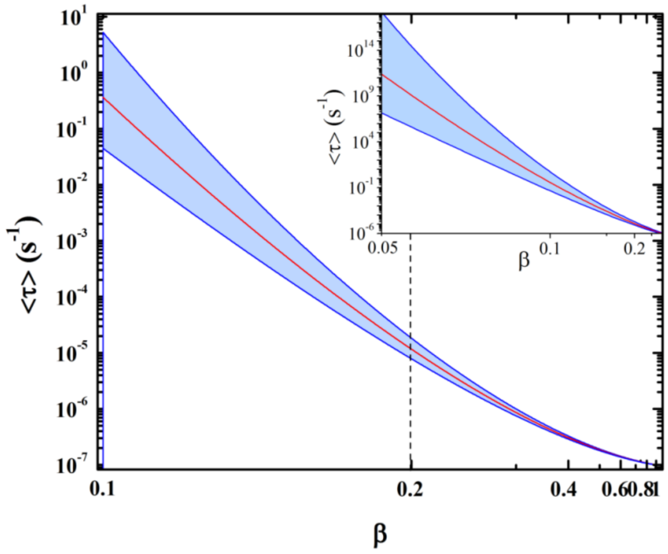

Figure 1.9 The average lifetime (Equation 1.14) on a log scale as a function of β, with a given time constant of $\tau_0 = 1 \times 10^{-7}$ s, typical for this work. The parameter β is plotted on a reciprocal scale for clarity. The dashed line at β = 0.2 indicates the lowest value of β deemed acceptable in this work. The red line is the average lifetime as a function of beta with no error. The blue lines are plots of the average lifetime with an error of ±0.01 in β, with the light blue area indicating the range of values for a given β. The inset is the same data on a different scale, showing smaller values of β.

The inset of Figure 1.9 shows the same plot on a smaller β-scale. The inset illustrates that while the possible lifetime spans less than an order of magnitude at $\beta = 0.2$, it spans three orders of magnitude at $\beta = 0.1$ and eleven orders of magnitude at $\beta = 0.05$. In this work, values of $\beta \lesssim 0.2$, indicated by the dashed line in Figure 1.9, have been avoided.

To the knowledge of the author, the first reported use of KWW to model recombination in DSSCs was in 1996.[112] Nelson, Haque, and Durrant put forth a theoretical justification for using the KWW function, which is based on the shape of the density of acceptor states in TiO_2.[22,92] The KWW function has since become ubiquitous in the field.

1.6 References

(1) IPCC, 2013: Climate Change 2013: The Physical Science Basis. Contribution of Working Group I to the Fifth Assessment Report of the Intergovernmental Panel on Climate Change; Stocker, T. F., Qin, D., Plattner, G.-K., Tignor, M., Allen, S. K., Boschung, J., Nauels, A., Xia, Y., Bex, V., Midgley, P. M., Series Eds.; Cambridge University Press, Cambridge, United Kingdom and New York, NY, USA.

(2) IPCC, 2014: Climate Change 2014: Impacts, Adaptation, and Vulnerability; Field, C. B., Barros, V. R., Dokken, D. J., Mach, K. J., Mastrandea, M. D., Bilir, T. E., Chatterjee, M., Ebi, K. L., Estrada, Y. O., Genova, R. C., Girma, B., Kissel, E. S., Levy, A. N., MacCracked, S., Mastrandrea, P. R., White, L. L., Series Eds.; Working Group II; Assessment 5; International Panel on Climate Change: Cambridge University Press in Cambridge, UK and New York, NY, 2014.

(3) Lewis, N. S.; Nocera, D. G. Powering the Planet: Chemical Challenges in Solar Energy Utilization. Proc. Natl. Acad. Sci. **2006**, 103 (43), 15729–15735.

(4) Komor, P. Renewable Energy Policy; iUniverse, 2004.

(5) Pernick, R.; Wilder, C.; Belcher, J. Clean Energy Trends 2014; Clean Edge, 2014.

(6) Son, C.-S.; Moon, H.-J.; Ahn, N. Overview of the PV Industry and R&D Strategies in Korea at the 2nd Growth Stage. Isr. J. Chem. **2015**, n/a – n/a.

(7) New World Record for Solar Cell Efficiency at 46%. French-German Cooperation Confirms Competitive Advantage of European Photovoltaic Industry. Fraunhofer ISE. December 1, 2014,.

(8) O'Regan, B. C. Early History https://workspace.imperial.ac.uk/people/Public/chemistry/Brian%20ORegan/EarlyHistory.html (accessed May 5, 2015).

(9) O'Regan, B.; Moser, J.; Anderson, M.; Graetzel, M. Vectorial Electron Injection into Transparent Semiconductor Membranes and Electric Field Effects on the Dynamics of Light-Induced Charge Separation. J. Phys. Chem. **1990**, 94 (24), 8720–8726.

(10) O'Regan, B.; Grätzel, M. A Low-Cost, High-Efficiency Solar Cell Based on Dye-Sensitized Colloidal TiO_2 Films. Nature **1991**, 353 (6346), 737–740.

(11) O'Donnell, R. M.; Johansson, P. G.; Abrahamsson, M.; Meyer, G. J. Excited-State Relaxation of Ruthenium Polypyridyl Compounds Relevant to Dye-Sensitized Solar Cells. Inorg. Chem. **2013**, 52 (12), 6839–6848.

(12) Morris, A. J.; Meyer, G. J. TiO_2 Surface Functionalization to Control the Density of States. J. Phys. Chem. C **2008**, 112 (46), 18224–18231.

(13) Brigham, E. C.; Meyer, G. J. Ostwald Isolation to Determine the Reaction Order for $TiO_2(e^-)|S^+ \rightarrow TiO_2|S$ Charge Recombination at Sensitized TiO_2 Interfaces. J. Phys. Chem. C **2014**, 118 (15), 7886–7893.

(14) Peter, L. M.; Walker, A. B.; Boschloo, G.; Hagfeldt, A. Interpretation of Apparent Activation Energies for Electron Transport in Dye-Sensitized Nanocrystalline Solar Cells. J. Phys. Chem. B **2006**, 110 (28), 13694–13699.

(15) Main, C.; Marshall, J. M.; Reynolds, S. Computer Modelling of Multi-Trapping and Hopping Transport in Disordered Semiconductors. J. Optoelectron. Adv. Mater. 7 (1), 107–114.

(16) Scher, H.; Montroll, E. W. Anomalous Transit-Time Dispersion in Amorphous Solids. Phys. Rev. B **1975**, 12 (6), 2455–2477.

(17) Bisquert, J. Hopping Transport of Electrons in Dye-Sensitized Solar Cells. J. Phys. Chem. C **2007**, 111 (46), 17163–17168.

(18) Bisquert, J.; Zaban, A.; Salvador, P. Analysis of the Mechanisms of Electron Recombination in Nanoporous TiO_2 Dye-Sensitized Solar Cells. Nonequilibrium Steady-State Statistics and Interfacial Electron Transfer via Surface States. J. Phys. Chem. B **2002**, 106 (34), 8774–8782.

(19) Fabregat-Santiago, F.; Garcia-Belmonte, G.; Bisquert, J.; Zaban, A.; Salvador, P. Decoupling of Transport, Charge Storage, and Interfacial Charge Transfer in the Nanocrystalline TiO_2/Electrolyte System by Impedance Methods. J. Phys. Chem. B **2002**, 106 (2), 334–339.

(20) Katoh, R.; Furube, A.; Barzykin, A. V.; Arakawa, H.; Tachiya, M. Kinetics and Mechanism of Electron Injection and Charge Recombination in Dye-Sensitized Nanocrystalline Semiconductors. Coord. Chem. Rev. **2004**, 248 (13–14), 1195–1213.

(21) Barzykin, A. V.; Tachiya, M. Mechanism of Charge Recombination in Dye-Sensitized Nanocrystalline Semiconductors: Random Flight Model. J. Phys. Chem. B **2002**, 106 (17), 4356–4363.

(22) Nelson, J. Continuous-Time Random-Walk Model of Electron Transport in Nanocrystalline TiO_{2} Electrodes. Phys. Rev. B **1999**, 59 (23), 15374–15380.

(23) Demas, J. N.; DeGraff, B. A. Design and Applications of Highly Luminescent Transition Metal Complexes. Anal. Chem. **1991**, 63 (17), 829A – 837A.

(24) Miessler, G. S.; Tarr, D. A. Coordination Chemistry III: Electronic Spectra. In Inorganic Chemistry; Pearson Education, Inc., 2004; pp 379–411.

(25) Figgis, B. N. Ligand Field Theory. In Comprehensive Coordination Chemistry: Indexes; Wilkinson, G., Gillard, R. D., McCleverty, J. A., Eds.; Pergamon Press, 1987; pp 243–246.

(26) Figgis, B. N.; Hitchman, M. A. Ligand Field Theory and Its Applications; Wiley-VCH: New York, N. Y., 2000.

(27) Adamson, A. W.; Fleischauer, P. D. s. Concepts of Inorganic Photochemistry; John Wiley & Sons Australia, Limited, 1975.

(28) Grätzel, M. Solar Energy Conversion by Dye-Sensitized Photovoltaic Cells. Inorg. Chem. **2005**, 44 (20), 6841–6851.

(29) Meyer, G. J. Molecular Approaches to Solar Energy Conversion with Coordination Compounds Anchored to Semiconductor Surfaces. Inorg. Chem. **2005**, 44 (20), 6852–6864.

(30) Ardo, S.; Meyer, G. J. Photodriven Heterogeneous Charge Transfer with Transition-Metal Compounds Anchored to TiO_2 Semiconductor Surfaces. Chem. Soc. Rev. **2009**, 38 (1), 115–164.

(31) Gust, D.; Moore, T. A.; Moore, A. L. Solar Fuels via Artificial Photosynthesis. Acc. Chem. Res. **2009**, 42 (12), 1890–1898.

(32) Youngblood, W. J.; Lee, S.-H. A.; Kobayashi, Y.; Hernandez-Pagan, E. A.; Hoertz, P. G.; Moore, T. A.; Moore, A. L.; Gust, D.; Mallouk, T. E. Photoassisted Overall Water Splitting in a Visible Light-Absorbing Dye-Sensitized Photoelectrochemical Cell. J. Am. Chem. Soc. **2009**, 131 (3), 926–927.

(33) Youngblood, W. J.; Lee, S.-H. A.; Maeda, K.; Mallouk, T. E. Visible Light Water Splitting Using Dye-Sensitized Oxide Semiconductors. Acc. Chem. Res. **2009**, 42 (12), 1966–1973.

(34) Caspar, J. V.; Meyer, T. J. Photochemistry of Ru(bpy)32+. Solvent Effects. J. Am. Chem. Soc. **1983**, 105 (17), 5583–5590.

(35) Kalyanasundaram, K. Photophysics, Photochemistry and Solar Energy Conversion with tris(bipyridyl)ruthenium(II) and Its Analogues. Coord. Chem. Rev. **1982**, 46, 159–244.

(36) Moucheron, C.; Kirsch-De Mesmaeker, A.; Kelly, J. M. Photoreactions of Ruthenium (II) and Osmium (II) Complexes with Deoxyribonucleic Acid (DNA). J. Photochem. Photobiol. B **1997**, 40 (2), 91–106.

(37) McCusker, J. K. Femtosecond Absorption Spectroscopy of Transition Metal Charge-Transfer Complexes. Acc. Chem. Res. **2003**, 36 (12), 876–887.

(38) Gorman, B. A.; Francis, P. S.; Barnett, N. W. Tris(2,2’-bipyridyl)ruthenium(II) Chemiluminescence. The Analyst **2006**, 131 (5), 616.

(39) Balzani, V.; Juris, A. Photochemistry and Photophysics of Ru(II)□polypyridine Complexes in the Bologna Group. From Early Studies to Recent Developments. Coord. Chem. Rev. **2001**, 211 (1), 97–115.

(40) Gerardi, R. D.; Barnett, N. W.; Lewis, S. W. Analytical Applications of tris(2,2′-bipyridyl)ruthenium(III) as a Chemiluminescent Reagent. Anal. Chim. Acta **1999**, 378 (1–3), 1–41.

(41) AllenJ Bard. Electrogenerated Chemiluminescence; CRC Press, 2004.

(42) Damrauer, N. H.; Cerullo, G. Femtosecond Dynamics of Excited-State Evolution in ...Ru(bpy)... Science **1997**, 275 (5296), 54–57.

(43) Hasselmann, G. M.; Meyer, G. J. Sensitization of Nanocrystalline TiO_2 by Re(I) Polypyridyl Compounds*. Z. Für Phys. Chem. **2011**, 212 (Part_1), 39–44.

(44) Ardo, S.; Meyer, G. J. Recent Advances in Photo-Initiated Electron-Transfer at the Interface between Anatase TiO_2 Nanocrystallites and Transition-Metal Polypyridyl Compounds. In Energy Production and Storage : Inorganic Chemical Strategies for a Warming World; Crabtree, R. H., Ed.; Wiley: Hoboken, 2013.

(45) Ning, Z.; Zhang, Q.; Wu, W.; Tian, H. Novel Iridium Complex with Carboxyl Pyridyl Ligand for Dye-Sensitized Solar Cells: High Fluorescence Intensity, High Electron Injection Efficiency? J. Organomet. Chem. **2009**, 694 (17), 2705–2711.

(46) Dragonetti, C.; Valore, A.; Colombo, A.; Righetto, S.; Trifiletti, V. Simple Novel Cyclometallated Iridium Complexes for Potential Application in Dye-Sensitized Solar Cells. Inorganica Chim. Acta **2012**, 388, 163–167.

(47) Wang, D.; Wu, Y.; Dong, H.; Qin, Z.; Zhao, D.; Yu, Y.; Zhou, G.; Jiao, B.; Wu, Z.; Gao, M.; Wang, G. Iridium (III) Complexes with 5,5-Dimethyl-3-(pyridin-2-Yl)cyclohex-2-Enone Ligands as

Sensitizer for Dye-Sensitized Solar Cells. Org. Electron. **2013**, 14 (12), 3297–3305.

(48) Argazzi, R.; Larramona, G.; Contado, C.; Bignozzi, C. A. Preparation and Photoelectrochemical Characterization of a Red Sensitive Osmium Complex Containing 4,4′,4″-Tricarboxy-2,2′:6′,2″-Terpyridine and Cyanide Ligands. J. Photochem. Photobiol. Chem. **2004**, 164 (1–3), 15–21.

(49) Kinoshita, T.; Fujisawa, J.; Nakazaki, J.; Uchida, S.; Kubo, T.; Segawa, H. Enhancement of Near-IR Photoelectric Conversion in Dye-Sensitized Solar Cells Using an Osmium Sensitizer with Strong Spin-Forbidden Transition. J. Phys. Chem. Lett. **2012**, 3 (3), 394–398.

(50) Altobello, S.; Argazzi, R.; Caramori, S.; Contado, C.; Da Fré, S.; Rubino, P.; Choné, C.; Larramona, G.; Bignozzi, C. A. Sensitization of Nanocrystalline TiO_2 with Black Absorbers Based on Os and Ru Polypyridine Complexes. J. Am. Chem. Soc. **2005**, 127 (44), 15342–15343.

(51) Polo, A. S.; Itokazu, M. K.; Murakami Iha, N. Y. Metal Complex Sensitizers in Dye-Sensitized Solar Cells. Coord. Chem. Rev. **2004**, 248 (13–14), 1343–1361.

(52) Lakowicz, J. R. Principles of Fluorescence Spectroscopy; Springer, 2007.

(53) Bozic-Weber, B.; Constable, E. C.; Housecroft, C. E. Light Harvesting with Earth Abundant D-Block Metals: Development of Sensitizers in Dye-Sensitized Solar Cells (DSCs). Coord. Chem. Rev. **2013**, 257 (21–22), 3089–3106.

(54) Ferrere, S.; Gregg, B. A. Photosensitization of TiO_2 by [FeII(2,2‘-Bipyridine-4,4‘-Dicarboxylic acid)2(CN)2]: Band Selective Electron Injection from Ultra-Short-Lived Excited States. J. Am. Chem. Soc. **1998**, 120 (4), 843–844.

(55) Ferrere, S. New Photosensitizers Based upon [Fe(L)2(CN)2] and [Fe(L)3] (L = Substituted 2,2‘-Bipyridine): Yields for the Photosensitization of TiO_2 and Effects on the Band Selectivity. Chem. Mater. **2000**, 12 (4), 1083–1089.

(56) Ferrere, S. New Photosensitizers Based upon [FeII(L)2(CN)2] and [FeIIL3], Where L Is Substituted 2,2′-Bipyridine. Inorganica Chim. Acta **2002**, 329 (1), 79–92.

(57) Balraju, P.; Kumar, M.; Roy, M. S.; Sharma, G. D. Dye Sensitized Solar Cells (DSSCs) Based on Modified Iron Phthalocyanine Nanostructured TiO_2 Electrode and PEDOT:PSS Counter Electrode. Synth. Met. **2009**, 159 (13), 1325–1331.

(58) Zanotti, G.; Angelini, N.; Notarantonio, S.; Paoletti, A. M.; Pennesi, G.; Rossi, G.; Lembo, A.; Colonna, D.; Di Carlo, A.; Reale, A.; Brown, T. M.; Calogero, G. Bridged Phthalocyanine Systems for Sensitization of Nanocrystalline TiO_2 Films. Int. J. Photoenergy **2010**, 2010, e136807.

(59) Bowman, D. N.; Blew, J. H.; Tsuchiya, T.; Jakubikova, E. Elucidating Band-Selective Sensitization in Iron(II) Polypyridine-TiO_2 Assemblies. Inorg. Chem. **2013**, 52 (15), 8621–8628.

(60) Ballhausen, C. J. Introduction to Ligand Field Theory; McGraw-Hill: Ney York, 1962.

(61) Lever, A. B. P. Inorganic Electronic Spectroscopy, 2nd ed.; Elsevier: New York, 1984.

(62) Monat, J. E.; McCusker, J. K. Femtosecond Excited-State Dynamics of an Iron(II) Polypyridyl Solar Cell Sensitizer Model. J. Am. Chem. Soc. **2000**, 122 (17), 4092–4097.

(63) Creutz, C.; Chou, M.; Netzel, T. L.; Okumura, M.; Sutin, N. Lifetimes, Spectra, and Quenching of the Excited States of Polypyridine Complexes of iron(II), ruthenium(II), and osmium(II). J. Am. Chem. Soc. **1980**, 102 (4), 1309–1319.

(64) Lazorski, M. S.; Castellano, F. N. Advances in the Light Conversion Properties of Cu(I)-Based Photosensitizers. Polyhedron.

(65) Yella, A.; Lee, H.-W.; Tsao, H. N.; Yi, C.; Chandiran, A. K.; Nazeeruddin, M. K.; Diau, E. W.-G.; Yeh, C.-Y.; Zakeeruddin, S. M.; Grätzel, M. Porphyrin-Sensitized Solar Cells with Cobalt (II/III)–Based Redox Electrolyte Exceed 12 Percent Efficiency. Science **2011**, 334 (6056), 629–634.

(66) Yella, A.; Mai, C.-L.; Zakeeruddin, S. M.; Chang, S.-N.; Hsieh, C.-H.; Yeh, C.-Y.; Grätzel, M. Molecular Engineering of Push-Pull Porphyrin Dyes for Highly Efficient Dye-Sensitized Solar Cells: The Role of Benzene Spacers. Angew. Chem. Int. Ed. **2014**, 53 (11), 2973–2977.

(67) Mathew, S.; Yella, A.; Gao, P.; Humphry-Baker, R.; Curchod, B. F. E.; Ashari-Astani, N.; Tavernelli, I.; Rothlisberger, U.; Nazeeruddin, M. K.; Grätzel, M. Dye-Sensitized Solar Cells with 13% Efficiency Achieved through the Molecular Engineering of Porphyrin Sensitizers. Nat. Chem. **2014**, 6 (3), 242–247.

(68) Achey, D.; Ardo, S.; Xia, H.-L.; Siegler, M. A.; Meyer, G. J. Sensitization of TiO_2 by the MLCT Excited State of CoI Coordination Compounds. J. Phys. Chem. Lett. **2011**, 2 (4), 305–308.

(69) Achey, D.; Brigham, E. C.; Dimarco, B. N.; Meyer, G. J. Excited State Electron Transfer after Visible Light Absorption by the Co(I) State of Vitamin B12. Chem. Commun. **2014**, In press.

(70) Achey, D. C. Cobalt and Nickel Macrocycles Anchored to Nanocrystalline Titanium Dioxide Thin Films: Sensitization, Catalysis, and Ligand Association. Ph.D., The Johns Hopkins University: United States -- Maryland, 2013.

(71) Lexa, D.; Saveant, J. M. The Electrochemistry of Vitamin B12. Acc. Chem. Res. **1983**, 16 (7), 235–243.

(72) Kadish, K. M.; Bottomley, L. A.; Beroiz, D. Reactions of Pyridine with a Series of Para-Substituted Tetraphenylporphyrincobalt and -Iron Complexes. Inorg. Chem. **1978**, 17 (5), 1124–1129.

(73) Achey, D.; Ardo, S.; Meyer, G. J. Increase in the Coordination Number of a Cobalt Porphyrin after Photo-Induced Interfacial Electron Transfer into Nanocrystalline TiO_2. Inorg. Chem. **2012**, 51 (18), 9865–9872.

(74) Hagfeldt, A.; Boschloo, G.; Sun, L.; Kloo, L.; Pettersson, H. Dye-Sensitized Solar Cells. Chem. Rev. **2010**, 110 (11), 6595–6663.

(75) Campbell, W. M.; Burrell, A. K.; Officer, D. L.; Jolley, K. W. Porphyrins as Light Harvesters in the Dye-Sensitised TiO_2 Solar Cell. Coord. Chem. Rev. **2004**, 248 (13–14), 1363–1379.

(76) Eric Wei-Guang Diau; Lu-Lin Li. Porphyrin-Sensitized Solar Cells. In Handbook of Porphyrin Science (Volume 28); Handbook of Porphyrin Science; World Scientific Publishing Company, 2013; Vol. Volume 28, pp 279–317.

(77) Kuciauskas, D.; Freund, M. S.; Gray, H. B.; Winkler, J. R.; Lewis, N. S. Electron Transfer Dynamics in Nanocrystalline Titanium Dioxide Solar Cells Sensitized with Ruthenium or Osmium Polypyridyl Complexes. J. Phys. Chem. B **2001**, 105 (2), 392–403.

(78) Alibabaei, L.; Luo, H.; House, R. L.; Hoertz, P. G.; Lopez, R.; Meyer, T. J. Applications of Metal Oxide Materials in Dye Sensitized Photoelectrosynthesis Cells for Making Solar Fuels: Let the Molecules Do the Work. J. Mater. Chem. A **2013**, 1 (13), 4133–4145.

(79) Hu, K.; Robson, K. C. D.; Beauvilliers, E. E.; Schott, E.; Zarate, X.; Arratia-Perez, R.; Berlinguette, C. P.; Meyer, G. J. Intramolecular and Lateral Intermolecular Hole Transfer at the Sensitized TiO_2 Interface. J. Am. Chem. Soc. **2014**, 136 (3), 1034–1046.

(80) Ardo, S.; Meyer, G. J. Characterization of Photoinduced Self-Exchange Reactions at Molecule–Semiconductor Interfaces by Transient Polarization Spectroscopy: Lateral Intermolecular Energy and Hole Transfer across Sensitized TiO_2 Thin Films. J. Am. Chem. Soc. **2011**, 133 (39), 15384–15396.

(81) Moser, J. E.; Grätzel, M. Observation of Temperature Independent Heterogeneous Electron Transfer Reactions in the Inverted Marcus Region. Chem. Phys. **1993**, 176 (2–3), 493–500.

(82) Bisquert, J.; Mora-Seró, I. Simulation of Steady-State Characteristics of Dye-Sensitized Solar Cells and the Interpretation of the Diffusion Length. J. Phys. Chem. Lett. **2010**, 1 (1), 450–456.

(83) Nelson, J. Continuous-Time Random-Walk Model of Electron Transport in Nanocrystalline TiO_{2} Electrodes. Phys. Rev. B **1999**, 59 (23), 15374–15380.

(84) Hasselmann, G. M.; Meyer, G. J. Diffusion-Limited Interfacial Electron Transfer with Large Apparent Driving Forces. J. Phys. Chem. B **1999**, 103 (36), 7671–7675.

(85) Katoh, R.; Furube, A.; Barzykin, A. V.; Arakawa, H.; Tachiya, M. Kinetics and Mechanism of Electron Injection and Charge

Recombination in Dye-Sensitized Nanocrystalline Semiconductors. Coord. Chem. Rev. **2004**, 248 (13–14), 1195–1213.

(86) Peter, L. M.; Walker, A. B.; Boschloo, G.; Hagfeldt, A. Interpretation of Apparent Activation Energies for Electron Transport in Dye-Sensitized Nanocrystalline Solar Cells. J. Phys. Chem. B **2006**, 110 (28), 13694–13699.

(87) Kuciauskas, D.; Freund, M. S.; Gray, H. B.; Winkler, J. R.; Lewis, N. S. Electron Transfer Dynamics in Nanocrystalline Titanium Dioxide Solar Cells Sensitized with Ruthenium or Osmium Polypyridyl Complexes. J. Phys. Chem. B **2001**, 105 (2), 392–403.

(88) Clifford, J. N.; Palomares, E.; Nazeeruddin, M. K.; Grätzel, M.; Nelson, J.; Li, X.; Long, N. J.; Durrant, J. R. Molecular Control of Recombination Dynamics in Dye-Sensitized Nanocrystalline TiO_2 Films: Free Energy vs Distance Dependence. J. Am. Chem. Soc. **2004**, 126 (16), 5225–5233.

(89) Clifford, J. N.; Yahioglu, G.; Milgrom, L. R.; Durrant, J. R. Molecular Control of Recombination Dynamics in Dye Sensitised Nanocrystalline TiO_2 Films. Chem. Commun. **2002**, No. 12, 1260–1261.

(90) Haque, S. A.; Tachibana, Y.; Klug, D. R.; Durrant, J. R. Charge Recombination Kinetics in Dye-Sensitized Nanocrystalline Titanium Dioxide Films under Externally Applied Bias. J. Phys. Chem. B **1998**, 102 (10), 1745–1749.

(91) Haque, S. A.; Tachibana, Y.; Willis, R. L.; Moser, J. E.; Grätzel, M.; Klug, D. R.; Durrant, J. R. Parameters Influencing Charge Recombination Kinetics in Dye-Sensitized Nanocrystalline Titanium Dioxide Films. J. Phys. Chem. B **2000**, 104 (3), 538–547.

(92) Nelson, J.; Haque, S. A.; Klug, D. R.; Durrant, J. R. Trap-Limited Recombination in Dye-Sensitized Nanocrystalline Metal Oxide Electrodes. Phys. Rev. B **2001**, 63 (20), 205321.

(93) Hasselmann, G. M.; Meyer, G. J. Diffusion-Limited Interfacial Electron Transfer with Large Apparent Driving Forces. J. Phys. Chem. B **1999**, 103 (36), 7671–7675.

(94) Haque, S. A.; Handa, S.; Peter, K.; Palomares, E.; Thelakkat, M.; Durrant, J. R. Supermolecular Control of Charge Transfer in Dye-Sensitized Nanocrystalline TiO_2 Films: Towards a Quantitative Structure–Function Relationship. Angew. Chem. Int. Ed. **2005**, 44 (35), 5740–5744.

(95) Johansson, P. G.; Kopecky, A.; Galoppini, E.; Meyer, G. J. Distance Dependent Electron Transfer at TiO_2 Interfaces Sensitized with Phenylene Ethynylene Bridged RuII–Isothiocyanate Compounds. J. Am. Chem. Soc. **2013**, 135 (22), 8331–8341.

(96) Tachibana, Y.; Haque, S. A.; Mercer, I. P.; Moser, J. E.; Klug, D. R.; Durrant, J. R. Modulation of the Rate of Electron Injection in Dye-Sensitized Nanocrystalline TiO_2 Films by Externally Applied Bias. J. Phys. Chem. B **2001**, 105 (31), 7424–7431.

(97) Kamat, P. V.; Bedja, I.; Hotchandani, S.; Patterson, L. K. Photosensitization of Nanocrystalline Semiconductor Films. Modulation of Electron Transfer between Excited Ruthenium Complex and SnO_2 Nanocrystallites with an Externally Applied Bias. J. Phys. Chem. **1996**, 100 (12), 4900–4908.

(98) Lu, H.; Prieskorn, J. N.; Hupp, J. T. Fast Interfacial Electron Transfer: Evidence for Inverted Region Kinetic Behavior. J. Am. Chem. Soc. **1993**, 115 (11), 4927–4928.

(99) Yan, S. G.; Prieskorn, J. S.; Kim, Y.; Hupp, J. T. In Search of the Inverted Region: Chromophore-Based Driving Force Dependence of Interfacial Electron Transfer Reactivity at the Nanocrystalline Titanium Dioxide Semiconductor/Solution Interface†. J. Phys. Chem. B **2000**, 104 (46), 10871–10877.

(100) Kelly, C. A.; Farzad, F.; Thompson, D. W.; Stipkala, J. M.; Meyer, G. J. Cation-Controlled Interfacial Charge Injection in Sensitized Nanocrystalline TiO_2. Langmuir **1999**, 15 (20), 7047–7054.

(101) Brigham, E. C.; Achey, D.; Meyer, G. J. Excited State Electron Transfer from Cobalt Coordination Compounds Anchored to TiO_2. Polyhedron **2014**, under review.

(102) Abrahamsson, M.; Johansson, P. G.; Ardo, S.; Kopecky, A.; Galoppini, E.; Meyer, G. J. Decreased Interfacial Charge Recombination Rate Constants with N3-Type Sensitizers. J. Phys. Chem. Lett. **2010**, 1 (11), 1725–1728.

(103) Johansson, P. G.; Zhang, Y.; Abrahamsson, M.; Meyer, G. J.; Galoppini, E. Slow Excited State Injection and Charge Recombination at Star-Shaped Ruthenium Polypyridyl compounds—TiO_2 Interfaces. Chem. Commun. **2011**, 47 (22), 6410.

(104) Johansson, P. G.; Zhang, Y.; Meyer, G. J.; Galoppini, E. Homoleptic "Star" Ru(II) Polypyridyl Complexes: Shielded Chromophores to Study Charge-Transfer at the Sensitizer-TiO_2 Interface. Inorg. Chem. **2013**, 52 (14), 7947–7957.

(105) Bonhôte, P.; Moser, J.-E.; Humphry-Baker, R.; Vlachopoulos, N.; Zakeeruddin, S. M.; Walder, L.; Grätzel, M. Long-Lived Photoinduced Charge Separation and Redox-Type Photochromism on Mesoporous Oxide Films Sensitized by Molecular Dyads. J. Am. Chem. Soc. **1999**, 121 (6), 1324–1336.

(106) Knauf, R. R.; Brennaman, M. K.; Alibabaei, L.; Norris, M. R.; Dempsey, J. L. Revealing the Relationship between Semiconductor Electronic Structure and Electron Transfer Dynamics at Metal Oxide–Chromophore Interfaces. J. Phys. Chem. C **2013**, 117 (48), 25259–25268.

(107) Espenson, J. H. Chemical Kinetics and Reaction Mechanisms; McGraw-Hill: New York, 2002.

(108) Kohlrausch, R. Theorie Des Elektrischen Rückstandes in Der Leidener Flasche. Ann. Phys. Chem. Leipz. **1854**, 91, 56–82.

(109) Kohlrausch, R. Theorie Des Elektrischen Rückstandes in Der Leidener Flasche. Ann. Phys. **1854**, 167 (2), 179–214.
(110) Williams, G.; Watts, D. C. Non-Symmetrical Dielectric Relaxation Behaviour Arising from a Simple Empirical Decay Function. Trans. Faraday Soc. **1970**, 66 (0), 80–85.
(111) Lindsey, C. P.; Patterson, G. D. Detailed Comparison of the Williams–Watts and Cole–Davidson Functions. J. Chem. Phys. **1980**, 73 (7), 3348.
(112) Heimer, T. A.; D'Arcangelis, S. T.; Farzad, F.; Stipkala, J. M.; Meyer, G. J. An Acetylacetonate-Based Semiconductor−Sensitizer Linkage. Inorg. Chem. **1996**, 35 (18), 5319–5324.

Chapter 2. Ostwald Isolation to Determine the Reaction Order for $TiO_2(e^-)|S^+ \rightarrow TiO_2|S$ Charge Recombination at Sensitized TiO_2 Interfaces

2.1 Introduction

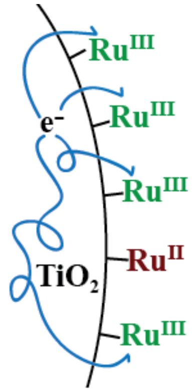

Figure 2.1

Recombination of electrons injected into mesoporous nanocrystalline TiO_2 thin films with oxidized sensitizer molecules has been of theoretical,[1–3] experimental,[4–9] and practical[10] interest for some time. The reaction is of practical importance as it can lower the efficiency of dye sensitized solar cells, particularly near the power point and open circuit conditions.[11,12] The reaction is also of intellectual interest as the injected electrons and oxidized sensitizers do not undergo significant geminate recombination. Instead, the charges diffuse through the three dimensional volume of the mesoporous TiO_2 network or the quasi-two-dimensional molecular layer of the sensitizer before interfacial charge recombination occurs. A proper mechanistic analysis of kinetic data could in principle directly provide rate constants for the fundamental interfacial electron transfer event *and* diffusion of the injected electron and the oxidized sensitizer. The most basic reaction that can be written for charge recombination is given in Equation 2.1.

$$TiO_2(e^-)|S^+ \rightarrow TiO_2|S \qquad 2.1$$

The rate law for the reaction is expressed in Equation 2.2, where n and m are the order of the reaction in electrons and oxidized sensitizers, respectively.

$$rate = k[TiO_2(e^-)]^n[S^+]^m \qquad 2.2$$

Until now, to our knowledge, the kinetic order of each reactant has not been experimentally determined, probably because most, but not all,[6,7,13–16] prior studies employed conditions where the number of oxidized sensitizers and injected electrons were equal. The order of the oxidized sensitizer has quite reasonably been assumed to be 1, but there is a dearth of experimental support for this assumption. Chemical intuition would suggest that the order of the electron should also be 1, but in practice the experimental data rarely report directly on the reaction order, yet values between 2 and 3 have been reported.[17]

In fluid solution, reaction orders are typically determined by quantifying rates when one or more of the reactants are present in large excess such that kinetic isolation conditions apply.[18] This phenomenally successful experimental technique was originally termed ‘Ostwald isolation’, but is more often referred to simply as the ‘isolation method’ or ‘flooding’.[18,19] Regardless of the name, the approach is not so much a mathematical approximation as it is an experimental condition that must be identified so that the reaction order (and rate constants) can be determined. In fluid solution these conditions are well established, and the rule of thumb commonly prescribed is a 10 fold stoichiometric excess of all reactants but one.[18] One purpose of this study was to determine whether Ostwald isolation could be applied to sensitized-semiconductor interfaces where 'concentration' is inherently ill-defined, yet intrinsic rate constants for the elementary steps of this recombination reaction are of great importance.

2.2 Experimental

2.2.1 Materials

The following substances were used as received from the provider: titanium(IV) isopropoxide (Aldrich, 97%), acetonitrile (Burdick and Jackson, spectrophotometric grade), lithium perchlorate (Aldrich, 99.99%), polyethylene glycol bisphenol A epichlorohydrin copolymer 15,000-20,000 Da (Sigma), nitric acid (Macron Fine Chemicals, ACS Reagent grade), fluorine-doped tin oxide coated glass (Hartford Glass Company, Inc., 15 Ω/□, 2.3 mm thick).

2.2.2 Titanium dioxide thin film electrode preparation

TiO_2-anatase nanocrystallites were prepared from titanium(IV) isopropoxide as previously described[20] and stored in the dark. The sol was doctor bladed onto glass slides with a conductive layer of fluorine-doped tin oxide (FTO), using clear cellophane tape as a spacer (~10 µm thick). After drying in the dark for 30 minutes, the cellophane was removed and the films were sintered at 450 °C under a flow of O_2 at ~1 atm. The resulting mesoporous thin films were stored in an oven at ~75 °C until use.

2.2.3 Sensitization of TiO_2

The TiO_2 electrode was immersed in a 1:1 *tert*-butanol:CH_3CN solution of $[Ru(bpy)_2(dcb)][ClO_4]_2$ (where bpy = 2,2'-bipyridine and dcb = [2,2'-bipyridine]-4,4'-dicarboxylic acid) for several days to anchor the sensitizer producing $FTO|TiO_2|Ru(bpy)_2(dcb)$, abbreviated $TiO_2|S$ herein. The electrode was then rinsed with acetonitrile and immersed in acetonitrile for 0.5-2 hours before use. No absorbance change was observed during immersion.

2.2.4 Spectroscopic measurements

All electronic absorption measurements were recorded in a quartz cuvette on a Varian Cary 50 spectrophotometer at ambient temperature under an argon atmosphere. The probe beam was incident at a 45° angle on the glass side of the $FTO|TiO_2$ sample.

2.2.4.1 ***Spectroelectrochemical measurements***

Experiments were conducted with a BAS CV-50W potentiostat and 0.3 M $LiClO_4$ CH_3CN electrolyte in a standard 3-electrode cell with the

FTO|TiO_2 serving as the working electrode, a platinum disk counter electrode, and Ag/AgCl reference electrode. The reference electrode was calibrated with the ferrocenium/ferrocene couple in 0.3 M $LiClO_4$ CH_3CN before and after each experiment. The measured potentials were converted to NHE using the previously reported[21] potential of ferrocene in CH_3CN (+630 mV *vs.* NHE). Prior to spectroelectrochemical measurement, a CV was taken at a scan rate of 100 mV/s. The typical magnitude of the peak current density was 150 μA/cm^2 or more. The experiment then proceeded by monitoring the absorbance of TiO_2|$Ru(bpy)_2(dcb)$ with increasingly negative or positive applied potential. Each potential was held until the absorbance was stable, a minimum of 3 minutes in the negative direction and 5 minutes in the positive direction. In the case of negative applied potential, the potential was stepped by ~100 mV, while in the case of positive potential, the steps began at 100 mV and gradually decreased to 10 mV near the reduction potential measured in the CV, and becoming larger as the potential exceeded the measured reduction potential. After measurement in each direction, a potential of ~0 mV *vs.* NHE was applied until the absorbance spectrum returned to match the initial spectrum.

In the case of positive applied potentials, the absorbance spectra of the Ru(II) species and the Ru(III) species were used to make a global fit to the absorbance data at each potential in Wolfram Mathematica 9 using a

Least Squares analysis. This operation yielded fractional abundance of Ru(II) and Ru(III) at each potential. This data was fit to Equation 2.3 in Origin 8.

In the case of negative applied potentials, the absorbance at 800 nm was used to measure the electron concentration in the TiO_2 film using a $TiO_2(e^-)$ molar absorptivity of 1000 $M^{-1}cm^{-1}$. The absorbance of the film at 800 nm was related to the geometric surface area using Equation 2.4. The absorbance of $TiO_2(e^-)$ was converted to concentration in cm^{-3} by calculating the volume of the film using the modified Beer-Lambert law (Equation 2.4), a porosity of 50%, and a film thickness of 10 μm.

2.2.4.2 ***Nanosecond transient absorption spectroscopy***

Measurements were made under argon at ambient temperature in a previously described apparatus.[22] A 150 W xenon arc lamp (Applied Photophysics) pulsed at 1 Hz served as the probe beam, was directed through a long-pass 385 nm filter toward a Spex monochromator that was optically coupled to a R928 Hammatsu photomultiplier tube. The signal was recorded by an optically triggered LeCroy 9450 oscilloscope with 2.5 ns resolution. The excitation beam was a Q-switched Nd:YAG (Quantel USA (BigSky) Brilliant B) pulsed at 1 Hz and oriented perpendicular to the probe beam. The appropriate non-linear optics to produce 532 nm excitation were employed, and the excitation fluence was measured with a thermopile power meter (Molectron). The instrument response time was ~10 ns. The sample was positioned such that the probe and excitation beams were both incident at a 45° angle on the glass side of the sample. For measurements made with an applied potential, a 3-electrode cell (*vide supra)* was used. At each potential step the current was monitored until it stabilized (generally ~10 minutes), only after which transient absorbance measurements were recorded.

2.3 Results & Discussion

Nanocrystalline, mesoporous thin films of ~20 nm diameter anatase TiO_2 particles deposited on fluorine doped tin oxide coated glass (FTO) were sensitized to visible light by $[Ru(bpy)_2(dcb)][ClO_4]_2$, where bpy is 2,2'-bipyridine and dcb = [2,2'-bipyridine]-4,4'-dicarboxylic acid, as has been previously described.[20] This sensitized thin film has been the subject of many previous studies and is abbreviated as $TiO_2|S$ within.

Spectroelectrochemistry was employed to determine the concentrations of $TiO_2|S$ and $TiO_2|S^+$ in 300 mM $LiClO_4/CH_3CN$ at the positive applied potentials indicated in Figure 2.2. The bleach of the metal-to-ligand charge-transfer (MLCT) absorption of S with increased positive applied potential evinces the oxidation of $TiO_2|S$ to yield $TiO_2|S^+$, a reaction known to proceed by lateral hole hopping from sensitizers anchored to the FTO substrate.[23,24]

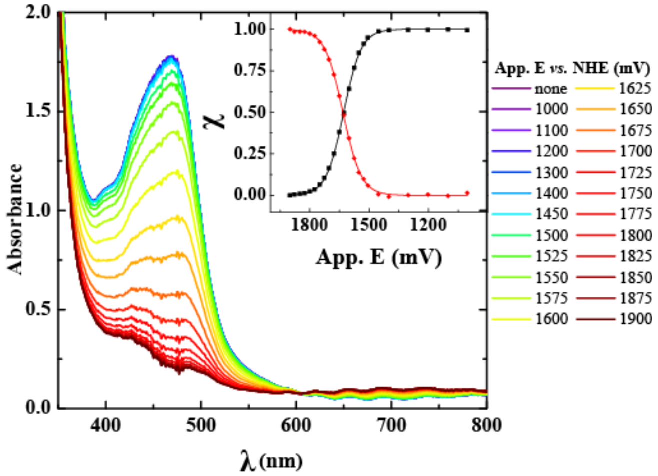

Figure 2.2 The absorbance of a $[Ru(bpy)_2(dcb)]^{2+}$ sensitized TiO_2 thin film, abbreviated $TiO_2|S$, measured at open circuit and at the indicated positive applied potentials. Inset: The fractional abundance, x, of $TiO_2|S$ (black) and $TiO_2|S^+$ (red) at each potential with an overlaid sigmoidal fit to the modified Nernst equation (Equation 2.3), from which an $E^0(TiO_2|S^{+/0})$ = 1630 mV *vs.* NHE and an ideality factor i = 1.76 were abstracted.

The inset of Figure 2.2 shows the fractional abundance, x, of $TiO_2|S$ (black) and $TiO_2|S^+$ (red), present at the indicated potentials as determined by standard addition of the known absorption spectra of $TiO_2|S$ and $TiO_2|S^+$. Overlaid on this data are fits to Equation 2.3, where E is the applied potential, E^0 is the reduction potential, and i is the ideality factor.[25]

$$\chi(E) = \frac{1}{1 + 10^{\frac{E-E^0}{i \cdot 59}}} \qquad 2.3$$

These fits yielded E^0 = 1.00 V *vs.* $Fc^{+/0}$ (approximately 1.63 V *vs.* NHE)[22] for the $TiO_2|S^{+/0}$ reduction with an ideality factor i = 1.76.

The surface coverage of the sensitizer in moles/cm^2, Γ, was determined with the modified Beer's law relation given in Equation 2.4,

$$A(\lambda) = \Gamma \cdot \varepsilon(\lambda) \cdot 1000 \tag{2.4}$$

where ε is the molar absorptivity in $M^{-1}cm^{-1}$, λ is the wavelength, and A is the absorbance. The data in Figure 2.2 were collected from a sample with surface coverage $\Gamma = 8.47 \times 10^{-8}$ moles/cm^2. Knowledge of x(E) and Γ enabled determination of the $TiO_2|S$ and the $TiO_2|S^+$ surface coverage at any desired potential.

In an attempt to achieve the flooding conditions necessary for Ostwald isolation, an applied potential was used to maintain a high surface coverage of S^+ such that the $[S^+] >> [TiO_2(e^-)]$ (see Figure 2.3) and the rate law of Equation 2.2 could be reduced to that given in Equation 2.5,

$$rate = k_{obs}[TiO_2(e^-)]^n \tag{2.5}$$

where $k_{obs} = k[S^+]^m$. It was thus necessary to show experimentally that $k_{obs} = k[S^+]^m$ was indeed a constant. This was investigated by nanosecond transient absorption experiments where an incident laser pulse was used to generate $TiO_2(e^-)$s and S^+ in equal numbers far smaller than that present before laser excitation, such that the number of S^+ was essentially constant. The number of $TiO_2(e^-)$s was controlled by the laser fluence.

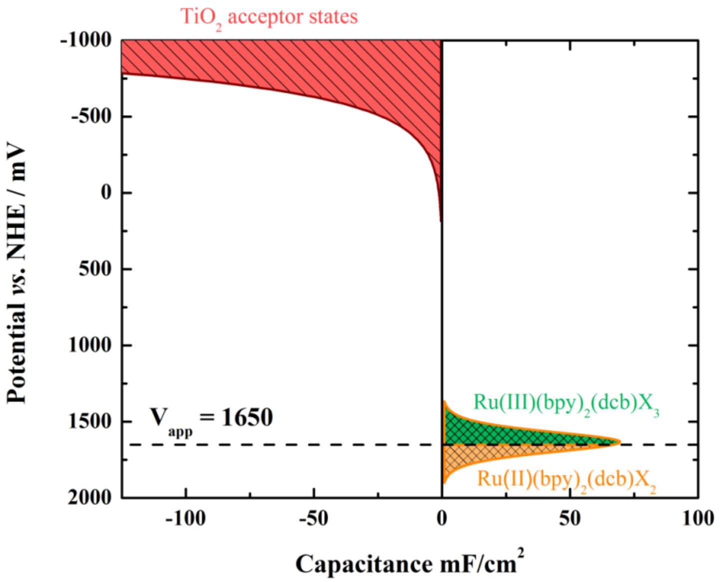

Figure 2.3 The density of states in free energy as measured by the spectroelectrochemical measurements shown in Figure 2.2. The orange line traces out the shaped of the distribution of the $TiO_2|S^{+/0}$ ($Ru^{III/II}$) reduction. The green area under the curve represents the proportion of S^+ present at an applied potential of 1650 mV (dotted black line). The orange area represents the proportion of S^0 at the same applied potential.

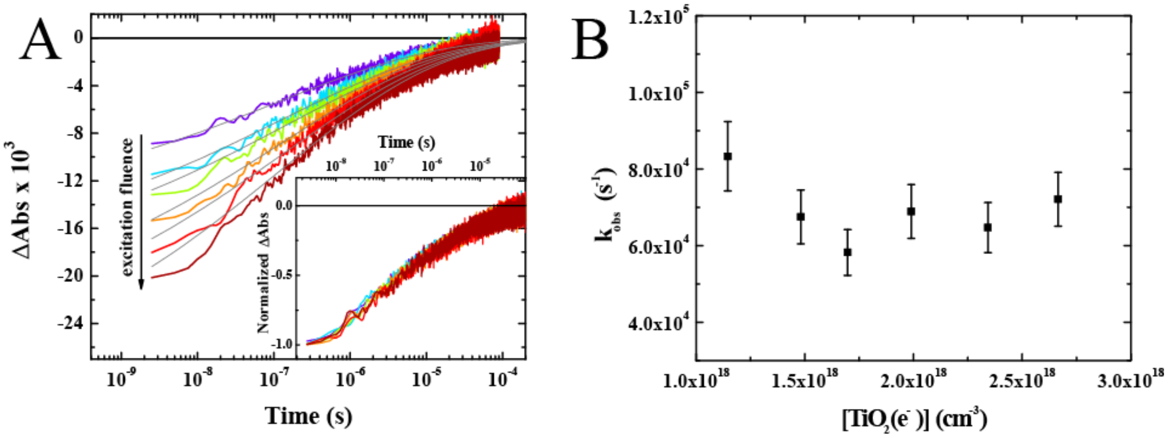

Figure 2.4 A) Absorbance changes of $TiO_2|S$ with an applied potential of 1650 mV monitored at 402 nm after 532 nm pulsed laser excitation. The arrow indicates increasing excitation fluence (~3-7 mJ/pulse). Fits to the KWW function with $\beta = 0.20$ are overlaid in grey. Inset: the same data normalized by dividing by the absolute value of the minimum. B) The observed rate constants of recombination *versus* initial concentration of $TiO_2(e^-)$ in units of e^-/cm^3.

Figure 2.4A shows the absorption change monitored at 402 nm after pulsed 532 nm laser excitation of $TiO_2|S$ with a reverse bias of +1650 mV with varied excitation fluence. The monitoring wavelength of 402 nm was chosen because it represents a ground-excited state isosbestic point that enables characterization of the charge recombination reaction without complications from the excited state.[20] This point was especially relevant under forward bias conditions (*vide infra*). Overlaid on this data are fits to the Kohlrausch Williams-Watts function[26–28] (KWW, grey, Equation 2.6).

$$\Delta A = A_0 e^{(-k_0 \cdot t)^{\beta}} \tag{2.6}$$

The first moment of this function[29] was taken as an 'average' observed rate constant, k_{obs}, with β fixed at 0.20. Figure 2.4B shows plots of k_{obs} versus the initial concentration of $TiO_2(e^-)$. While some scatter does exist, we take this as an artifact of the fitting procedure as the raw experimental data were superposable (Figure 2.4A inset).

It is instructional to consider the 'concentrations' that were used to insure Ostwald isolation conditions. Table 2.1 summarizes the surface coverages, $TiO_2(e^-)$ concentrations, and the observed rate constants measured at each excitation fluence for a potentiostatically controlled sensitized thin film. At this applied potential, approximately 60% of the sensitizers were oxidized corresponding to S^+ surface coverages that remained relatively constant at 5.37 (±0.06) x 10^{-8} moles/cm^2 at all excitation fluences utilized (~3-7 mJ/pulse). As the number of $TiO_2(e^-)$s present in the dark at this positive applied potential was expected to be negligibly small; the number present after light excitation was taken to be equal to the number of photo-oxidized sensitizers measured spectroscopically.[6] The TiO_2 volume was determined based on the film's measured geometrical area, 10 μm thickness, and 50% porosity. Simple division yielded the concentration of injected electrons in units of electrons/cm^3. The pulsed laser fluences employed resulted in a 2.2 fold change in the initial $TiO_2(e^-)$ concentration and the number represented 2-4% of the number of oxidized sensitizers, satisfying the < 10% requirement often asserted as necessary for the isolation method in fluid solution.[18] The number of S^+ was thus determined to be 20-60 fold larger than the number of injected electrons in the range of excitation fluences utilized.

Table 2.1 Surface coverages, $TiO_2(e^-)$ concentrations, and kinetic parameters for the pseudo first-order condition of constant, excess S^+. [a] 10^{-8} moles/cm^2 Γ_{S+} refers to the total surface coverage of S^+, while Γ'_{S+} refers to the contribution of the photo-oxidized sensitizers, [b] 10^{18} cm^{-3}, [c] 10^4 s^{-1}

Data set	Γ_{S+}[a]	Γ'_{S+}[a]	S^+:$TiO_2(e^-)$	$[TiO_2(e^-)]$[b]	k_{obs}[c]
🟥	5.43	0.22	25	2.7	8.7
🟥	5.41	0.19	28	2.3	7.1
🟧	5.38	0.17	33	2.0	7.4
🟩	5.35	0.14	38	1.7	6.4
🟦	5.34	0.12	43	1.5	7.3
🟪	5.31	0.10	56	1.2	8.8

The independence of k_{obs} on the number of injected electrons, under conditions where the oxidized sensitizer concentration remained essentially constant and in large excess, is telling. It shows that $k_{obs} = k[S^+]^m$ is indeed a constant and thus Ostwald isolation has been achieved at a sensitized semiconductor interface. With the Ostwald isolation condition satisfied, the kinetic data was only influenced by the concentration of $TiO_2(e^-)$. Even with changing the initial $[TiO_2(e^-)]$ the data were superposable, which implies that the lifetime was constant with respect to initial $[TiO_2(e^-)]$. Only first-order kinetics permit constancy of the lifetime with changing initial reactant concentration, ergo the order of $TiO_2(e^-)$ must be 1 (see section 2.5 Supporting Information for expressions of lifetime for various reaction orders). This is particularly

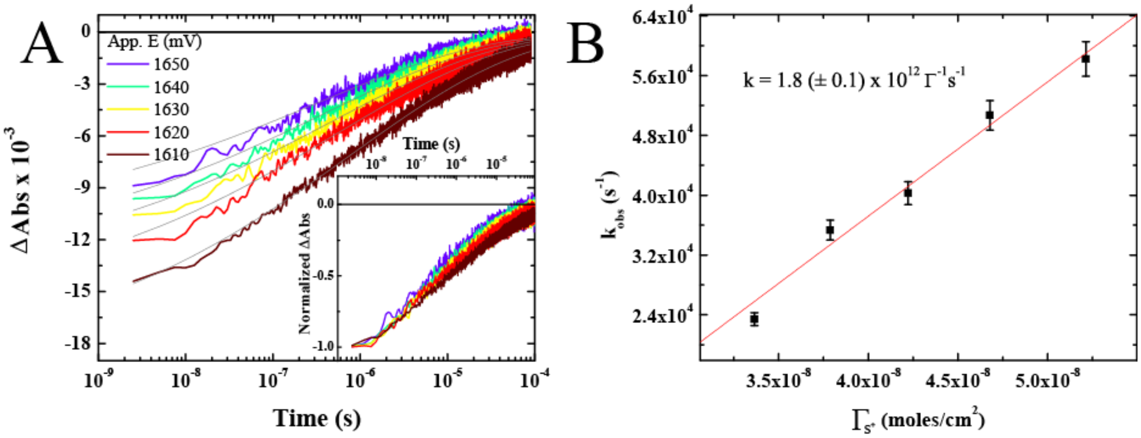

Figure 2.5 A) The absorption change after pulsed 532 nm laser excitation of $TiO_2|S$ monitored at 402 nm with the indicated applied potentials. Excitation fluence was 3.1 mJ/pulse. Fits to the KWW function are overlaid. Inset: The same data normalized by dividing by the absolute value of the minimum. B) The observed rate constants of charge recombination plotted against initial surface coverage of S^+. The overlaid linear fit yielded a second order rate constant of 1.8(±0.1) x 10^{12} $cm^2 mole^{-1} s^{-1}$.

Table 2.2 Applied potential E_{app}, fractional abundance of S^+, surface coverages of S^+, and observed rate constants for the pseudo first-order condition of varied, excess S^+. [a] 10^{-8} moles/cm^2 where Γ_{S+} refers to the total surface coverage of S^+, while Γ'_{S+} refers to the contribution of the photo-oxidized sensitizers, [b] 10^4 s^{-1}.

E_{app}	x (S^+)	Γ_{S+}[a]	Γ_{S+}[a]	S^+:$TiO_2(e^-)$	k_{obs}[b]
1610	0.38	3.37	0.15	22	2.3
1620	0.43	3.79	0.13	29	3.5
1630	0.48	4.22	0.11	37	4.0
1640	0.54	4.68	0.10	45	5.1
1650	0.59	5.21	0.19	27	5.8

compelling evidence because it is independent of the error and assumptions introduced by kinetic fitting. Plots of the lifetime as a function of initial [$TiO_2(e^-)$] lead to the same conclusion, albeit with more scatter (see section 2.5 Supporting Information).

The excess of S^+ was potentiostatically varied to ascertain the dependence of k_{obs} on [S^+]. Figure 2.5A shows the change in absorbance of $TiO_2|S$ at 402 nm at the indicated applied potentials after pulsed 532 nm laser excitation. Overlaid on the kinetic data are fits to the KWW function. The inset shows the normalized data, that were not superposable and returned to baseline more rapidly as the potential (and Γ_{S+}) increased. Table 2.2 displays the observed rate constants, fractional abundance and surface coverages of S^+ corresponding to the data presented in Figure 2.5.

Figure 2.5B shows k_{obs} (abstracted from the KWW parameters with β = 0.22) *vs.* Γ_{S+} with an overlaid linear fit that yielded a second-order rate constant of k = 1.8 (±0.1) x 10^{12} $\Gamma^{-1}s^{-1}$. This value could also be expressed as 5.0 x 10^{-16} cm^3 s^{-1} or, with some critical assumptions, in the more familiar units of $M^{-1}s^{-1}$, ~ 3 x 10^5 $M^{-1}s^{-1}$ (supporting information). It should be noted that the intercepts of the linear fit of the data in Figure 2.5B are non-zero. Possible explanations for this include a systematic error in determination of the oxidized sensitizer surface coverage or a change in the charge recombination mechanism at lower surface coverage. It was not possible to investigate this latter possibility while also maintaining isolation conditions. If it were assumed that the deviation from zero was solely due to systematic error, the resulting Γ_{S+} values would still indicate a ~10 fold or greater excess of S^+.

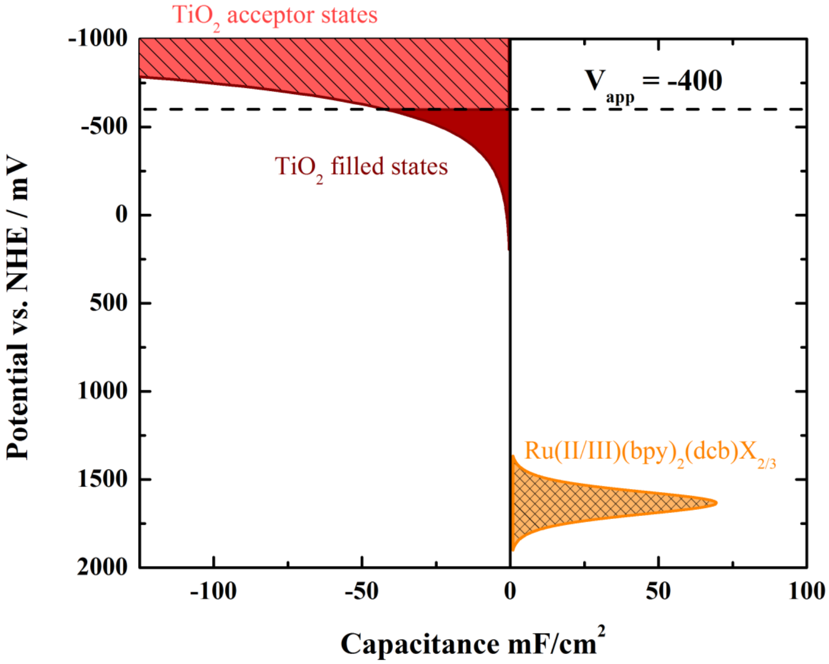

Figure 2.6 The density of states in free energy as measured as has been previously described,[30] under identical conditions as the data shown in Figure 2.2. The dark red area under the exponential density of states curve of the TiO$_2$ represents states that are filled under the condition of -400 mV applied bias (dashed black line), while the light red striped area represents states that are unfilled at the same bias.

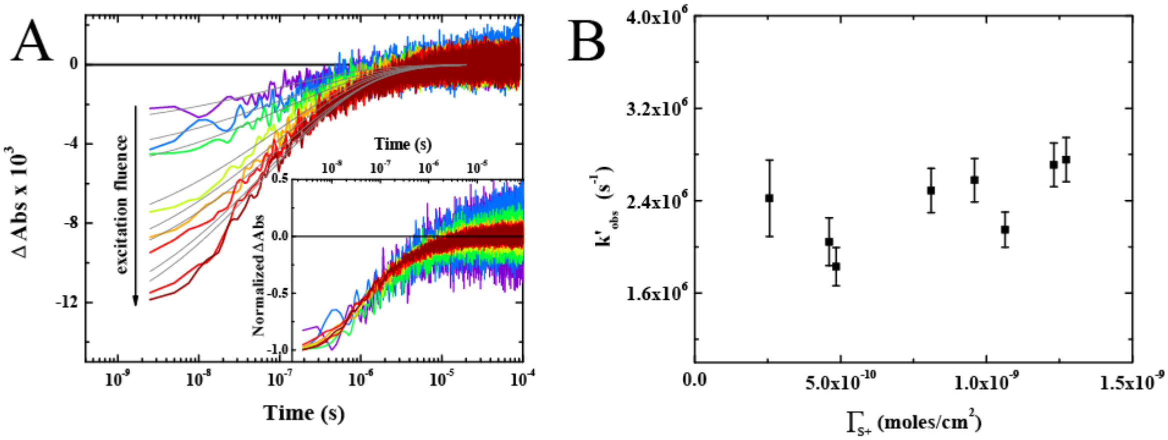

Figure 2.7 A) Absorbance changes of TiO$_2$(e$^-$)|S at -400 mV, monitored at 402 nm after 532 nm pulsed laser excitation. The arrow indicates increasing excitation fluence (~2-7 mJ/pulse). Fits to the KWW function with β = 0.35 are overlaid in grey. Inset: the same data normalized by dividing by the absolute value of the minimum. B) The average observed recombination rate constants *versus* the initial S$^+$ surface coverage.

The same transient absorption studies of a potentiostatically controlled electrode were repeated except with a forward bias such that the dark $TiO_2(e^-)$ concentration was in large excess (see Figure 2.6) and essentially constant and Equation 2.2 reduces to rate = $k'_{obs}[S^+]^m$ where k'_{obs} is a constant equal to $k[TiO_2(e^-)]^n$. Figure 2.7A shows an absorbance change that corresponds to interfacial charge recombination measured after pulsed 532 nm laser excitation of a sensitized thin film held at a forward bias of -400 mV. Based on spectroelectrochemical measurements, the dark $TiO_2(e^-)$ concentration was 31.2 x 10^{18} cm^{-3} at this potential. The initial number of $TiO_2(e^-)$s was 20-100 fold larger than the initial number of S^+ created by the laser pulse while the concentration of $TiO_2(e^-)$s varied only slightly with excitation fluence, at 32.2 (±0.7) x 10^{18} cm^{-3} (see Table 2.3).

Table 2.3 Surface coverages, $TiO_2(e^-)$ concentrations, and observed rate constants for the pseudo first-order condition of constant, excess $[TiO_2(e^-)]$. [a] 10^{-8} moles/cm^2 where Γ'_{S+} refers to the contribution of the photo-oxidized sensitizers, [b] 10^{18} cm^{-3}, [c] 10^4 s^{-1}

Data set	Γ'_{S+}[a]	$[TiO_2(e^-)]$[b]	$TiO_2(e^-):S^+$	k'_{obs}[c]
🟫	0.13	32.7	21	280
🟥	0.12	32.7	22	270
🟥	0.11	32.5	25	220
🟧	0.10	32.4	28	260
🟨	0.08	32.2	33	250
🟩	0.05	31.8	54	180
🟦	0.04	31.8	57	200
🟪	0.03	31.5	102	240

Figure 2.7B shows that observed rate constants abstracted from the KWW fit parameters (Equation 2.6 with $\beta = 0.35$) were independent of Γ_{S+}. The kinetic data were noticeably noisier at lower fluences, but were otherwise superposable when normalized (Figure 2.7A inset). Following the same arguments presented for the complementary data in Figure 2.4 (*vide supra*), these data imply that the order of the recombination reaction with respect to S^+ was 1, in accord with the results presented in Figure 2.5B. See supporting information for plots of lifetime as a function of initial surface coverage of S^+.

Figure 2.8A shows the absorbance change measured at the indicated negative applied potentials after pulsed 532 nm laser excitation of

$TiO_2|S$. Overlaid are fits to the KWW model with common β equal to 0.20 for all the kinetic data. The inset shows that the normalized data were non-superposable, with more negative potentials inducing a more rapid recombination with the oxidized sensitizer. However this data did not produce a linear relationship with k'_{obs}, as can be seen in the log-linear plot in Figure 2.8B. Plausible explanations for the non-linear dependence of k'_{obs} on the $[TiO_2(e^-)]$ include the very real possibility that Ostwald isolation was not achieved under *all* the reverse bias conditions reported in Figure 2.8 (see Table 2.4). Demonstration of isolation over a larger potential range was frustrated by sensitizer desorption and/or irreversible chemistry, which occurred particularly at applied potentials more negative than -400 mV. Another explanation for the superlinear increase in k'_{obs} is that the electron transfer contributes more to the recombination mechanism as potential decreases because of the increasing electron mobility in TiO_2 (*vide infra*). It should be emphasized that this kinetic data was not easily interpreted and is consistent with the reports of power-law dependence[7] (see section 2.5 Supporting Information). However, if pseudo first-order behavior was assumed for the data measured at -400 mV, a potential where Ostwald isolation was clearly demonstrated, the second-order rate constant for recombination would be 4.3×10^{-14} cm^3s^{-1} (or ~3×10^7 $M^{-1}s^{-1}$). The recombination rate clearly increased with $[TiO_2(e^-)]$ (see Table 2.4), but the non-linear dependence of k'_{obs} precluded corroboration of the kinetic order of n = 1 for $TiO_2(e^-)$ as determined in the constant reverse bias condition. However, these results do not necessarily conflict with the conclusion of n = 1.

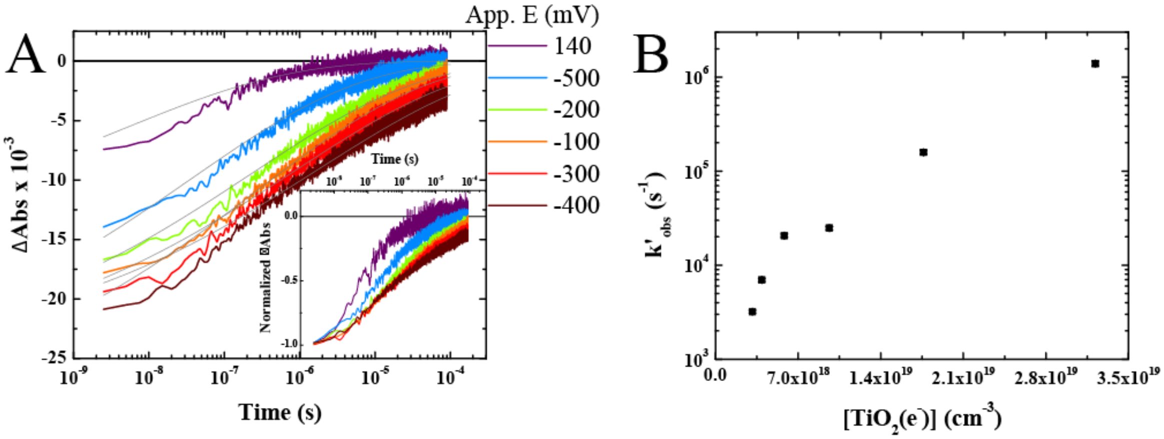

Figure 2.8 A) The absorption change after pulsed 532 nm laser excitation of $TiO_2|S$ monitored at 402 nm with the indicated applied potentials. Excitation fluence was 3.1 mJ/pulse. Fits to the KWW function with β = 0.20 are overlaid. Inset: The same data normalized by dividing by the absolute value of the minimum. B) The k'_{obs} of charge recombination plotted on a log scale against initial concentration of $TiO_2|(e^-)$.

Table 2.4 Surface coverages, $TiO_2(e^-)$ concentrations, and observed rate constants for the condition of varied, excess $[TiO_2(e^-)]$. ^{a} 10^{18} cm^{-3}, $^b10^{-8}$ moles/cm^2, ^{c} 10^4 s^{-1}

E_{app}	$[TiO_2(e^-)]^a$	$\Gamma_{S+}{}^b$	$TiO_2(e^-)$: S^+	$k'_{obs}{}^c$
100	3.1	0.23	1	0.3
0	3.9	0.21	1	0. 7
-100	5.8	0.19	2	2.1
-200	9.7	0.18	5	2.5
-300	17.6	0.15	10	15.9
-400	32.1	0.08	33	139

Demonstration that charge recombination has a first-order dependence on the concentration of both the oxidized sensitizers and the $TiO_2(e^-)$s was an important outcome of this study. This finding was enabled by steady-state and transient absorption experiments of a potentiostatically-controlled sensitized TiO_2 thin film where the concentrations of the oxidized sensitizers or the $TiO_2(e^-)$ were systematically studied. It is worthwhile to briefly review previously reported kinetic data for charge recombination within the framework of a simplified mechanism that links experimentally measured observed rate constants to the elementary steps in the recombination reaction.

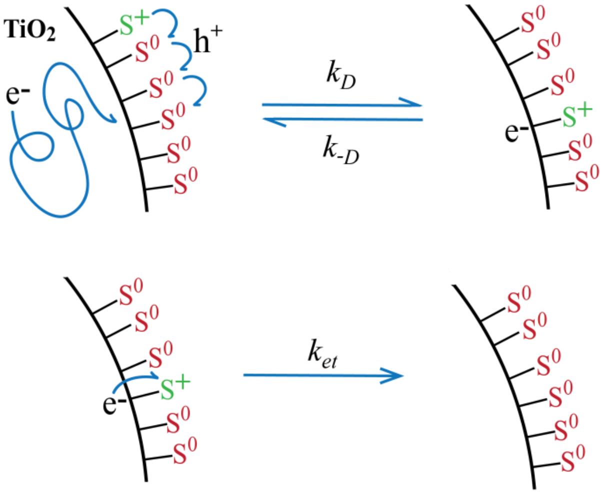

Scheme 2.1 Proposed mechanism of interfacial charge recombination of $TiO_2(e^-)$ and S^+.

On the nanosecond time scale, electron injection and thermalization of the oxidized sensitizer and the injected electron are expected to be complete. Therefore, recombination is proposed to occur by a mechanism that incorporates a pre-equilibrium encounter between the injected electron and the oxidized sensitizer, Scheme 2.1. The encounter occurs through lateral hole hopping by the oxidized sensitizer[31,32] and ambipolar diffusion of the injected electron.[33,34] Although electron transfer will occur over a range of distances, like in fluid solution it is most favored at close contact where orbital overlap is highest. If the rate constant for diffusion away from this close contact, k_{-D}, is comparable to the electron transfer rate constant, k_{et}, the observed rate constant, k_{obs}, contains contributions from both diffusional and electron transfer steps. A steady-state approximation yields Equation 2.7, where $K = k_D/k_{-D}$.

$$\frac{1}{k_{obs}} = \frac{1}{k_D} + \frac{1}{Kk_{et}} \qquad 2.7$$

Interestingly, the vast literature on charge recombination at sensitized TiO_2 interfaces remains unclear as to which mechanistic step(s) the observed 'average' recombination rate constants correspond to. Early studies concluded that diffusion of TiO_2 electrons to the oxidized dye molecules was most important.[7,8] Such behavior corresponds to the kinetic limit where the reaction is controlled by diffusion, i.e. $k_D \leq Kk_{et}$. However, other investigators found that charge recombination was sensitive to the redox potential[5,35] and/or the physical location[5,36] of the molecular sensitizer. In some cases, the observed rate constants were directly related to electron transfer rate constants analyzed in terms of

Marcus theory.[35] This interpretation would correspond to the kinetic limit where diffusion was much slower than electron transfer such that $k_{obs} = K\ k_{et}$.

The data reported here suggest that the intermediate case, where the observed rate constant is comparable to diffusion *and* the electron transfer rate constants, may be the general case when the number of injected electrons is small. Furthermore, the relative weight of these two contributors can be controlled experimentally. Kinetic isolation measurements at more negative potentials clearly revealed a first-order dependence on $[S^+]$. The reaction rate also increased dramatically, as was first reported by Durrant.[13] It is probable that this acceleration is the result of more rapid ambipolar diffusion that also occurs at higher excitation fluences as was revealed previously by classical time-of-flight and intensity modulated photocurrent studies of operational dye sensitized solar cells.[37,38] Hence as the number of $TiO_2(e^-)$s increases, the observed rate constants are expected to more closely reflect the true interfacial electron transfer rate constant.[34] Experimental variables in transient absorption experiments, such as an intense probe beam or high laser repetition rates (that do not allow complete recombination before the subsequent laser pulses), will similarly increase the "dark" $TiO_2(e^-)$ concentration and average observed rate constants abstracted from such data will be larger. The finding here that Ostwald isolation can be utilized to quantify charge recombination provides a means by which such experimental artifacts can be eliminated. Further studies with a larger number of sensitized materials may one day directly provide the critically needed rate constants for the fundamental interfacial electron transfer event *and* diffusion of the injected electron and the oxidized sensitizer.

For this to be realized, an additional issue is that the kinetics for charge recombination display complex kinetics that are not well described by first-order kinetic models. Indeed, early charge recombination studies of dye sensitized TiO_2 revealed that recombination occurred on the 10^{-9} to 10^{-2} s time scale with multi-exponential kinetics, and the slow component was assigned to recombination.[39] The data reported here and elsewhere[20] demonstrate that such modelling is of very limited value unless the concentration dependence is explicitly accounted for, as was recently done.[40] A kinetic model widely used for charge recombination is the Kohlrausch-Williams-Watts (KWW) function that is based on a skewed Lèvy distribution of rate constants,[3,6,7,24] with the first moment often taken as an 'average' observed rate constant. Since the derivation of the KWW function by Scher and Montroll,[28] it has become a paradigm for modelling charge transport in heterogeneous media. However, a statistically good fit to this function in itself does not indicate that recombination is rate limited by transport/diffusion of the charges. More recently, a second-order equal concentration kinetic model has been used that yielded rate constants that were independent of the initial concentration of $TiO_2(e^-)$ and S^+ always generated in equal numbers.[20] This model is consistent with the report here if the 'dark' concentrations of injected electrons and oxidized sensitizers are negligibly small. However, quantification of the full recombination reaction often required a sum of two second-order rate constants.[20] The need for sums or distributions of rate constants to model charge recombination data is not well understood. Heterogeneity may ultimately be the underlying cause of this behavior and identification of the origin(s) of this heterogeneity represent important goals for future research.

2.4 Conclusions

Ostwald isolation has been shown to be applicable as a mechanistic tool for kinetic analysis of charge recombination between surface anchored oxidized dye molecules and electrons injected into mesoporous nanocrystalline TiO_2 thin films. The order of the recombination reaction $TiO_2(e^-)|S^+ \rightarrow TiO_2|S$ was established to be 1 in both oxidized sensitizer and $TiO_2(e^-)$ under conditions where the number of $TiO_2(e^-)$ was low (reverse bias), and 1 for S^+ under conditions where the number of $TiO_2(e^-)$ was high (forward bias). The order of the $TiO_2(e^-)$ in the forward bias condition was not verified, likely as a result of concentration dependent electron diffusion. The application of this approach to other sensitized materials is straight forward provided that the sensitizer is stable in its one-electron oxidized form.

2.5 Supporting Information

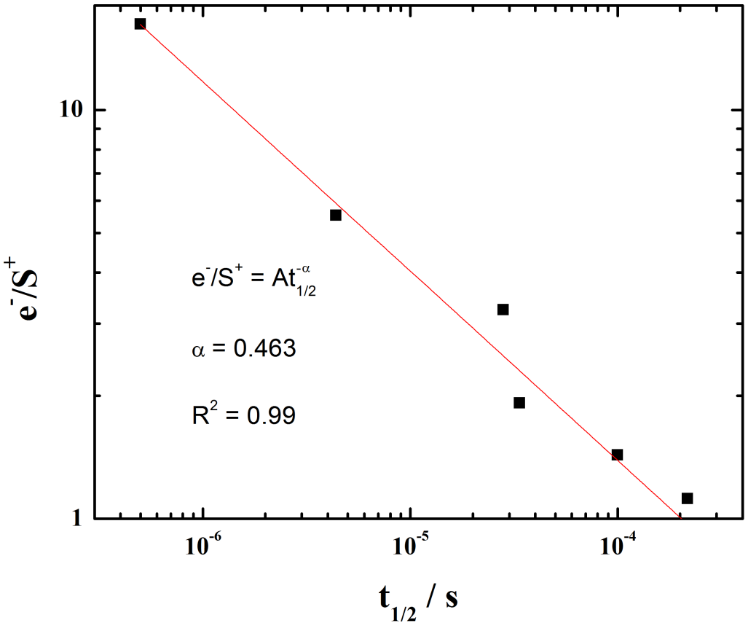

Figure 2.9 Recombination half-lives from 100 to -400 mV *vs.* NHE (or -100 to -600 mV *vs.* Ag/AgCl) analyzed in the same way as described by Nelson et al.[7]

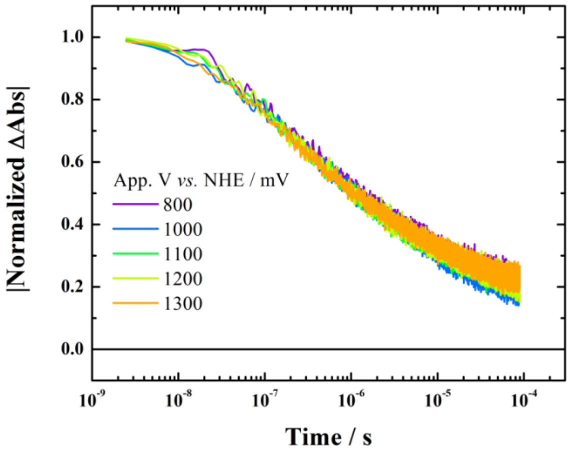

Figure 2.10 The absolute value of the normalized change in absorbance at 402 nm of $TiO_2|S$ at the indicated applied potentials. In the displayed potential range, no appreciable S^+ was formed.

2.5.1 Analysis notes: Conversion between units of surface coverage, molarity, and cm^{-3}

Using the standard expression of surface coverage, Equation 2.8,

$$\Gamma = \frac{moles}{cm^2} \tag{2.8}$$

a second order rate constant in units of $\Gamma^{-1}s^{-1}$ was obtained. To convert to volume instead of area, the surface coverage was multiplied by the thickness of the film scaled by the porosity of 50%. Then, a conversion from cm^3 to liters was used to convert to molarity (Equation 2.9).

$$\frac{cm^2}{mole \cdot s} \cdot (0.5 * 0.001\ cm) \cdot \frac{1\ L}{1000\ cm^3} = \frac{10^{-6} L}{2 \cdot mole \cdot s} \tag{2.9}$$

This is all that was necessary when the measured quantity was the $TiO_2(e^-)$. For the case where the measured quantity was the sensitizer, the distinct volume should be taken into account, as described below.

In order to account for the volume of the nanoparticles that cannot be occupied by the sensitizer, first the volume of a sphere of 10 nm radius was computed (Equation 2.10).

$$\frac{4\pi}{3}(10\cdot 10^{-9}m)^3 = 4.189\cdot 10^{-24}\,m^3 \qquad 2.10$$

Then the volume of the sphere containing the nanoparticle and the sensitizers, with an assumed diameter[41] of 12.75 Å for $Ru^{II}(bpy)_2(dcb)$ (measured in Jmol[42] from distal O to bpy-H) was computed (Equation 2.11).

$$\frac{4\pi}{3}(11.275\cdot 10^{-9}m)^3 = 6.004\cdot 10^{-24}\,m^3 \qquad 2.11$$

The difference between these volumes gave the volume of space available to the sensitizers, and was equal to 2.017 x 10^{-24} m^3. The ratio of the volume available to the sensitizers to the total volume is shown in Equation 2.12.

$$\frac{2.017\cdot 10^{-24}}{6.004\cdot 10^{-24}} = 0.336 \qquad 2.12$$

This ratio was multiplied by the conversion on the RHS of Equation 2.9 to determine molarity of surface-bound molecules (Equation 2.13).

$$\frac{mole}{cm^2}\cdot\frac{1}{0.001\,cm}\cdot\frac{1}{0.5}\cdot\frac{1}{0.336}\cdot\frac{1000\,cm^3}{1L} = 5.95\cdot 10^6\,\frac{mole}{L} \qquad 2.13$$

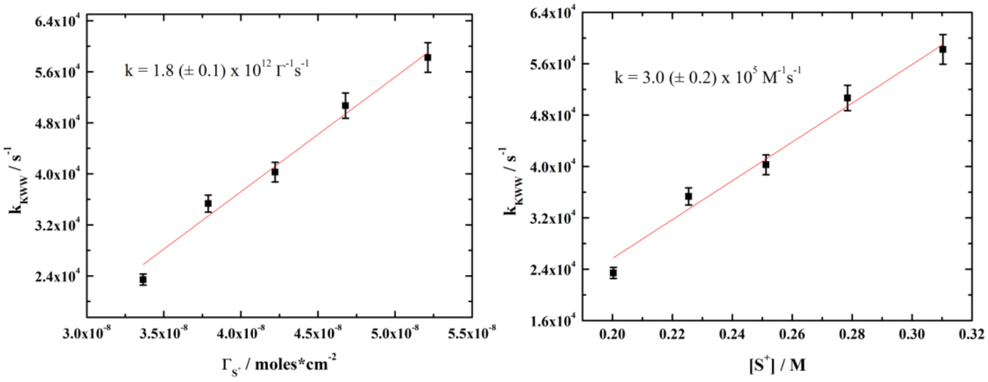

Figure 2.11 Conversion from surface coverage (left) to molarity (right) and subsequent fitting to find the rate constant in each unit.

The plot on the left of Figure 2.11 shows pseudo-first order rate constants plotted *vs.* the surface coverage of oxidized sensitizer, S^+, while the plot on the right shows the same rate constants plotted *vs.* “molar” S^+ concentration, calculated as described above. The second order rate constants obtained from linear fits are shown on the plots. Additionally, the rate constant in terms of Γ^{-1} could be converted to the rate constant in terms of inverse molarity by multiplying by the conversion factor 1.67 x 10^{-7}: 1.8 x 10^{12}*1.67 x 10^{-7}= 3.0 x 10^5, which is consistent with the calculations above.

Similarly, to convert from surface coverage to the units of cm^{-3} (for $TiO_2(e^-)$ only):

$$\frac{mole}{cm^2}\cdot\frac{1}{0.001\ cm}\cdot\frac{1}{0.5}\cdot\frac{6.022\cdot 10^{23}}{1\ mole} = 1.2044\cdot 10^{27}\ cm^{-3} \qquad 2.14$$

Or to convert rate constants in $l^{-1}s^{-1}$ to rate constants in cm^3s^{-1}:

$$\frac{cm^2}{mole \cdot s} \cdot (0.5 * 0.001\,cm) \cdot \frac{1\,mole}{6.022 \cdot 10^{23}} = 8.3029 \cdot 10^{-28} \frac{cm^3}{s} \qquad 2.15$$

2.5.2 Determination of the order of the reactants:

In flooding or isolation conditions, the order of the limiting reactant may be determined by plotting the relationship between the lifetime and the initial concentration of the limiting reactant. Some examples of these relationships are given below. L is used to represent the limiting reactant.

For order of 0:

$$\tau = \frac{[L](1 - e^{-1})}{k} \qquad 2.16$$

For an order of 1/2:

$$\tau = \frac{4[L]^{1/2}\left(e^{1/2} - 1\right)}{e^{1/2}k} \qquad 2.17$$

For an order of 1:

$$\tau = \frac{1}{k} \qquad 2.18$$

For an order of 2:

$$\tau = \frac{e - 1}{2k[L]} \qquad 2.19$$

In summary, for an order less than 1 lifetime is directly proportional to reactant concentration, and for an order greater than one, lifetime is inversely related to initial reactant concentration. The lifetime is only independent of the reactant concentration in the case of an order exactly equal to one. Figure 2.12 A and B show the behavior for the case of limiting S^+ and TiO_2(e-), respectively. The lifetime is plotted against the inverse of the limiting reactant surface coverage or concentration. The observed lack of dependence on the inverse of the initial limiting reactant concentration implies that the reaction was first order in both reactants.

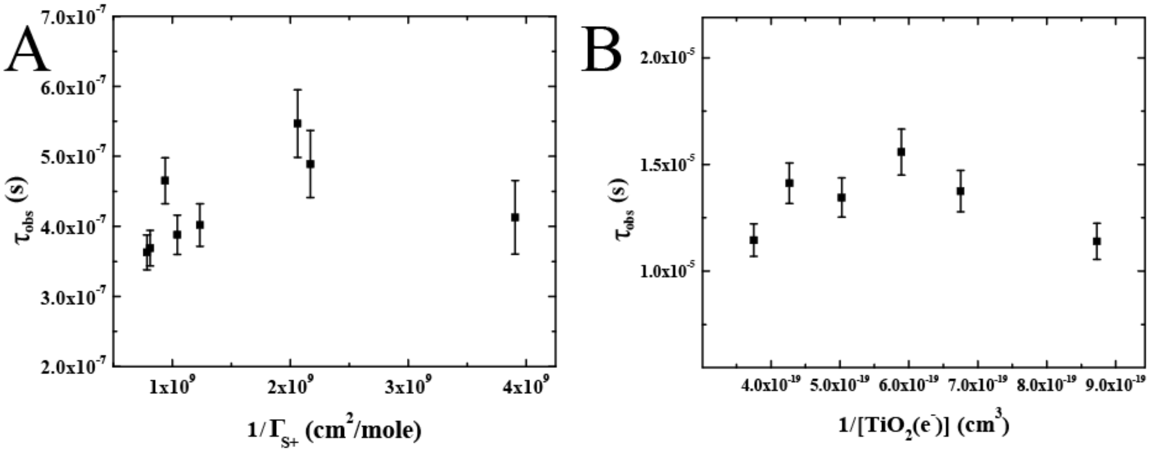

Figure 2.12 The dependence of the lifetime on the inverse concentration of the limiting reactant in flooding conditions. In A) S^+ was the limiting reactant and in B) $TiO_2(e^-)$ was the limiting reactant.

2.6 References

(1) Maggio, E.; Troisi, A. Theory of the Charge Recombination Reaction at the Semiconductor–Adsorbate Interface in the Presence of Defects. *J. Phys. Chem. C* **2013**, *117* (46), 24196–24205.

(2) Bisquert, J. Hopping Transport of Electrons in Dye-Sensitized Solar Cells. *J. Phys. Chem. C* **2007**, *111* (46), 17163–17168.

(3) Nelson, J. Continuous-Time Random-Walk Model of Electron Transport in Nanocrystalline TiO_2 Electrodes. *Phys. Rev. B* **1999**, *59* (23), 15374–15380.

(4) Yan, S. G.; Hupp, J. T. Semiconductor-Based Interfacial Electron-Transfer Reactivity: Decoupling Kinetics from pH-Dependent Band Energetics in a Dye-Sensitized Titanium Dioxide/Aqueous Solution System. *J. Phys. Chem.* **1996**, *100* (17), 6867–6870.

(5) Clifford, J. N.; Palomares, E.; Nazeeruddin, M. K.; Grätzel, M.; Nelson, J.; Li, X.; Long, N. J.; Durrant, J. R. Molecular Control of Recombination Dynamics in Dye-Sensitized Nanocrystalline TiO_2 Films: Free Energy vs Distance Dependence. *J. Am. Chem. Soc.* **2004**, *126* (16), 5225–5233.

(6) Haque, S. A.; Tachibana, Y.; Willis, R. L.; Moser, J. E.; Grätzel, M.; Klug, D. R.; Durrant, J. R. Parameters Influencing Charge Recombination Kinetics in Dye-Sensitized Nanocrystalline Titanium Dioxide Films. *J. Phys. Chem. B* **2000**, *104* (3), 538–547.

(7) Nelson, J.; Haque, S. A.; Klug, D. R.; Durrant, J. R. Trap-Limited Recombination in Dye-Sensitized Nanocrystalline Metal Oxide Electrodes. *Phys. Rev. B* **2001**, *63* (20), 205321.

(8) Hasselmann, G. M.; Meyer, G. J. Diffusion-Limited Interfacial Electron Transfer with Large Apparent Driving Forces. *J. Phys. Chem. B* **1999**, *103* (36), 7671–7675.

(9) Willis, R. L.; Olson, C.; O'Regan, B.; Lutz, T.; Nelson, J.; Durrant, J. R. Electron Dynamics in Nanocrystalline ZnO and TiO_2 Films Probed by Potential Step Chronoamperometry and Transient Absorption Spectroscopy. *J. Phys. Chem. B* **2002**, *106* (31), 7605–7613.

(10) Yella, A.; Lee, H.-W.; Tsao, H. N.; Yi, C.; Chandiran, A. K.; Nazeeruddin, M. K.; Diau, E. W.-G.; Yeh, C.-Y.; Zakeeruddin, S. M.; Grätzel, M. Porphyrin-Sensitized Solar Cells with Cobalt (II/III)–Based Redox Electrolyte Exceed 12 Percent Efficiency. *Science* **2011**, *334* (6056), 629–634.

(11) Robson, K. C. D.; Hu, K.; Meyer, G. J.; Berlinguette, C. P. Atomic Level Resolution of Dye Regeneration in the Dye-Sensitized Solar Cell. *J. Am. Chem. Soc.* **2013**, *135* (5), 1961–1971.

(12) Li, F.; Jennings, J. R.; Wang, Q. Determination of Sensitizer Regeneration Efficiency in Dye-Sensitized Solar Cells. *ACS Nano* **2013**, *7* (9), 8233–8242.

(13) Haque, S. A.; Tachibana, Y.; Klug, D. R.; Durrant, J. R. Charge Recombination Kinetics in Dye-Sensitized Nanocrystalline Titanium Dioxide Films under Externally Applied Bias. *J. Phys. Chem. B* **1998**, *102* (10), 1745–1749.

(14) Hu, K.; Robson, K. C. D.; Johansson, P. G.; Berlinguette, C. P.; Meyer, G. J. Intramolecular Hole Transfer at Sensitized TiO_2 Interfaces. *J. Am. Chem. Soc.* **2012**, *134* (20), 8352–8355.

(15) O'Regan, B.; Moser, J.; Anderson, M.; Graetzel, M. Vectorial Electron Injection into Transparent Semiconductor Membranes and Electric Field Effects on the Dynamics of Light-Induced Charge Separation. *J. Phys. Chem.* **1990**, *94* (24), 8720–8726.

(16) Kamat, P. V.; Bedja, I.; Hotchandani, S.; Patterson, L. K. Photosensitization of Nanocrystalline Semiconductor Films. Modulation of Electron Transfer between Excited Ruthenium Complex and SnO_2 Nanocrystallites with an Externally Applied Bias. *J. Phys. Chem.* **1996**, *100* (12), 4900–4908.

(17) Barnes, P. R. F.; Miettunen, K.; Li, X.; Anderson, A. Y.; Bessho, T.; Gratzel, M.; O'Regan, B. C. Interpretation of Optoelectronic Transient and Charge Extraction Measurements in Dye-Sensitized Solar Cells. *Adv. Mater.* **2013**, *25* (13), 1881–1922.

(18) Espenson, J. H. *Chemical Kinetics and Reaction Mechanisms*; McGraw-Hill: New York, 2002.

(19) Ostwald, W. *Lehrbuch der allgemeinen chemie*; Leipzig, W. Engelmann, 1902; Vol. 2.2.

(20) Kelly, C. A.; Farzad, F.; Thompson, D. W.; Stipkala, J. M.; Meyer, G. J. Cation-Controlled Interfacial Charge Injection in Sensitized Nanocrystalline TiO_2. *Langmuir* **1999**, *15* (20), 7047–7054.

(21) Pavlishchuk, V. V.; Addison, A. W. Conversion Constants for Redox Potentials Measured versus Different Reference Electrodes in Acetonitrile Solutions at 25°C. *Inorganica Chim. Acta* **2000**, *298* (1), 97–102.

(22) Argazzi, R.; Bignozzi, C. A.; Heimer, T. A.; Castellano, F. N.; Meyer, G. J. Enhanced Spectral Sensitivity from Ruthenium(II) Polypyridyl Based Photovoltaic Devices. *Inorg. Chem.* **1994**, *33* (25), 5741–5749.

(23) Bonhôte, P.; Gogniat, E.; Tingry, S.; Barbé, Christophe; Vlachopoulos, N.; Lenzmann, F.; Comte, P.; Grätzel, M. Efficient Lateral Electron Transport inside a Monolayer of Aromatic Amines Anchored on Nanocrystalline Metal Oxide Films. *J. Phys. Chem. B* **1998**, *102* (9), 1498–1507.

(24) Heimer, T. A.; D'Arcangelis, S. T.; Farzad, F.; Stipkala, J. M.; Meyer, G. J. An Acetylacetonate-Based Semiconductor−Sensitizer Linkage. *Inorg. Chem.* **1996**, *35* (18), 5319–5324.

(25) Ardo, S.; Achey, D.; Morris, A. J.; Abrahamsson, M.; Meyer, G. J. Non-Nernstian Two-Electron Transfer Photocatalysis at Metalloporphyrin–TiO_2 Interfaces. *J Am Chem Soc* **2011**, *133* (41), 16572–16580.

(26) Kohlrausch, R. Theorie Des Elektrischen Rückstandes in Der Leidener Flasche. *Ann. Phys. Chem. Leipz.* **1854**, *91*, 56–82.

(27) Williams, G.; Watts, D. C. Non-Symmetrical Dielectric Relaxation Behaviour Arising from a Simple Empirical Decay Function. *Trans. Faraday Soc.* **1970**, *66* (0), 80–85.

(28) Scher, H.; Montroll, E. W. Anomalous Transit-Time Dispersion in Amorphous Solids. *Phys. Rev. B* **1975**, *12* (6), 2455–2477.

(29) Lindsey, C. P.; Patterson, G. D. Detailed Comparison of the Williams–Watts and Cole–Davidson Functions. *J. Chem. Phys.* **1980**, *73* (7), 3348.

(30) Morris, A. J.; Meyer, G. J. TiO_2 Surface Functionalization to Control the Density of States. *J. Phys. Chem. C* **2008**, *112* (46), 18224–18231.

(31) Ardo, S.; Meyer, G. J. Direct Observation of Photodriven Intermolecular Hole Transfer across TiO_2 Nanocrystallites: Lateral Self-Exchange Reactions and Catalyst Oxidation. *J. Am. Chem. Soc.* **2010**, *132* (27), 9283–9285.

(32) Ardo, S.; Meyer, G. J. Characterization of Photoinduced Self-Exchange Reactions at Molecule–Semiconductor Interfaces by Transient Polarization Spectroscopy: Lateral Intermolecular Energy and Hole Transfer across Sensitized TiO_2 Thin Films. *J. Am. Chem. Soc.* **2011**, *133* (39), 15384–15396.

(33) Kopidakis, N.; Schiff, E. A.; Park, N.-G.; van de Lagemaat, J.; Frank, A. J. Ambipolar Diffusion of Photocarriers in Electrolyte-Filled, Nanoporous TiO_2. *J. Phys. Chem. B* **2000**, *104* (16), 3930–3936.

(34) Kambe, S.; Nakade, S.; Kitamura, T.; Wada, Y.; Yanagida, S. Influence of the Electrolytes on Electron Transport in Mesoporous TiO_2−Electrolyte Systems. *J. Phys. Chem. B* **2002**, *106* (11), 2967–2972.

(35) Kuciauskas, D.; Freund, M. S.; Gray, H. B.; Winkler, J. R.; Lewis, N. S. Electron Transfer Dynamics in Nanocrystalline Titanium Dioxide Solar Cells Sensitized with Ruthenium or Osmium Polypyridyl Complexes. *J. Phys. Chem. B* **2001**, *105* (2), 392–403.

(36) Johansson, P. G.; Kopecky, A.; Galoppini, E.; Meyer, G. J. Distance Dependent Electron Transfer at TiO2 Interfaces Sensitized with Phenylene Ethynylene Bridged Ru^{II}–Isothiocyanate Compounds. *J. Am. Chem. Soc.* **2013**, *135* (22), 8331–8341.

(37) Cao, F.; Oskam, G.; Meyer, G. J.; Searson, P. C. Electron Transport in Porous Nanocrystalline TiO_2 Photoelectrochemical Cells. *J. Phys. Chem.* **1996**, *100* (42), 17021–17027.

(38) Fabregat-Santiago, F.; Garcia-Belmonte, G.; Bisquert, J.; Zaban, A.; Salvador, P. Decoupling of Transport, Charge Storage, and Interfacial Charge Transfer in the Nanocrystalline TiO_2/Electrolyte System by Impedance Methods. *J. Phys. Chem. B* **2002**, *106* (2), 334–339.

(39) Bonhôte, P.; Moser, J.-E.; Humphry-Baker, R.; Vlachopoulos, N.; Zakeeruddin, S. M.; Walder, L.; Grätzel, M. Long-Lived Photoinduced Charge Separation and Redox-Type Photochromism

on Mesoporous Oxide Films Sensitized by Molecular Dyads. *J. Am. Chem. Soc.* **1999**, *121* (6), 1324–1336.

(40) Knauf, R. R.; Brennaman, M. K.; Alibabaei, L.; Norris, M. R.; Dempsey, J. L. Revealing the Relationship between Semiconductor Electronic Structure and Electron Transfer Dynamics at Metal Oxide–Chromophore Interfaces. *J. Phys. Chem. C* **2013**, *117* (48), 25259–25268.

(41) Pearson, P.; Bond, A. M.; Deacon, G. B.; Forsyth, C.; Spiccia, L. Synthesis and Characterisation of bis(2,2′-bipyridine)(4-Carboxy-4′-(pyrid-2-Ylmethylamido)-2,2′-bipyridine)ruthenium(II) Di(hexafluorophosphate): Comparison of Spectroelectrochemical Properties with Related Complexes. *Inorganica Chim. Acta* **2008**, *361* (3), 601–612.

(42) Jmol: An Open-Source Java Viewer for Chemical Structures in 3D. Http://www.jmol.org/.

Chapter 3. Driving Force Dependence of Interfacial Charge Recombination under Conditions of Applied Forward Bias

3.1 Introduction

The driving force dependence of interfacial charge recombination between electrons in TiO_2 to oxidized sensitizers, $TiO_2(e^-)|S^+ \rightarrow TiO_2|S$, has been hotly contested for several decades in the literature,[1–8] as was discussed in some detail in section 1.5.1.1 *Driving Force vs. Electron Diffusion Dependence*. As the title of 1.5.1.1 indicates, a large part of the disagreement surrounds whether diffusion of electrons within the TiO_2 particles or the interfacial electron transfer controls the rate of recombination. The focus of this chapter is an attempt to clarify this argument.

Our hypothesis was that control over the rate of recombination depends upon the conditions of the cell.[9] Specifically, that high electron occupancy of the TiO_2 nanoparticles would, by virtue of increased concentration and increased electron mobility, not only increase the rate of electron transfer back to the oxidized sensitizers, but also increase the control of the electron transfer event over the rate of recombination.

Essentially, this work is based upon the mechanism for recombination proposed in the previous chapter, Scheme 2.1.[9]

Since the Marcus equation predicts that the rate of electron transfer depends on driving force,[10] using a series of sensitizers of varied reduction potentials should yield rates of recombination that decrease with increasing driving force for electron transfer (assuming electron transfer is in the Marcus inverted region).[1] Thus, the observation of driving force dependence would show that charge recombination is not solely controlled by electron diffusion within the TiO_2 nanoparticles, but is influenced by the thermodynamics of the electron transfer event.

We find that it is preferable to use the Ru(III/II) reduction potential as a proxy for driving force in evaluating our results, because the reducing power of the $TiO_2(e^-)$ participating in recombination is less well-defined than the readily quantifiable sensitizer reduction potential, and we expect driving force to be linearly related to the sensitizer reduction potentials.[1] In this notation, the more positive reduction potentials have larger driving force, and would therefore have slower electron transfer rate constants.

We assembled a series of sensitizers, shown in Scheme 3.1, to test our hypothesis. The series assumes that the driving force of electron transfer would supersede other molecular factors in influence over the observed charge recombination rate constant. Notably, similar studies have been done in the absence of an applied negative potential used here to increase the electron occupancy.[1,8] The procedure used here is a powerful synthesis of the approaches of Hasselmann and Kuciauskas with that of Haque.[4,6,8]

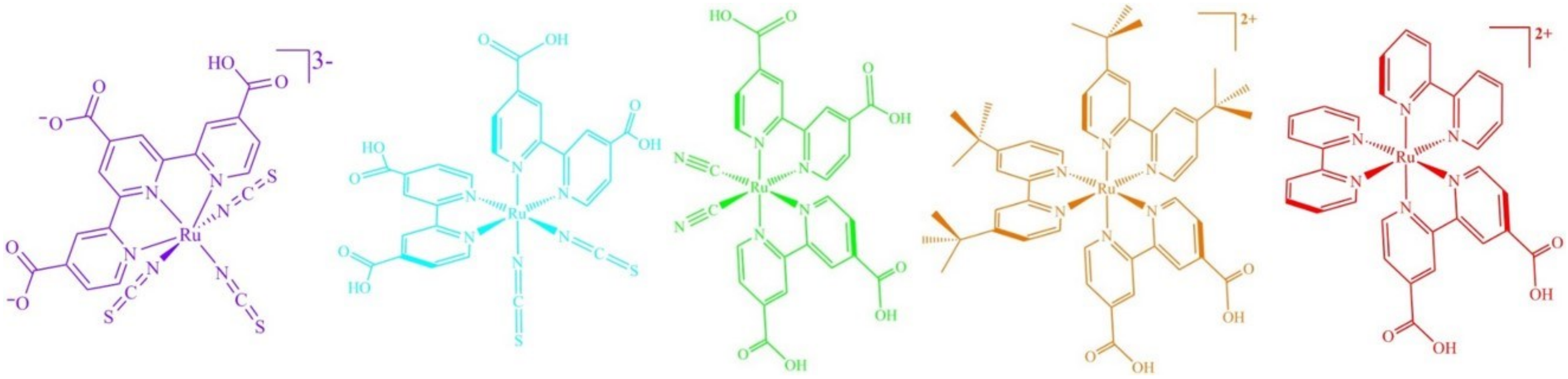

Abbreviation				
Ru(tcpyH)(NCS)$_3$$^{3-}$	Ru(dcb)$_2$(NCS)$_2$	Ru(dcb)$_2$(CN)$_2$	Ru(dtb)$_2$(dcb)$^{2+}$	Ru(bpy)$_2$(dcb)$^{2+}$
Common name				
Black dye	N3	--	YS12	Model compound
E$_{1/2}$(Ru$^{III/II}$)	(V vs. NHE)			
0.94	1.09	1.31	1.45	1.55

Scheme 3.1 The sensitizers used in this study. The reduction potentials for the Black Dye and N3 are from Nazeeruddin *et al.* and Nazeeruddin *et al.*[11,12]

3.2 Experimental Methods

3.2.1 Materials

The following substances were used as received from the provider: argon gas (Airgas, >99.998%), oxygen gas (Airgas, industrial grade), acetonitrile (Burdick and Jackson, spectrophotometric grade), lithium perchlorate (Aldrich, 99.99%), titanium(IV) isopropoxide (Aldrich, 97%), nitric acid (Macron Fine Chemicals, ACS Reagent grade), polyethylene glycol bisphenol A epichlorohydrin copolymer 15,000-20,000 Da (Sigma), fluorine-doped tin oxide coated glass (Hartford Glass Company, Inc., 15 Ω/□, 2.3 mm thick), and glass microscope slides (Fischer Scientific, 1 mm thick). The sensitizers were available from previous studies.

3.2.2 Preparations

3.2.2.1 ***TiO_2 Thin Films***

TiO_2 nanocrystalline thin film electrodes were prepared as previously described.[13] A sol-gel process was used, wherein titanium(IV) isopropoxide was added drop wise to a stirring solution of nitric acid (0.42 mL) in water (60 mL), and brought to 96 °C for several hours, until the volume was reduced to ~20 mL. This opalescent colloid was transferred to a Teflon acid digestion bomb and placed in an oven at 200 °C for 12 hrs and, after cooling, transferred to a glass vial covered in aluminum foil and stirred at 180 rpm. Finely ground polyethylene glycol bisphenol A epichlorohydrin copolymer (~1 g) was added to the stirring Elmer's glue-like substance, and the mixture was allowed to stir for a week or more until the copolymer was completely dissolved. The mixture was then doctor bladed onto fluorine-doped tin oxide glass with cellophane tape as a spacer. After drying for 30-45 minutes, the film was sintered at 450 °C under ~1 atm O_2 flow. The film was stored in the dark at 60-75 °C until needed.

3.2.2.2 ***Sensitization of TiO_2 and ZrO_2***

The TiO_2 electrode or zirconia film on glass was immersed in a 1:1 solution of the sensitizer in CH_3CN:*tert*-butanol and kept sealed in the dark for several days. In some cases, the sensitizer was poorly soluble, and solid sensitizer was present at the bottom of the reaction vial. Before use in experiments, the films were rinsed and immersed in neat acetonitrile for 0.5-2 hours. The resulting sensitized films were referred to as FTO|TiO_2|S and ZrO_2|S.

3.2.3 Profilometry

Measurements were performed by Tyler Motley on a Bruker Dektak XT profilometer using Vision 64 software. The stylus was 12.5 µm in diameter, and exerted a force of 10 mg while collecting data with a resolution of 0.334 µm. The film was measured in the vertical direction in four discrete paths, which were roughly evenly spaced across the ~1 cm width of the film.

3.2.4 Electrochemistry

All experiments were done under positive pressure of solvent-saturated argon after sparging the solution for a minimum of 30 minutes. The Ru(III/II) reduction potentials of YS12, the model compound, and $Ru(dcb)_2(CN)_2$ were measured by cyclic voltammetry with 100 mV/s scan rate in a standard 3-electrode cell, with a platinum disc or mesh counter electrode, an aqueous gel Ag/AgCl Pine mini reference electrode, and an $FTO|TiO_2|S$ working electrode in 300 mM $LiClO_4$ CH_3CN electrolyte solution. All measurements were made using either of the CV 50W or Epsilon-EC potentiostats from Bioanalytical Systems, Inc. (BASi). The reference electrode was calibrated by measuring the reduction potential of ferrocene in the same electrolyte solution before and after each experiment. The reported potential of ferrocene in acetonitrile of +0.63 V vs. NHE was used.[14]

3.2.5 Spectroscopy

All spectroscopic measurements were made at ambient temperature (~20 °C) and all samples were sparged with solvent-saturated argon for at least 30 minutes prior to measurement. In cases where a potential was applied, solvent-saturated argon flow through the head space was maintained throughout the duration of the experiment. UV-Visible absorbance spectra were measured either on a Varian Cary 50 or Agilent Cary 60 spectrophotometer with 1 nm resolution. A 1 cm path length quartz cuvette was used for solution samples. With films, the probe beam was incident on the glass side of the sample at 45° angle.

3.2.5.1 ***Spectroelectrochemistry***

UV-Visible spectra were acquired in the apparatus described above while the applied potential was varied. A standard 3-electrode cell was used with a Pt mesh counter, a Pine Ag/AgCl aqueous gel standard, and the FTO|TiO_2|S working electrode placed at a 45° angle to the probe beam with the probe light passing through the glass before the TiO_2|S. In all measurements, 300 mM $LiClO_4$ CH_3CN electrolyte was used. To apply the potential, a CV50-W BASi potentiostat was used in the CV mode and paused at the potentials of interest. The density of states measurement procedure was modified from a previously described protocol.[15] The absorbance from 798-810 nm was averaged and a molar absorptivity of 1000 $M^{-1}cm^{-1}$ was used. From the absorbance, the surface coverage of electrons was calculated using a modified Beer's Law:

$$A(\lambda) = \Gamma \cdot \varepsilon(\lambda) \cdot 1000 \tag{3.1}$$

In Equation 3.1, A is absorbance, λ is the wavelength, ε is the molar absorptivity, Γ is the macroscopic surface coverage in units of moles/cm^2, and 1000 is a conversion factor.

The measurement began at +100 mV vs. NHE and proceeded by intervals of 50-100 mV in the negative direction, until at least -800 mV. A minimum of 4 minutes wait time at each potential was observed before recording the spectrum to ensure quasi-equilibrium conditions were reached.

3.2.5.2 ***Nanosecond transient absorption spectroscopy***

Spectra were collected on a previously described apparatus.[16] A combination of KV 370 nm and GG 385 nm long pass filters were used between the 150 W Xenon arc lamp, which served the probe, and the sample. This was done for all single wavelength kinetics measurements to prevent the discrepancies observed when using long pass filters with different cut off wavelengths. For kinetic data, a minimum of 120 shots were averaged. For full spectra, 30-60 shots were averaged at each wavelength. The transient absorption spectrum of the excited state of each sensitizer was measured either in CH_3CN solution or on zirconia thin films (prepared by Brian DiMarco) immersed in CH_3CN, depending on solubility in CH_3CN. The transient absorption spectrum of each sensitizer on TiO_2 in 300 mM $LiClO_4$ CH_3CN was also measured. Then, several wavelengths were selected for each sensitizer for use in monitoring the charge recombination kinetics at increasingly negative applied potentials. In cases where it was likely that the excited state would still be present when monitoring the change in absorbance on TiO_2 in the above electrolyte, the excited state isosbestic points were used to monitor the change in absorbance solely due to the charge separated state. In cases where the excited state was not an interference, the peaks in the change in absorbance or Stark isosbestic points were used. To apply the potential, a CV50-W BASi potentiostat was used in the chronoamperometry, or “time base,” mode with a standard 3-electrode cell with Pt mesh counter, Pine Ag/AgCl aqueous gel standard, and the FTO|TiO_2|S working electrodes. Each potential was applied until the current stabilized, or for a minimum of 10 minutes, before transient absorption was acquired while the applied potential remained on. The applied potentials used were approximately none, +100, 0, -80, -100, -200, -300, -350, -400, -500 mV *vs.* NHE. Generally, these potentials were applied in the order listed, but in several cases the reversibility was tested by returning to +100 mV and re-measuring transient absorption there between each increasingly negative potential. All kinetics reported here were measured on the same batch of TiO_2 slides (all sintered together), for consistency of electronic and physical properties (i.e. density of acceptor states, film thickness, and porosity).

3.2.6 Modeling of kinetic data

The kinetic data were modeled using the Kohlrausch Williams-Watts stretched exponential function (KWW, Equation 3.2),[17–19] discussed in section 1.5.1.4 *Mathematical fitting functions.*

$$\Delta A = A_0 e^{-(kt)^{\beta}} \tag{3.2}$$

To paraphrase the most relevant information, it is generally preferable to fit all kinetic data that will be compared to each other with the same β parameter. With a shared β value, the fits of the kinetic data have the same distribution function describing the rate constants, so the “average” lifetime (which is the first moment of the stretched exponential function) has the same meaning for all of them. The grouping of the data when fitting has an impact on the results of the analysis, but they could not all share the same β value – the fit would not converge because of the large range of timescales in the data. The kinetic data was grouped by applied potential rather than by the identity of the sensitizer, and share a common β within each applied potential group. This was done for three reasons: 1) When β was shared within the group of each sensitizer with all the applied potentials, a good fit was impossible to achieve. This is because the distribution which the β parameter reflects[20] narrowed with increasingly negative applied potential. 2) The analysis with each kinetic measurement having its own value for β was nonsensical, for the reasons described above. 3) The comparison of greatest interest is not the applied potentials within the group of a sensitizer, but rather between the sensitizers (the reduction potentials of which are place holders for driving forces) at each applied potential.

The time zero also has an effect on the fitting results of KWW, and in this chapter time zero was set to the peak of the initial amplitude for all data sets.

3.3 Results

The batch of TiO_2 films used to produce the data presented here was characterized by profilometry and spectroelectrochemistry. According to profilometric measurements, the films were approximately 4 µm thick and relatively uniform, see

Figure 3.1. Based on the profilometry, the dimensions of each film were approximately 16x10x0.0038 mm. The density of states measurement, Figure 3.2, was done by a spectroelectrochemical method in a standard 3 electrode cell with a Pt mesh counter electrode, aqueous Ag/AgCl reference, and the FTO|TiO_2 working electrode in 300 mM $LiClO_4$ CH_3CN. The data shown in Figure 3.2 was used in conjunction with the thickness measurement to calculate the number electrons, and hence the electron concentration, at each applied potential, Table 3.1. See section 2.5.1 Analysis notes: Conversion between units of surface coverage, molarity, and cm^{-3} for an explanation of how this was done.

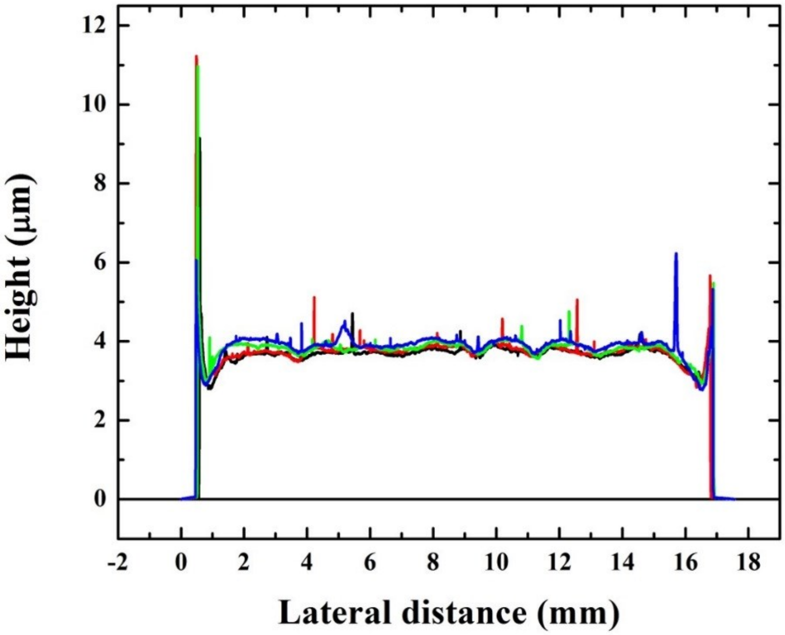

Figure 3.1 Profilometric measurements of a representative sample of FTO|TiO_2. The height of the film is shown on the vertical axis, and the distance in mm from the beginning of the measurement is shown on the horizontal axis. The film was measured in the vertical direction in four discrete paths, roughly evenly spaced across the ~1 cm width of the film. Each path is shown in a different color on the plot. The dimensions of each film were approximately 16x10x0.0038 mm.

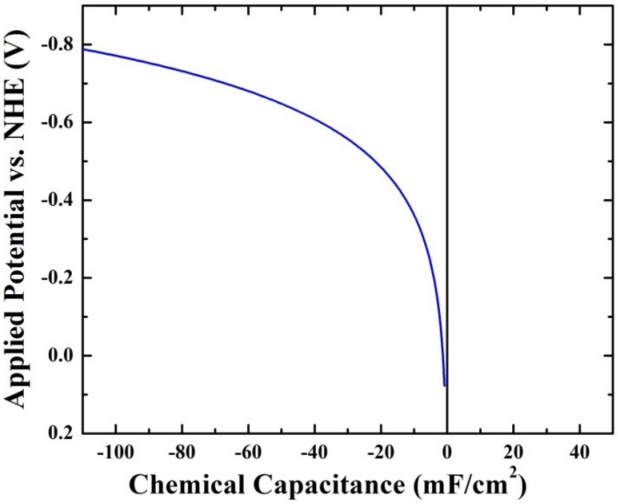

Figure 3.2 The density of states in free energy of a typical sample, calculated using the average absorbance from 798-810 nm and an extinction coefficient of 1000 $M^{-1}cm^{-1}$.

Table 3.1 Electron surface coverages and “concentrations” at the relevant applied biases. Based upon the measured density of states in free energy shown in Figure 3.2, a porosity of 0.5, and a thickness of 4 μm.

Applied Potential (mV vs NHE)	$\Gamma(e^-)$ (moles/cm^2 x 10^{-9})	$[TiO_2(e^-)]$ (M x 10^{-16})
-500	39.9	79.8
-400	22.8	45.6
-350	17.5	34.5
-300	13.1	26.1
-200	7.5	14.9
-100	4.3	8.5
-80	3.8	7.6
0	2.4	4.8
+100	1.6	3.1

The transient absorption data for each dye is presented sequentially in the following pages, and the data are combined for comparison afterword in Figure 3.27. The sensitizers are presented in order of increasing Ru(III/II) reduction potential, and therefore increasing driving force for recombination, with the Black Dye first.

Figure 3.3 shows the absorbance spectrum of the Black Dye in CH_3CN before and after the transient absorption experiment that produced Figure 3.4, which shows the change in absorbance after pulsed 532 nm laser excitation of the same solution. The average time constant from exponential fits of the change in absorbance at 380, 440, 510, and 580 nm gave an excited state lifetime of 26 ns for the Black Dye in acetonitrile.

Figure 3.5 shows the absorbance of the Black Dye anchored to TiO_2, abbrev. FTO|TiO_2|BD, before and after the transient absorption experiment that yielded the data in Figure 3.6, which shows the change in absorbance after pulsed 532 nm laser excitation of the same sample. These spectra correspond to the charge separated state, where the Black Dye has injected an electron into TiO_2. The MLCT transitions decreased, while another absorption appeared at wavelengths longer than 660 nm, which is commonly attributed to a ligand-to-metal charge transfer from the isothiocyanates.[21–24] When the spectra were normalized, there was no evidence for the presence of excited state; therefore, the peak of the bleach, 430 nm, was used for the collection of charge recombination kinetics.

Figure 3.8 shows the change in the absorbance of FTO|TiO_2|BD, at the indicated applied potentials, in 300 mM $LiClO_4$ CH_3CN after 532 nm laser excitation. As the applied potential became more negative, the amplitude of the initial change in absorbance decreased, as can be seen in Figure 3.8 Top. The origin of this effect is unclear — it could be due to either or both increased ultrafast recombination, or decreased injection due to the partial filling of the TiO_2 acceptor states — but it is consistent with previous observations. In addition, the recombination proceeds to completion faster as the applied potential became more negative. This effect is best illustrated in Figure 3.8 Bottom, where the data are normalized at t = 0. The kinetic data were fit with the KWW function, and the resultant rate constants are later discussed in the context of the rest of the sensitizers, see Table 3.2.

It was also noted that the absorbance spectrum of the FTO|TiO_2|BD sample was hypsochromically shifted after the measurement of recombination kinetics under negative applied potentials, see Figure 3.7. This change was irreversible — the sample did not return to its previous absorbance even after prolonged application of a positive potential. This change was not observed after the transient absorption measurement without negative applied potential (Figure 3.5), and was reproduced in spectroelectrochemical experiments which did not involve laser excitation, Figure 3.9 Left. It was therefore concluded that the shift was the sole result of the applied negative potential. It is unclear why a negative applied potential would give such an effect, but it could be due to a change in the TiO_2 that affected the field experienced by the sensitizer, which is not without precedent.[25–27] This idea is reinforced by the similarity of the difference spectrum of the Black Dye on TiO_2 before and after application of – 800 mV and before and after the addition of $LiClO_4$ to the CH_3CN solution, see Figure 3.9 Right.

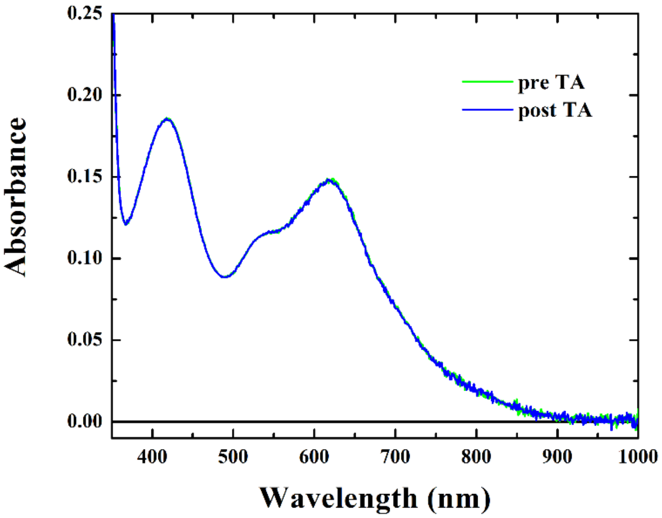

Figure 3.3 The absorbance of the Black Dye in CH_3CN before and after the transient absorption experiment.

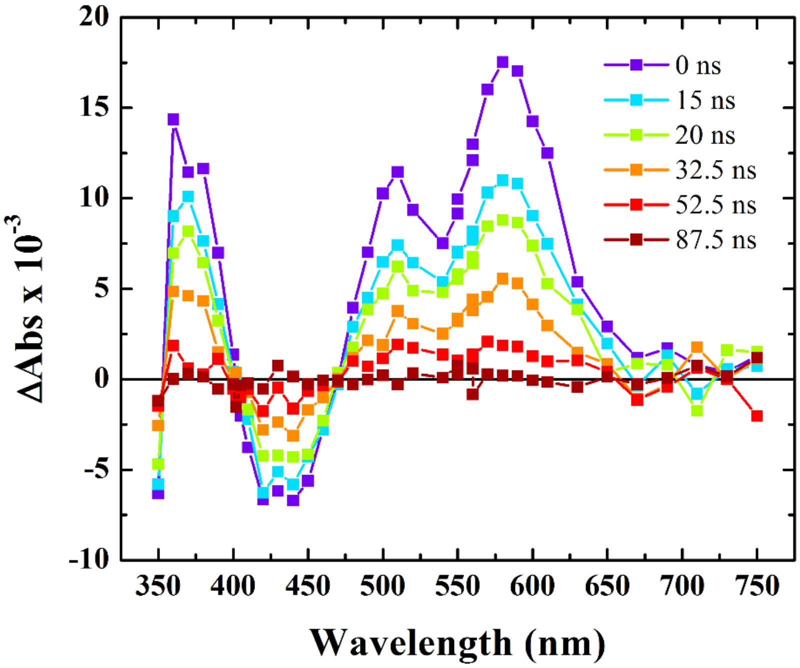

Figure 3.4 The change in absorbance of a CH_3CN solution of the Black Dye at the indicated times after 532 nm pulsed laser excitation.

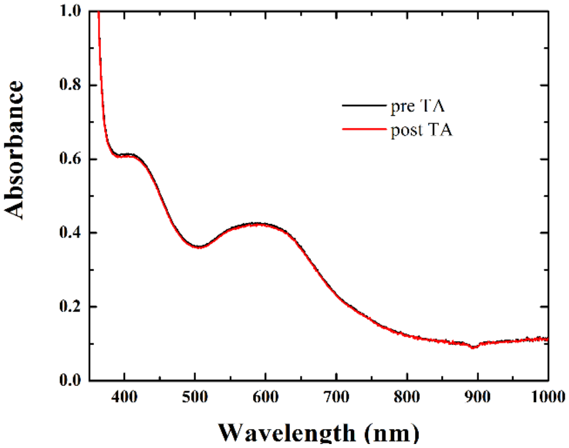

Figure 3.5 The absorbance of FTO|TiO$_2$|BD in 300 mM LiClO$_4$ before and after the transient absorption experiment which yielded the data in Figure 3.6.

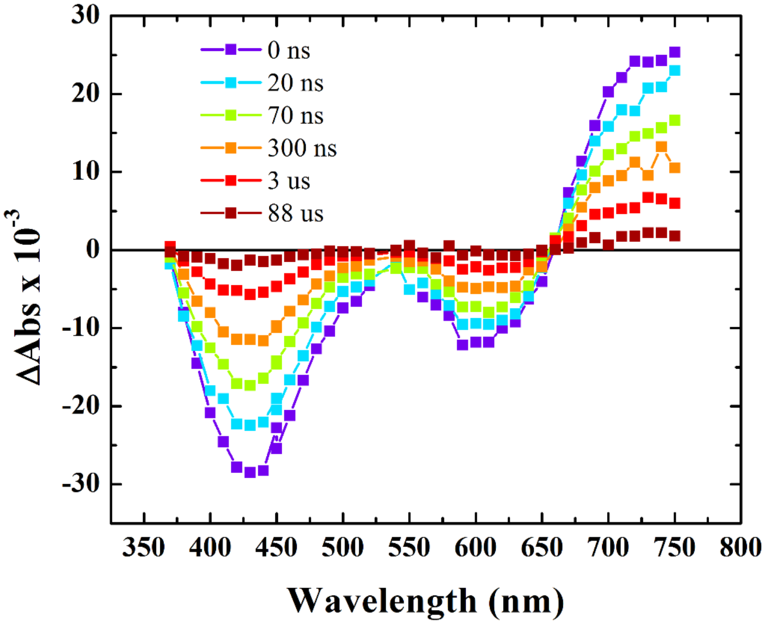

Figure 3.6 The change of absorbance of FTO|TiO$_2$|BD in 300 mM LiClO$_4$ at the indicated times after pulsed 532 nm laser excitation.

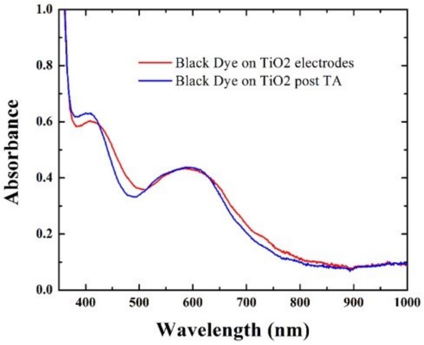

Figure 3.7 The absorbance of FTO|TiO_2|BD in 300 mM $LiClO_4$ before and after the transient absorption experiment, which yielded the data in Figure 3.8.

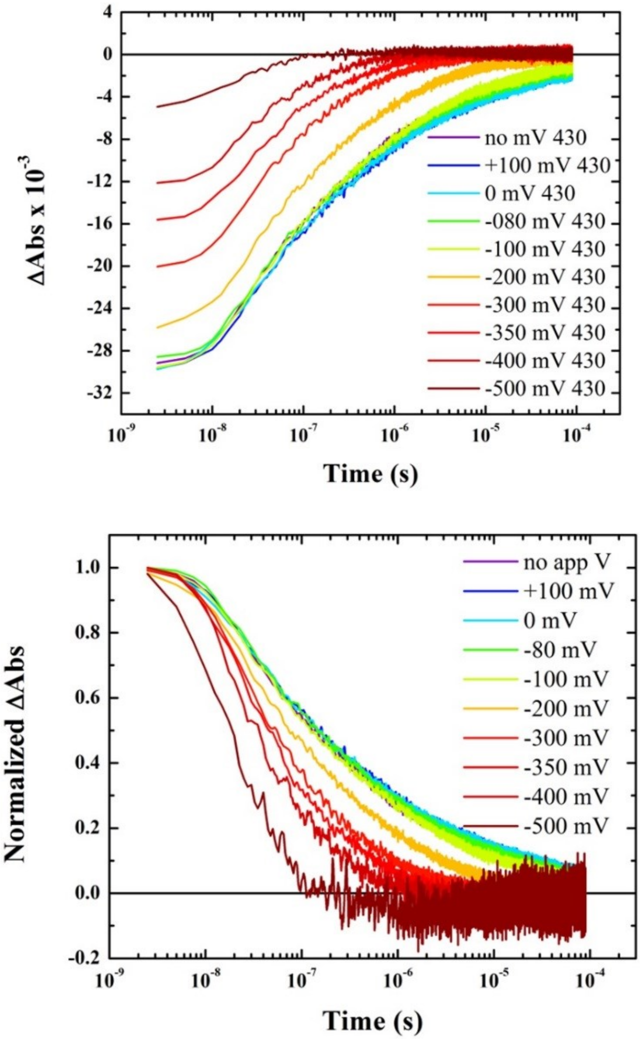

Figure 3.8 Top) The change in absorbance of FTO|TiO_2|BD in 300 mM $LiClO_4$ CH_3CN at 430 nm with the indicated applied potentials. Bottom) The same data normalized at t = 0.

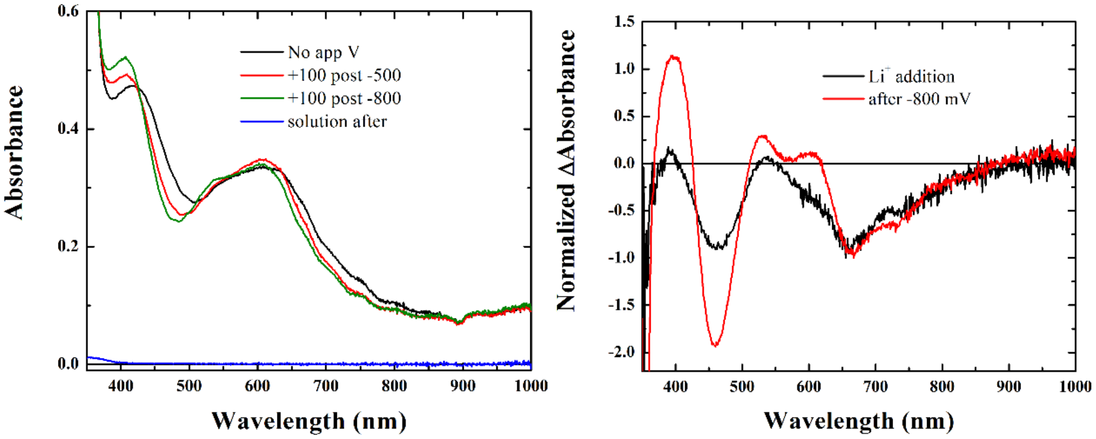

Figure 3.9 Left) The absorbance of FTO|TiO_2|BD in 300 mM $LiClO_4$ CH_3CN with no applied potential (black), with +100 mV after the application of -500 mV (red), and +100 mV after the application of -800 mV (green). Right) The difference spectrum of the FTO|TiO_2|BD before and after addition of $LiClO_4$ to the CH_3CN (black) normalized to the difference spectrum of the same sample before and after -800 mV applied bias (red).

The next sensitizer to be considered is N3. The change in absorbance of a CH_3CN solution (Figure 3.10 Right) of N3 after 532 nm laser excitation is shown in Figure 3.10 Left. The change in absorbance, characterized by the decrease in absorbance of the MLCT transitions and increased absorbance in wavelengths longer than the 588 nm isosbestic point, is due to the excited state of N3. The emission measured at 750, 760, 770, 780, 790, and 800 nm was fit to a single exponential function, and the resulting lifetimes were averaged, yield an excited state lifetime of 24 ns in CH_3CN solution.

The change in absorbance of FTO|TiO_2|N3 in 300 mM $LiClO_4$ CH_3CN after pulsed 532 nm laser excitation is shown in Figure 3.11. This was taken to be entirely due to the charge separated state based on the absence of photoluminescence, the superposability of the normalized difference spectra at all times after excitation, and the long time scale of the disappearance of the change in absorbance. For this reason, the wavelength at which the change in absorbance had the largest amplitude, 520 nm, was used for kinetic data measurements.

Figure 3.13 shows the kinetic data for recombination measured at 520 nm. As with the Black Dye, the initial amplitude decreased with increasing applied potential, Figure 3.13 Top, while the time to completion of charge recombination also decreased, Figure 3.13 Bottom. The increase in rate of recombination was not as pronounced as in the case of the Black Dye. This will be discussed in the following section.

There was a permanent change in absorbance of the sample after measuring the kinetics of charge recombination. This can be seen in Figure 3.12, and was reproduced in a spectroelectrochemical experiment shown in Figure 3.14. Unlike in the case of the Black Dye, the change in absorbance did not have a similar shape as the change in absorbance after addition of $LiClO_4$.

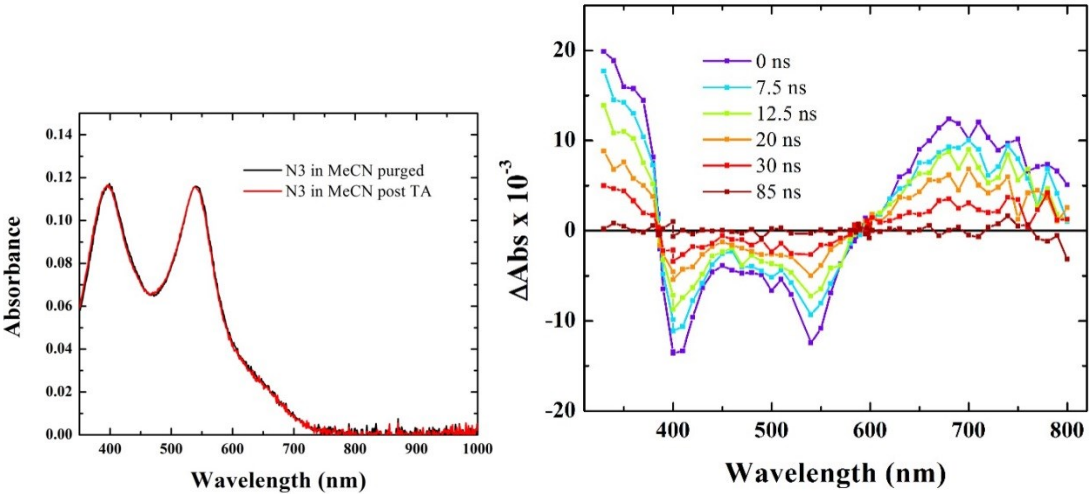

Figure 3.10 Right) The absorbance spectra of N3 in CH_3CN solution before and after the transient absorption. Left) The change in absorbance of N3 in CH_3CN at the indicated times after pulsed 532 nm laser excitation.

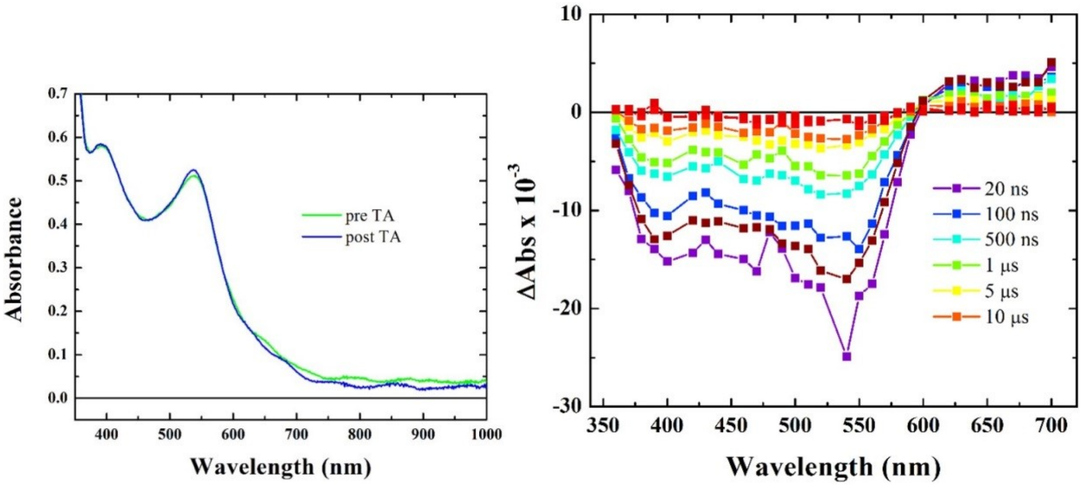

Figure 3.11 The absorbance of FTO|TiO_2|N3 in 300 mM $LiClO_4$ CH_3CN before and after the transient absorption measurement. Left) The change in absorbance of the same sample at the indicated times after pulsed 532 nm laser excitation.

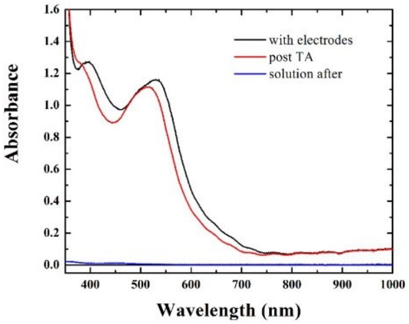

Figure 3.12 The absorbance spectra of FTO|TiO$_2$|N3 in 300 mM LiClO$_4$ CH$_3$CN before and after the transient absorption measurements that yielded Figure 3.13.

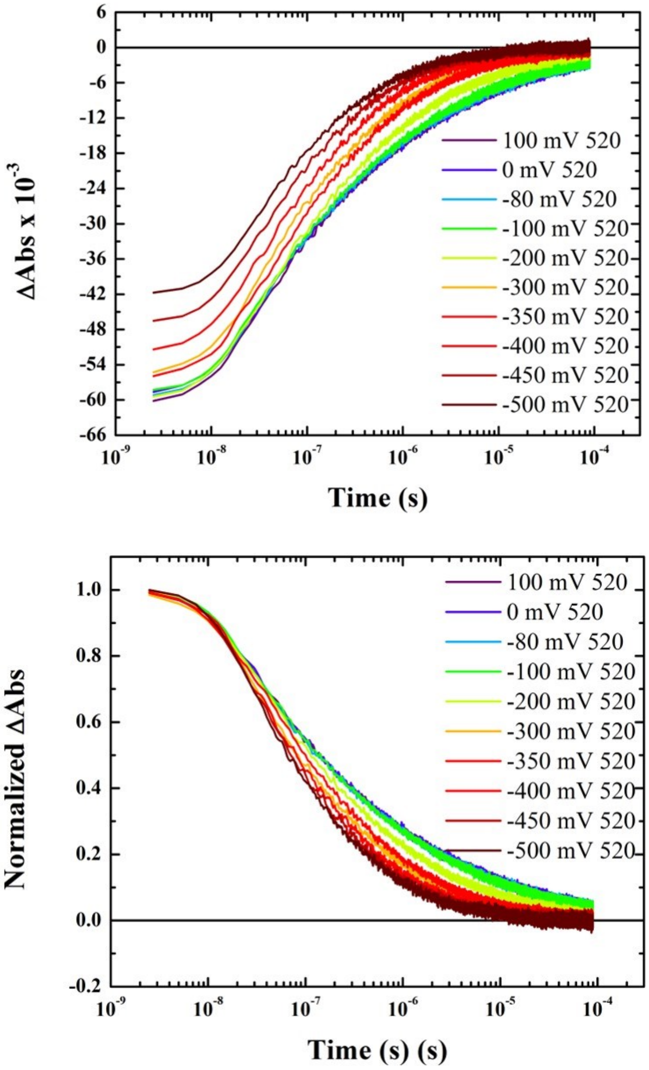

Figure 3.13 Top) The change in absorbance of FTO|TiO$_2$|N3 in 300 mM LiClO$_4$ CH$_3$CN at 520 nm with the indicated applied potentials. Bottom) The same data normalized at t = 0.

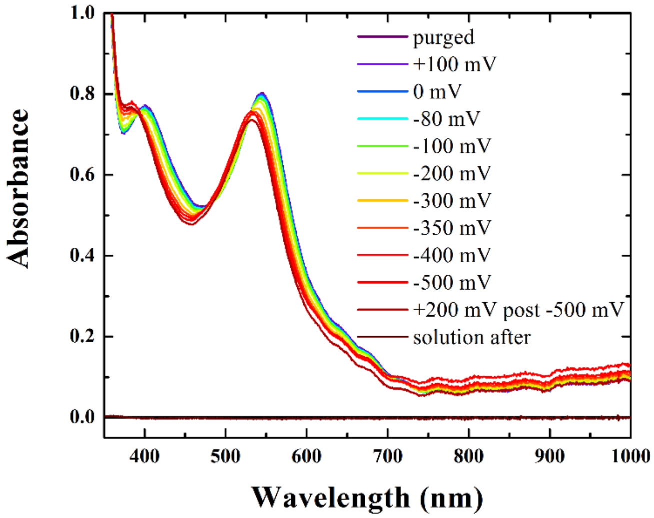

Figure 3.14 The absorbance of FTO|TiO_2|N3 in 300 mM $LiClO_4$ CH_3CN with no applied potential (purged, purple) and with the indicated applied potentials.

The data presented next is from $Ru(dcb)_2(CN)_2$, whose reversible Ru(III/II) reduction potential was measured at 1.31 V vs. NHE when anchored to TiO_2. The change in absorbance of ZrO_2|$Ru(dcb)_2(CN)_2$ after laser excitation is shown in Figure 3.15. There is a decrease in the absorbance of the MLCT centered at ~520 nm, and the beginnings of an increase in absorbance for wavelengths shorter than the ~370 nm isosbestic point and longer than the ~620 nm isosbestic point. The measured emission at 640, 660, 680, and 700 nm was well fit with bi-exponential functions, yielding an average lifetime of 110 ns.

At long time scales, the decrease in the MLCT absorbance shifted to be centered at 500 nm. This shifted absorbance change was longer lived than the original change in absorbance and the measured luminescence

(Figure 3.15 Right). The nature of this feature was clarified by the measurement of the change in absorbance of FTO|TiO_2|Ru(dcb)$_2$(CN)$_2$ after laser excitation, shown in Figure 3.16. Here, the decrease in absorbance of the MLCT is centered at 500 nm, while the increase in absorbance in the small wavelength region seen in the previous case was absent, and a decrease in absorbance at all wavelengths smaller than the ~620 nm isosbestic point was observed. The difference spectra were superposable for all times shown, although some short-lived (τ < 40 ns) luminescence was observed. This change in absorbance closely matched the long-lived difference spectrum of ZrO_2|Ru(dcb)$_2$(CN)$_2$, suggesting that some injection occurred on zirconia.

In the measurement of recombination kinetics, several wavelengths were explored, but it was found that the same results were achieved with the excited state isosbestic points as with the maximum of the decrease in the MLCT absorbance at 500 nm. Since the signal to noise at the isosbestic points of the excited state was low, the data at 500 nm is shown in Figure 3.18. As with the other sensitizers, increasingly negative applied potential was accompanied by decreasing initial amplitude of the change in absorbance (Figure 3.18 Top), and to more rapid charge recombination (Figure 3.18 Bottom).

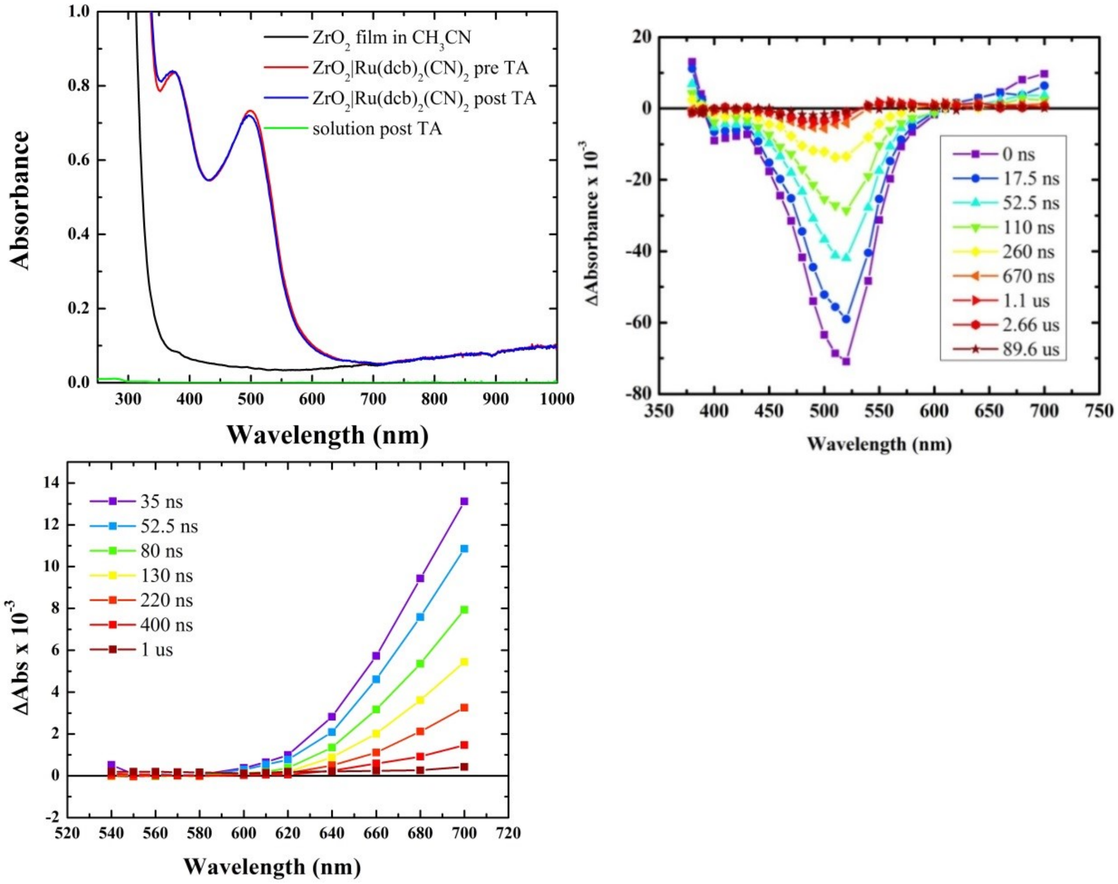

Figure 3.15 The change in absorbance of $FTO|ZrO_2|Ru(dcb)_2(CN)_2$ in CH_3CN at the indicated times after pulsed 532 nm laser excitation.

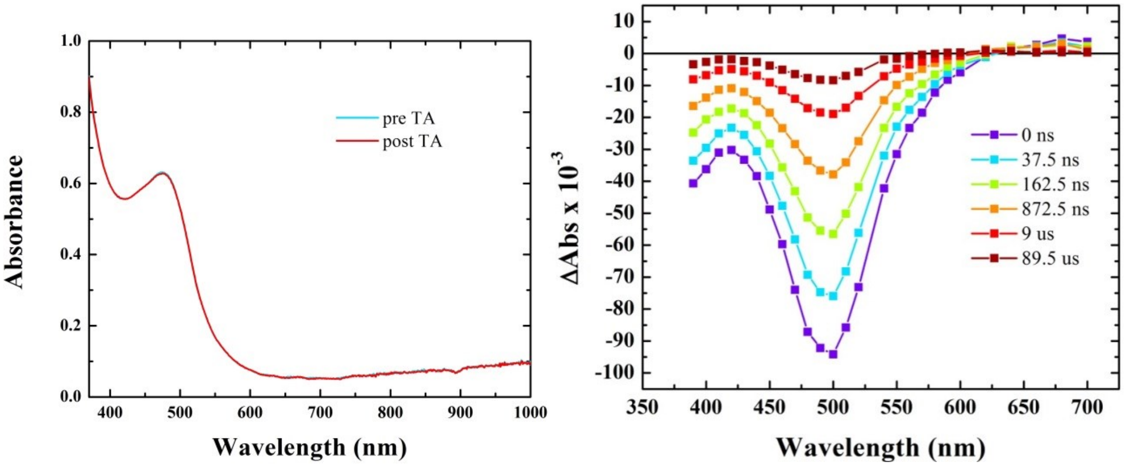

Figure 3.16 The change in absorbance of $FTO|TiO_2|Ru(dcb)_2(CN)_2$ in 300 mM $LiClO_4$ CH_3CN at the indicated times after pulsed 532 nm laser excitation.

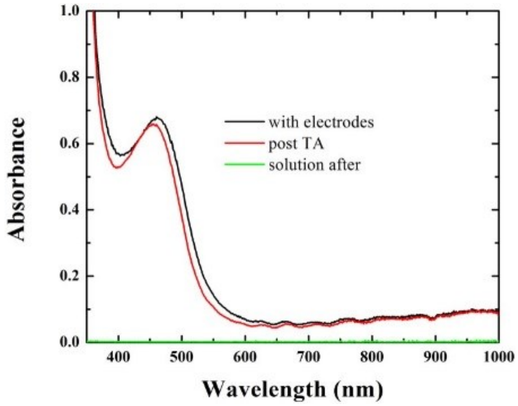

Figure 3.17 The absorbance of FTO|TiO_2|$Ru(dcb)_2(CN)_2$ in 300 mM $LiClO_4$ CH_3CN before (black) and after (red) the transient absorption experiment that yielded the data in Figure 3.18.

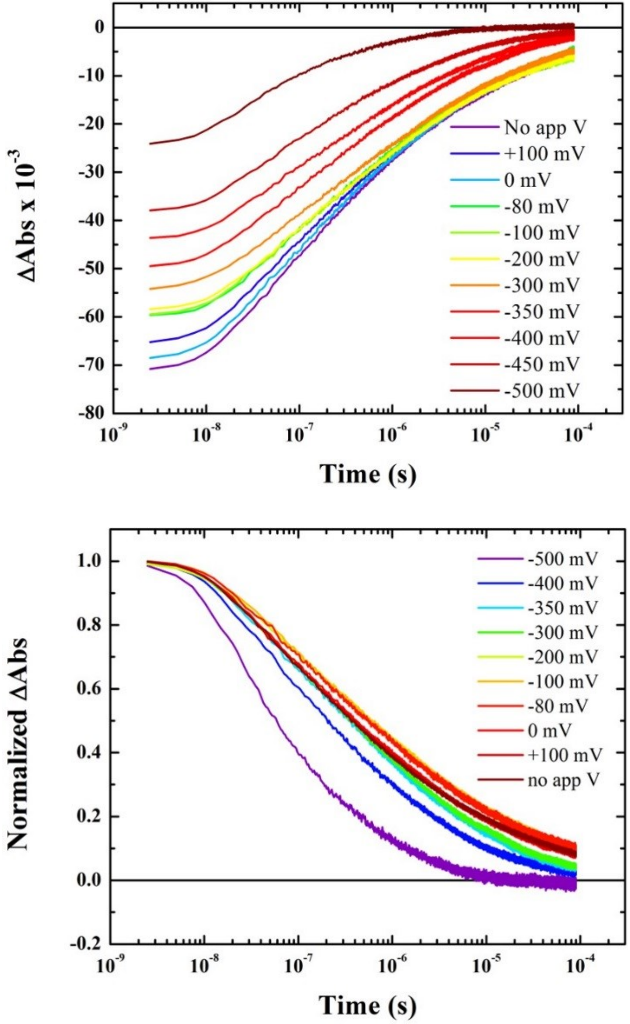

Figure 3.18 Top) The change in absorbance of FTO|TiO_2|$Ru(dcb)_2(CN)_2$ in 300 mM $LiClO_4$ CH_3CN at 500 nm with the indicated applied potentials. Bottom) The same data normalized at t = 0.

$Ru(dtb)_2(dcb)^{2+}$, also called YS12, had a measured Ru(III/II) reduction potential of 1.45 V vs NHE when anchored to TiO_2. YS12 has been used for as a probe for the interfacial electric field emanating from TiO_2 particles following photo-induced electron injection because it shows a relatively large Stark effect.[25,26,28] This was taken into account when the wavelength for charge recombination kinetics measurements was chosen. The change in absorbance of $ZrO_2|Ru(dtb)_2(dcb)^{2+}$ after laser excitation is shown in Figure 3.19. There was a broad decrease in the MLCT absorbance centered at 460 nm, and an increase in the absorbance for wavelengths shorter than the 403 nm isosbestic point. A small increase in absorbance after the 520 nm isosbestic point was also present. The spectra were superposable when normalized, and this change in absorbance was assigned as the excited state difference spectrum. The measured emission at 660 nm was well fit using a tri-exponential function. The average lifetime based on this fit was 720 ns.

The change of absorbance of $FTO|TiO_2|Ru(dtb)_2(dcb)^{2+}$, by contrast, did not have the increase in absorbance at wavelengths shorter than 403 nm. Instead, there appears to be an isosbestic point for the decrease in absorbance at the edge of our detection, approximately 350 nm. The decrease in absorbance of the MLCT transition is also more structured, with two separate maxima in the change, at ~410-420 nm and 490 nm.

Several monitoring wavelengths were explored for the measurement of recombination kinetics, but in the end the isosbestic point of the excited state, 403 nm, was chosen as the most representative of the charge separated state, since the excited state does not contribute to the change in absorbance. The kinetic data for recombination with varied applied potential are shown in Figure 3.21. After an initial decrease in amplitude like the rest of the sensitizers, there was a recovery at -350 mV applied potential, and the decrease in initial amplitude proceeded again afterwards (Figure 3.21 Top). This behavior was reproducible, and the origin is not known to the author. Despite this lapse in the trend of the initial amplitude, the trend in the rapidity of recombination was not as interrupted at -350 mV (Figure 3.21 Bottom). Instead, it appears that at -300 and -350 mV recombination proceeded at approximately the same speed, which is similar to what was observed in the other sensitizers.

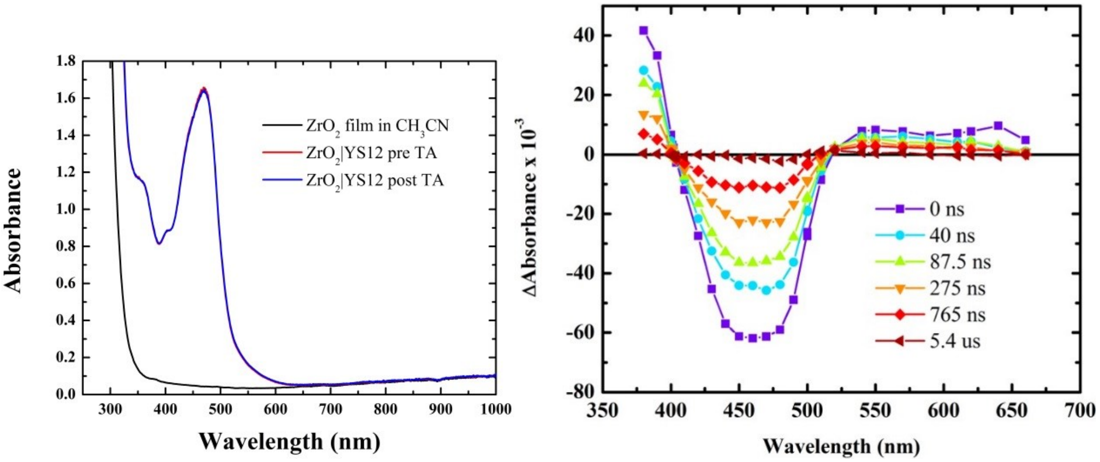

Figure 3.19 The change in absorbance of FTO|ZrO$_2$|YS12 in CH$_3$CN at the indicated times after pulsed 532 nm laser excitation.

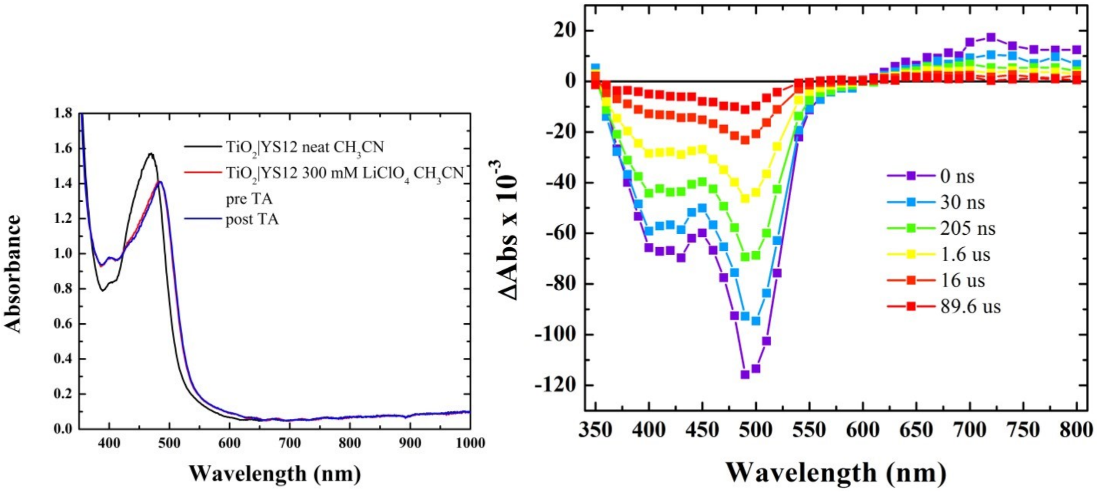

Figure 3.20 The change in absorbance of FTO|TiO$_2$|YS12 in 300 mM LiClO$_4$ CH$_3$CN at the indicated times after pulsed 532 nm laser excitation.

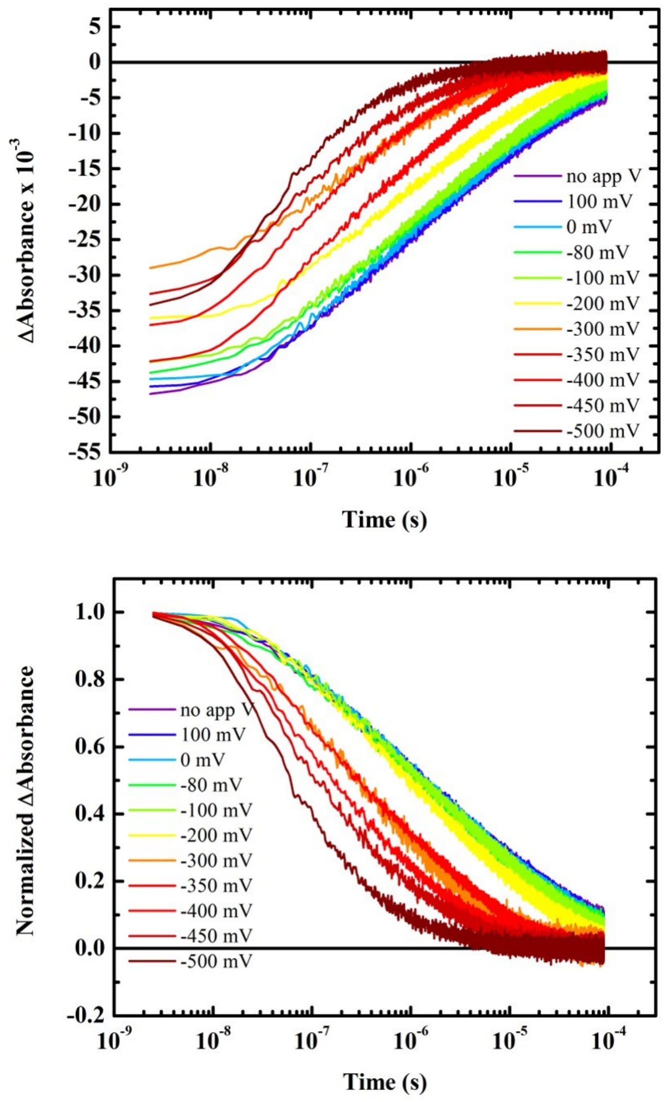

Figure 3.21 Top) The change in absorbance of FTO|TiO_2|YS12 in 300 mM $LiClO_4$ CH_3CN at 403 nm with the indicated applied potentials. Bottom) The same data normalized at t = 0.

The final compound used in this research was the model compound, with a measured Ru(III/II) reduction potential of 1.55 V when anchored to TiO_2. The absorbance spectra of FTO|TiO_2|Ru(bpy)$_2$(dcb)$^{2+}$ before and after transient absorption measurements are shown in Figure 3.22, and the change in absorbance after pulsed 532 nm laser excitation is shown in Figure 3.23. There is a decrease in the MLCT absorbance centered at 490 nm, and an increase in the absorbance at wavelengths longer than the isosbestic point at ~600 nm. There was also significant photoluminescence detected.

It has been reported that the isosbestic point between the excited state and charge-separated state of the model compound is at 402 nm.[13] Since the change in absorbance is substantial at 402 nm for the charge separated state, 402 nm was chosen as the wavelength to monitor charge recombination. Figure 3.24 shows the change in absorbance of FTO|TiO_2|Ru(bpy)$_2$(dcb)$^{2+}$ at 402 nm. As with the other sensitizers, the amplitude of the initial change in absorbance decreased (Figure 3.24 Top) and the rapidity of charge recombination increased (Figure 3.24 Bottom) with increasingly negative applied potential. Notably, the dynamics at -300 and -350 mV were essentially superposable when normalized, similar to what was seen with the YS12 sensitizer.

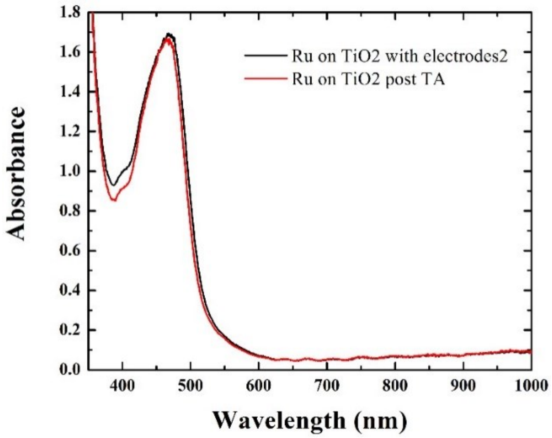

Figure 3.22 The absorbance spectra of FTO|TiO$_2$|Model in 300 mM LiClO$_4$ CH$_3$CN before (black) and after (red) the transient absorption measurements that yielded the data in Figure 3.23.

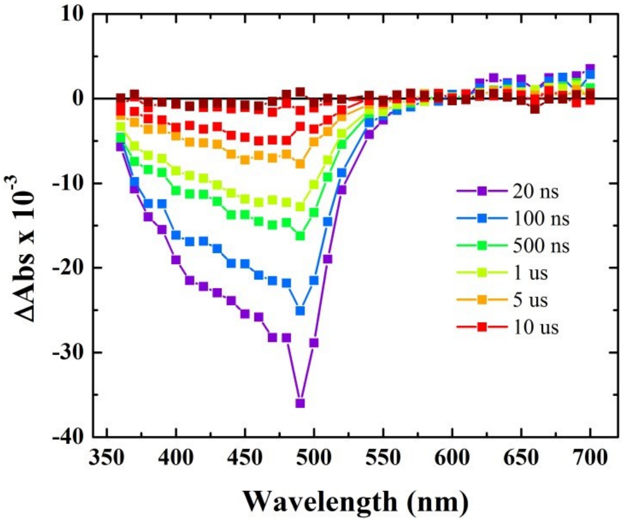

Figure 3.23 The change in absorbance of FTO|TiO$_2$|Model in 300 mM LiClO$_4$ CH$_3$CN at the indicated times after pulsed 532 nm laser excitation.

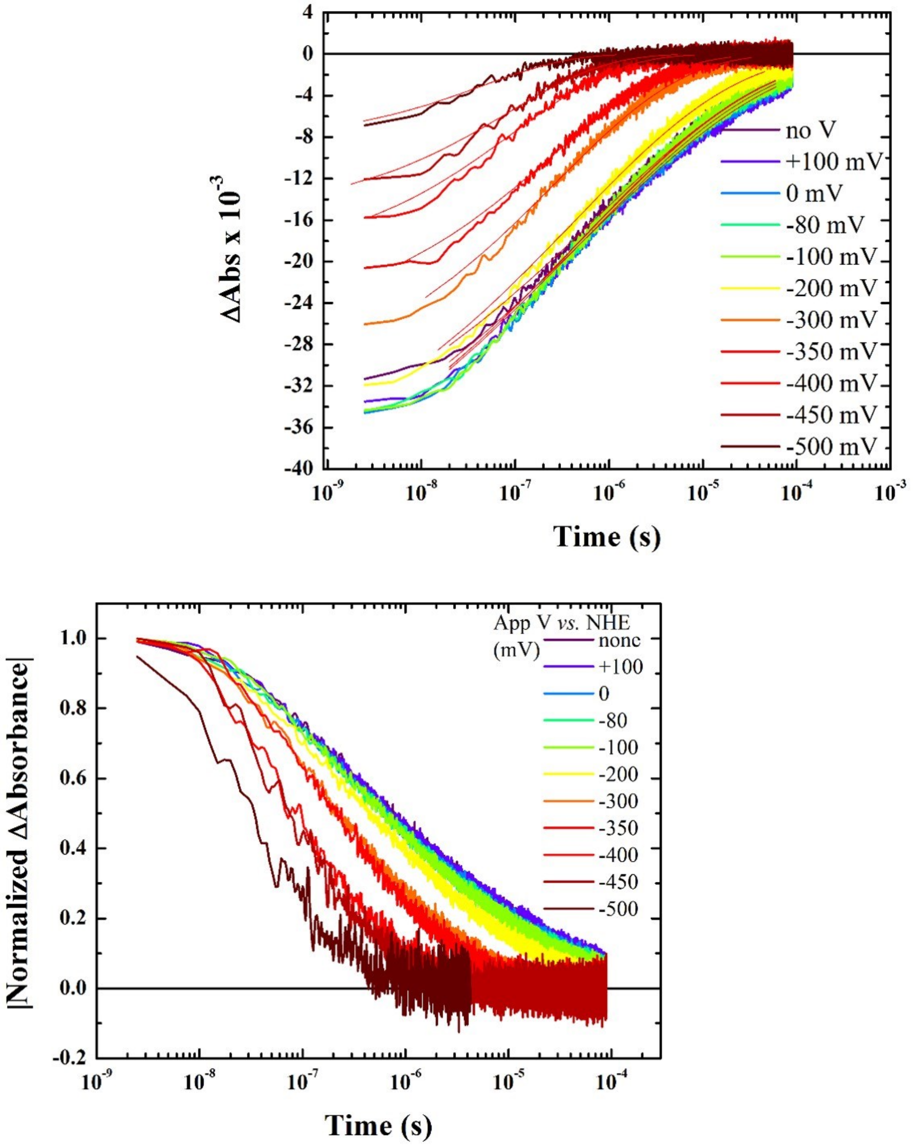

Figure 3.24 Top) The change in absorbance of FTO|TiO_2|Model in 300 mM $LiClO_4$ CH_3CN at 402 nm with the indicated applied potentials. Bottom) The same data normalized at t = 0.

The kinetic data for each sensitizer is shown in Figure 3.25. Each plot contains the kinetic data for every sensitizer at a given applied potential. The kinetic data are normalized in Figure 3.26 to show the relative rates more clearly.

Figure 3.27 shows the logarithm of the observed rate constants as a function of the applied potential for each sensitizer. There is a linear relationship for the rate constants measured at potentials ≤ -200 mV, and the sensitizers have different slopes, shown in the image legend. The rate constants from every sensitizer at every applied potential are plotted as a function of the Ru(III/II) reduction potential of the sensitizer in Figure 3.27. Each applied potential has been assigned a color, and each sensitizer has been assigned a symbol. The grey, dotted lines on the plot are meant to emphasize relevant behavior. This will be discussed further below.

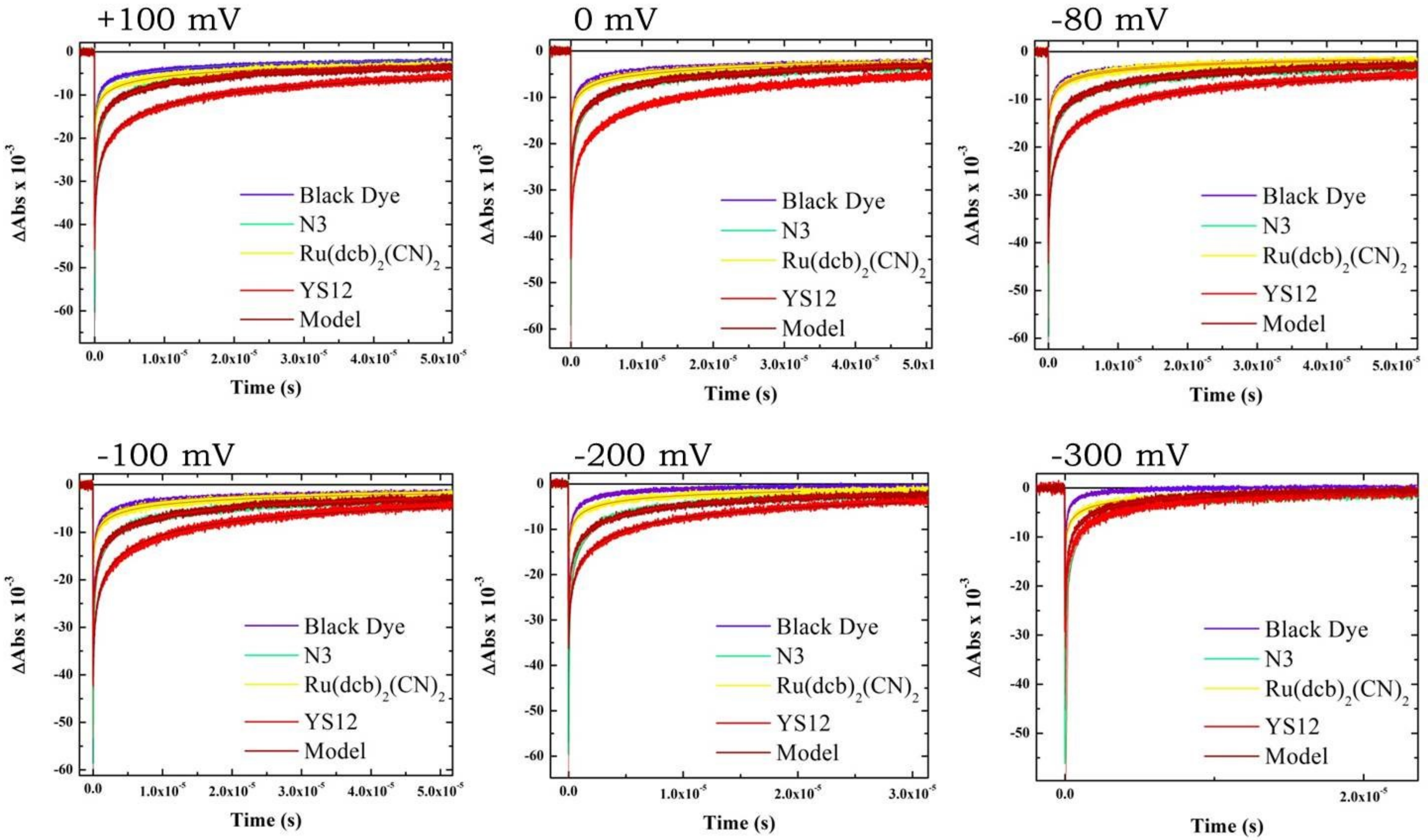
+100 mV
0 mV
-80 mV
-100 mV
-200 mV
-300 mV
ΔAbs x 10^{-3}
Time (s)
Black Dye
N3
Ru(dcb)$_2$(CN)$_2$
YS12
Model
0
-10
-20
-30
-40
-50
-60
0.0
1.0x10^{-5}
2.0x10^{-5}
3.0x10^{-5}
4.0x10^{-5}
5.0x10^{-5}

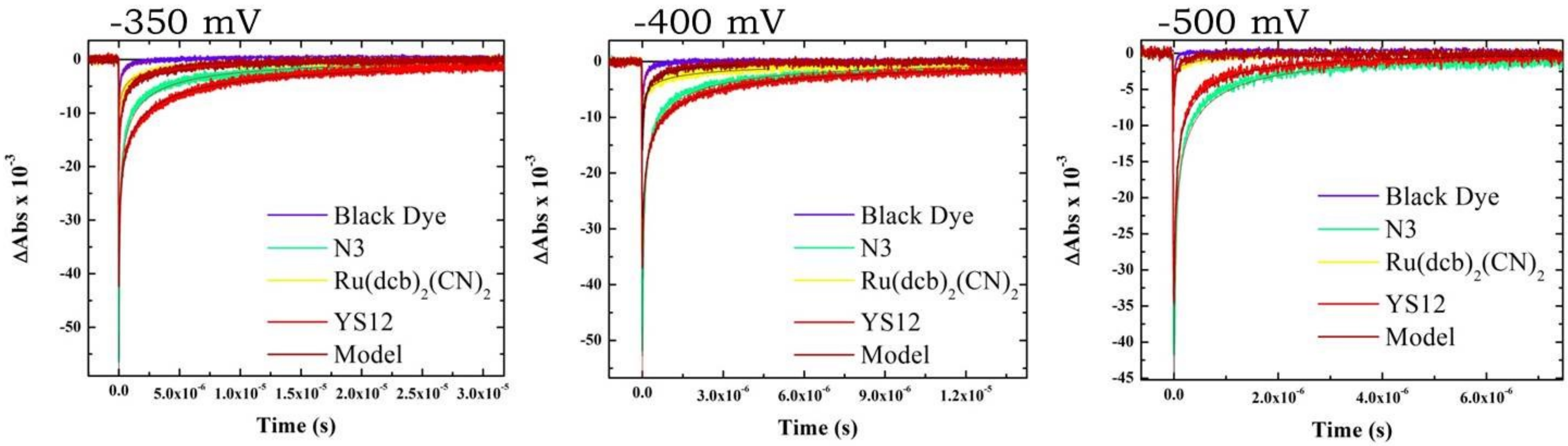

Figure 3.25 The absorbance change after pulsed laser excitation of all the sensitizer anchored to TiO_2 at the indicated applied potentials with fits to KWW overlaid in red.

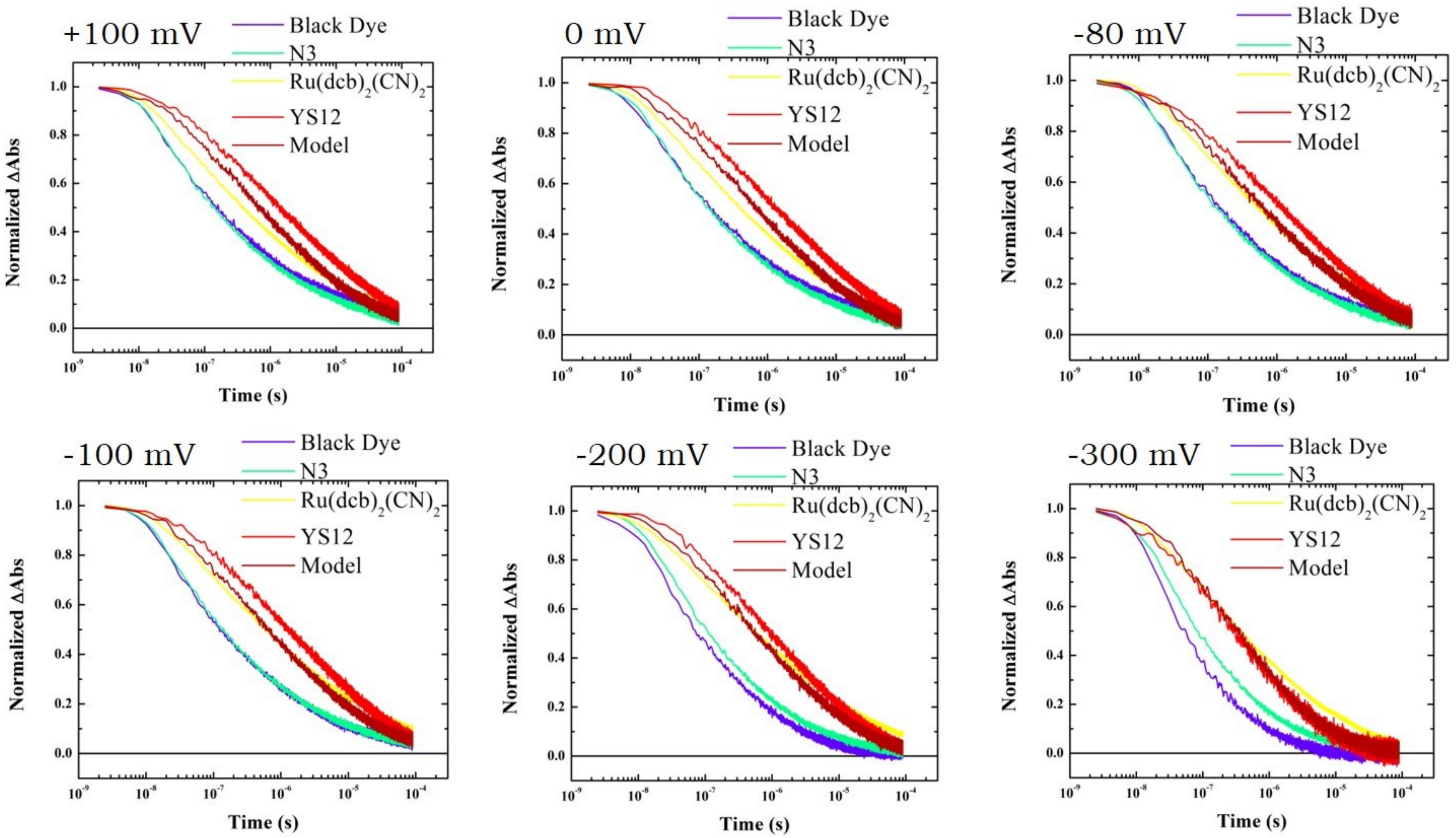
+100 mV
0 mV
-80 mV
-100 mV
-200 mV
-300 mV
Black Dye
N3
Ru(dcb)$_2$(CN)$_2$
YS12
Model
Normalized ΔAbs
Time (s)
0.0
0.2
0.4
0.6
0.8
1.0
10^{-9}
10^{-8}
10^{-7}
10^{-6}
10^{-5}
10^{-4}

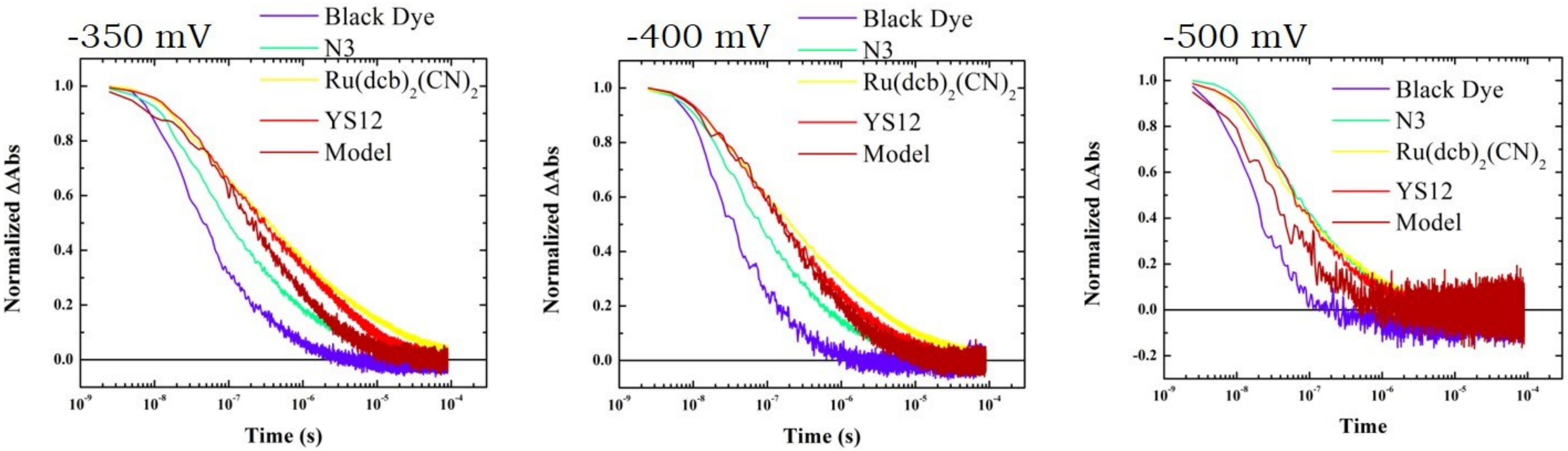

Figure 3.26 The same data as shown in Figure 3.25 normalized at time zero.

Table 3.2 The observed rate constants for recombination for each sensitizer at each applied potential, in units of s-1. The beta values used for each potential group are also included. In the table, Ru(dcb)2(CN)2 is abbreviated as CN2.

	App V	+0.1	0	-0.08	-0.1	-0.2	-0.3	-0.35	-0.4	-0.5
	β	0.203	0.204	0.207	0.213	0.240	0.266	0.271	0.277	0.31
Sensitizer	BD	31300 (±730)	26200 (±660)	4.4E4 (±1E3)	6.6E4 (±1.6E3)	6.7E5 (±1.84E4)	2.75E6 (±1.07E5)	4.6E6 (±1.9E5)	6.3E6 (±4.1E5)	1.75E7 (±5.1E6)
	N3	60700 (±1.4E3)	5.3E4 (±1.3E3)	60700 (±1.4E3)	6.3E4 (±1.5E3)	2.33E5 (±6E3)	6.48E5 (±2E4)	5.69E5 (±1.5E4)	1.09E6 (±3.0E4)	1.91E6 (±8.4E4)
	CN2	1.28E4 (±300)	1.67E4 (±400)	3.37E4 (±800)	3.03E4 (±700)	1.05E5 (±2.7E3)	2.37E5 (±8.5E3)	4.1E5 (±1.4E4)	3.4E5 (±1.5E4)	1.3E6 (±4.3E4)
	YS12	1.84E4 (±400)	2.19E4 (±500)	2.44E4 (±530)	3.1E4 (±700)	6.1E4 (±1.4E3)	3.42E5 (±1E4)	2.54E5 (±6.1E3)	5.4E5 (±1.5E4)	2.9E6 (±6.2E5)
	Model	2.44E4 (±550)	3.32E4 (±800)	4.03E4 (±900)	4.2E4 (±1E3)	1.05E5 (±2.5E3)	5.0E5 (±1.6E4)	7.6E5 (±2.2E4)	2.59E6 (±9.6E4)	8.4E6 (±8E5)

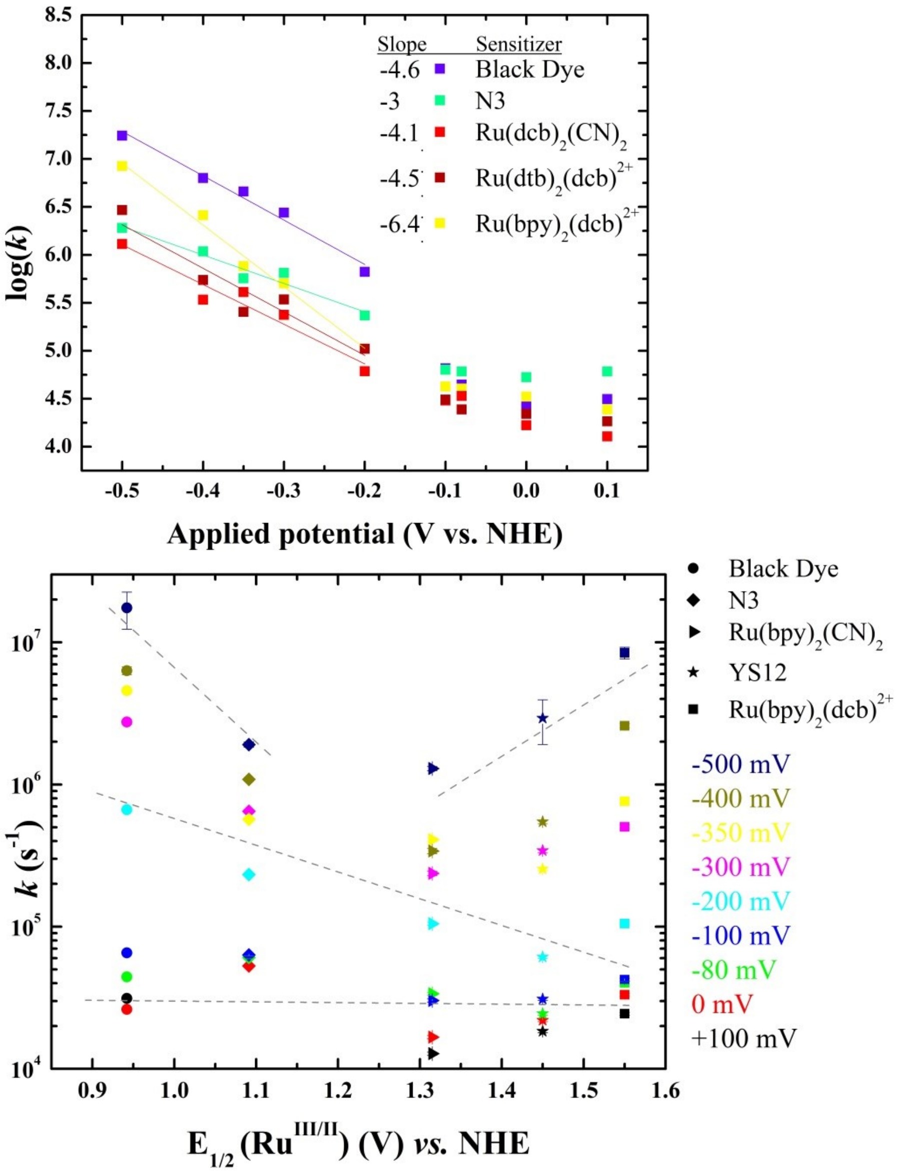

Figure 3.27 Top) The log of the observed rate constant for recombination to the indicated sensitizers anchored to TiO_2 plotted as a function of applied potential. Each color represents the indicated sensitizer. Bottom) The same rate constants plotted as a function of the Ru(III/II) reduction potential of the sensitizer.

3.4 Discussion

For each of the sensitizers, the charge separated ($TiO_2(e^-)|S^+$) and excited state difference spectra were measured using nanosecond transient absorption. Based on these spectra, wavelengths for monitoring $TiO_2(e^-)|S^+ \rightarrow TiO_2|S$ recombination were chosen. The observed rate constants for charge recombination at a series of increasingly negative applied potentials were abstracted from the transient absorption kinetic data using the Kohlrausch Williams-Watts function, Equation 3.2.

In the kinetic fitting, the data were grouped according to the applied potential and the β fitting parameter was shared in each group. The meaningfulness of any model must always be questioned, especially one so broadly used as the KWW function. It is best if the basis for the conclusion suggested by modeling can be seen in the raw data itself. It is highly encouraging that, in this chapter, the normalized raw data (Figure 3.26) suggest the same ordering of the rapidity of the recombination reaction as do the extracted rate constants for recombination to every sensitizer at every applied potential.

At the least negative applied potentials, the rate constants for recombination are essentially invariant with the Ru(III/II) reduction potential. Beginning at -200 mV, there appears to be an inverse relationship between Ru(III/II) reduction potential and the observed rate constant. This is what would be expected in the Marcus inverted region under conditions where the formation of the encounter complex is fast enough that the electron transfer has an effect on the rate of charge recombination. Arguably, this relationship is still observable in the rate constants for recombination at -300 and -350 mV applied potential. The relationship is more complex at more negative applied potentials, such as -400 and -500 mV. The effect of the driving force seems to be at least partially eclipsed by another effect at -400 and -500 mV applied potential. It should be noted that there is approximately ±10 mV uncertainty in the applied potential of the potentiostat used, and this potential range represents a much larger range in electron concentration at -400 and -500 mV than at -200 mV because of the exponential nature of the density of acceptor states in TiO_2. This could contribute to the complicated behavior observed at -400 and -500 mV.

It is also possible that this seemingly anomalous behavior is related to the increasing electric field emanating from the TiO_2 particles as the applied potential becomes more negative. An applied potential can cause greater ordering of the solvent at electrode surfaces.[29] This greater ordering could give rise to a shift in the reorganization energy that defines the vertex of the log(k) vs. driving force Marcus parabola. Usually with Ru(III/II) reduction, the outer-sphere reorganization is the largest contributor to the reorganization energy; thus, it is reasonable to expect that a change in the rigidity of the solvent ordering would significantly affect the overall reorganization energy. If the reorganization energy were to increase enough to place recombination to the oxidized sensitizers in the normal region, the expected trend in recombination rate constants would be reversed. The change in behavior observed at -400 and -500 mV could be the beginning of this transition.

There are several other factors that could be superseding the change in driving force for the recombination reaction. For example, there has been substantial work indicating the presence of some distance dependence in the rate of interfacial recombination in $TiO_2|S$ systems.[2,7,30–33] In the sensitizer series used in this chapter, the hole is likely not localized at exactly the same distance from the TiO_2 surface for all of the sensitizers, because they do not constitute a structurally homologous series, although the sensitizers have structural similarities. For example, the electron donation from isothiocyanate ligands to the metal *d* orbitals places part of the LUMO on the SCN^-, rather than being localized on the Ru(III) center.[22,34] Whether this variation in hole distance would have a substantial effect is unclear, especially since the variation in distance is confined to the diameter of a Ru-polypyridyl compound. However, it has been shown that the distance dependence of recombination is more marked in $TiO_2|S$ systems when the applied potential is more negative,[30] which may at least partially account for the change in behavior seen at -400 and -500 mV. The slopes of the log(*k*) vs. applied potential plot (Figure 3.27 Top) could reflect this increase in sensitivity to distance with more negative applied potential. Additionally, the molecular dipole moment of S has been shown to have an electronic effect at interfaces such as the TiO_2|S interface.[30,35–39] The sensitizers in our series do not have the similar dipole moments, in either the Ru(II) or the Ru(III) states. It is possible that the analysis of driving force dependence could be compounded by these effects.

The slopes of the linear fits of the logarithm of the observed rate constants may be the result of a fundamental difference between the TiO_2|S systems. The interaction of dipoles with the electric field could be a factor in the rate of increase in log(*k*). For example, the largest slope shown in this chapter (-6.4) is that of the compound with a small expected dipole, $Ru(bpy)_2(dcb)$. Additionally, Chapter 4 reports on a compound with a very small dipole, a cobalt corrin, which exhibits a slope of -7.4. A symmetric cobalt porphyrin, with essentially no dipole, has previously exhibited a slope of -8.3. Notably, both of these cobaltous examples were measured in tetrabutylammonium perchlorate electrolyte, rather than in the presence of lithium perchlorate, which could affect the relationship by altering the density of acceptor states in the TiO_2. In another example, two organic dyes with small calculated dipole moments[40] have slopes of -7.7 and -9.8.[41] On the other hand, the sensitizers with less negative slopes (especially the Black Dye, N3, and $Ru(dcb)_2(CN)_2$) all have strong σ donating ligands with π accepting capability trans to the anchoring ligands.

3.5 Conclusions & Future Direction

The data presented here suggest that at negative applied potentials, there is a contribution from the electron transfer event to the rate of charge recombination. This is most clear at -200 mV. Furthermore, in the absence of a sufficiently negative applied potential, the driving force dependence is not observed. This is the first time that this change in control over the rate of charge recombination has been shown by changing the concentration of electrons in TiO_2. Indeed, evidence of sensitivity of the rate of recombination to molecular factors has been limited and noteworthy when found. Reports of the dependence and lack of dependence of the rate of recombination on the sensitizer properties are cited here.[1,2,8,30,35,36,41]

Improved understanding of the behavior at very negative applied potentials, such as -400 and -500 mV, would greatly enhance the strength of this evidence for driving force dependence in interfacial charge recombination. This could be pursued by modeling the Ru(II) and

Ru(III) states of the sensitizers in the present series to compare their dipoles and the expected distance between the TiO_2 surface and the hole in the formally Ru(III) oxidation state to the observed kinetics.

3.6 Acknowledgements

The author is grateful to Tyler Motley for taking the profilometry measurements, Brian N. DiMarco for donating several samples of nanocrystalline zirconia thin films on glass, Dr. Ke Hu for many productive conversations about data analysis, Timothy J. Barr for editing and productive conversations, and the previous members of the Meyer lab who synthesized the sensitizers.

3.7 References

(1) Kuciauskas, D.; Freund, M. S.; Gray, H. B.; Winkler, J. R.; Lewis, N. S. Electron Transfer Dynamics in Nanocrystalline Titanium Dioxide Solar Cells Sensitized with Ruthenium or Osmium Polypyridyl Complexes. *J. Phys. Chem. B* **2001**, *105* (2), 392–403.

(2) Clifford, J. N.; Palomares, E.; Nazeeruddin, M. K.; Grätzel, M.; Nelson, J.; Li, X.; Long, N. J.; Durrant, J. R. Molecular Control of Recombination Dynamics in Dye-Sensitized Nanocrystalline TiO_2 Films: Free Energy vs Distance Dependence. *J. Am. Chem. Soc.* **2004**, *126* (16), 5225–5233.

(3) Clifford, J. N.; Yahioglu, G.; Milgrom, L. R.; Durrant, J. R. Molecular Control of Recombination Dynamics in Dye Sensitised Nanocrystalline TiO_2 Films. *Chem. Commun.* **2002**, No. 12, 1260–1261.

(4) Haque, S. A.; Tachibana, Y.; Klug, D. R.; Durrant, J. R. Charge Recombination Kinetics in Dye-Sensitized Nanocrystalline Titanium

Dioxide Films under Externally Applied Bias. *J. Phys. Chem. B* **1998**, *102* (10), 1745–1749.

(5) Haque, S. A.; Tachibana, Y.; Willis, R. L.; Moser, J. E.; Grätzel, M.; Klug, D. R.; Durrant, J. R. Parameters Influencing Charge Recombination Kinetics in Dye-Sensitized Nanocrystalline Titanium Dioxide Films. *J. Phys. Chem. B* **2000**, *104* (3), 538–547.

(6) Nelson, J.; Haque, S. A.; Klug, D. R.; Durrant, J. R. Trap-Limited Recombination in Dye-Sensitized Nanocrystalline Metal Oxide Electrodes. *Phys. Rev. B* **2001**, *63* (20), 205321.

(7) Haque, S. A.; Handa, S.; Peter, K.; Palomares, E.; Thelakkat, M.; Durrant, J. R. Supermolecular Control of Charge Transfer in Dye-Sensitized Nanocrystalline TiO_2 Films: Towards a Quantitative Structure–Function Relationship. *Angew. Chem. Int. Ed.* **2005**, *44* (35), 5740–5744.

(8) Hasselmann, G. M.; Meyer, G. J. Diffusion-Limited Interfacial Electron Transfer with Large Apparent Driving Forces. *J. Phys. Chem. B* **1999**, *103* (36), 7671–7675.

(9) Brigham, E. C.; Meyer, G. J. Ostwald Isolation to Determine the Reaction Order for TiO_2 (e–)|S+→ TiO_2|S Charge Recombination at Sensitized TiO_2 Interfaces. *J. Phys. Chem. C* **2014**, *118* (15), 7886–7893.

(10) Marcus, R. A. Electron Transfer Reactions in Chemistry. Theory and Experiment. *Rev. Mod. Phys.* **1993**, *65* (3), 599–610.

(11) Nazeeruddin, M. K.; Kay, A.; Rodicio, I.; Humphry-Baker, R.; Mueller, E.; Liska, P.; Vlachopoulos, N.; Graetzel, M. Conversion of Light to Electricity by Cis-X2bis(2,2'-Bipyridyl-4,4'-dicarboxylate)ruthenium(II) Charge-Transfer Sensitizers (X = Cl-, Br-, I-, CN-, and SCN-) on Nanocrystalline Titanium Dioxide Electrodes. *J. Am. Chem. Soc.* **1993**, *115* (14), 6382–6390.

(12) Péchy, P.; Renouard, T.; Zakeeruddin, S. M.; Humphry-Baker, R.; Comte, P.; Liska, P.; Cevey, L.; Costa, E.; Shklover, V.; Spiccia, L.; Deacon, G. B.; Bignozzi, C. A.; Grätzel, M. Engineering of Efficient Panchromatic Sensitizers for Nanocrystalline TiO_2-Based Solar Cells. *J. Am. Chem. Soc.* **2001**, *123* (8), 1613–1624.

(13) Kelly, C. A.; Farzad, F.; Thompson, D. W.; Stipkala, J. M.; Meyer, G. J. Cation-Controlled Interfacial Charge Injection in Sensitized Nanocrystalline TiO_2. *Langmuir* **1999**, *15* (20), 7047–7054.

(14) Pavlishchuk, V. V.; Addison, A. W. Conversion Constants for Redox Potentials Measured versus Different Reference Electrodes in Acetonitrile Solutions at 25°C. *Inorganica Chim. Acta* **2000**, *298* (1), 97–102.

(15) Morris, A. J.; Meyer, G. J. TiO_2 Surface Functionalization to Control the Density of States. *J. Phys. Chem. C* **2008**, *112* (46), 18224–18231.

(16) Argazzi, R.; Bignozzi, C. A.; Heimer, T. A.; Castellano, F. N.; Meyer, G. J. Enhanced Spectral Sensitivity from Ruthenium(II) Polypyridyl Based Photovoltaic Devices. *Inorg. Chem.* **1994**, *33* (25), 5741–5749.
(17) Kohlrausch, R. Theorie Des Elektrischen Rückstandes in Der Leidener Flasche. *Ann. Phys.* **1854**, *167* (2), 179–214.
(18) Nelson, J. Continuous-Time Random-Walk Model of Electron Transport in Nanocrystalline TiO_2 Electrodes. *Phys. Rev. B* **1999**, *59* (23), 15374–15380.
(19) Williams, G.; Watts, D. C. Non-Symmetrical Dielectric Relaxation Behaviour Arising from a Simple Empirical Decay Function. *Trans. Faraday Soc.* **1970**, *66* (0), 80–85.
(20) Lindsey, C. P.; Patterson, G. D. Detailed Comparison of the Williams–Watts and Cole–Davidson Functions. *J. Chem. Phys.* **1980**, *73* (7), 3348.
(21) Li, X.; Nazeeruddin, M. K.; Thelakkat, M.; Barnes, P. R. F.; Vilar, R.; Durrant, J. R. Spectroelectrochemical Studies of Hole Percolation on Functionalised Nanocrystalline TiO_2 Films: A Comparison of Two Different Ruthenium Complexes. *Phys. Chem. Chem. Phys.* **2011**, *13* (4), 1575–1584.
(22) Kämper, S.; Paretzki, A.; Fiedler, J.; Záliš, S.; Kaim, W. Solar Cell Sensitizer Models $[Ru(bpy\text{-}R)_2(NCS)_2]$ Probed by Spectroelectrochemistry. *Inorg. Chem.* **2012**, *51* (4), 2097–2104.
(23) Kuang, D.; Ito, S.; Wenger, B.; Klein, C.; Moser, J.-E.; Humphry-Baker, R.; Zakeeruddin, S. M.; Grätzel, M. High Molar Extinction Coefficient Heteroleptic Ruthenium Complexes for Thin Film Dye-Sensitized Solar Cells. *J. Am. Chem. Soc.* **2006**, *128* (12), 4146–4154.
(24) Fattori, A.; Peter, L. M.; McCall, K. L.; Robertson, N.; Marken, F. Adsorption and Redox Chemistry of Cis-RuLL’$(SCN)_2$ with L=4,4′-Dicarboxylic Acid-2,2′-Bipyridine and L’=4,4′-Dinonyl-2,2′-Bipyridine (Z907) at FTO and TiO_2 Electrode Surfaces. *J. Solid State Electrochem.* **2010**, *14* (10), 1929–1936.
(25) O’Donnell, R. M.; Sampaio, R. N.; Barr, T. J.; Meyer, G. J. Electric Fields and Charge Screening in Dye Sensitized Mesoporous Nanocrystalline TiO_2 Thin Films. *J. Phys. Chem. C* **2014**, *118* (30), 16976–16986.
(26) Ardo, S.; Sun, Y.; Staniszewski, A.; Castellano, F. N.; Meyer, G. J. Stark Effects after Excited-State Interfacial Electron Transfer at Sensitized TiO_2 Nanocrystallites. *J. Am. Chem. Soc.* **2010**, *132* (19), 6696–6709.
(27) Barr, T. J. Unpublished Results.
(28) Cappel, U. B.; Feldt, S. M.; Schöneboom, J.; Hagfeldt, A.; Boschloo, G. The Influence of Local Electric Fields on Photoinduced

Absorption in Dye-Sensitized Solar Cells. *J. Am. Chem. Soc.* **2010**, *132* (26), 9096–9101.

(29) Bockris, J. O.; Devanathan, M. a. V.; Muller, K. On the Structure of Charged Interfaces. *Proc. R. Soc. Lond. Math. Phys. Eng. Sci.* **1963**, *274* (1356), 55–79.

(30) Johansson, P. G.; Kopecky, A.; Galoppini, E.; Meyer, G. J. Distance Dependent Electron Transfer at TiO_2 Interfaces Sensitized with Phenylene Ethynylene Bridged RuII–Isothiocyanate Compounds. *J. Am. Chem. Soc.* **2013**, *135* (22), 8331–8341.

(31) Abrahamsson, M.; Johansson, P. G.; Ardo, S.; Kopecky, A.; Galoppini, E.; Meyer, G. J. Decreased Interfacial Charge Recombination Rate Constants with N3-Type Sensitizers. *J. Phys. Chem. Lett.* **2010**, *1* (11), 1725–1728.

(32) Johansson, P. G.; Zhang, Y.; Abrahamsson, M.; Meyer, G. J.; Galoppini, E. Slow Excited State Injection and Charge Recombination at Star-Shaped Ruthenium Polypyridyl compounds—TiO_2 Interfaces. *Chem. Commun.* **2011**, *47* (22), 6410.

(33) Johansson, P. G.; Zhang, Y.; Meyer, G. J.; Galoppini, E. Homoleptic “Star” Ru(II) Polypyridyl Complexes: Shielded Chromophores to Study Charge-Transfer at the Sensitizer-TiO_2 Interface. *Inorg. Chem.* **2013**, *52* (14), 7947–7957.

(34) Lockard, J. V.; Rachford, A. A.; Smolentsev, G.; Stickrath, A. B.; Wang, X.; Zhang, X.; Atenkoffer, K.; Jennings, G.; Soldatov, A.; Rheingold, A. L.; Castellano, F. N.; Chen, L. X. Triplet Excited State Distortions in a Pyrazolate Bridged Platinum Dimer Measured by X-Ray Transient Absorption Spectroscopy. *J. Phys. Chem. A* **2010**, *114* (48), 12780–12787.

(35) Hu, K.; Robson, K. C. D.; Johansson, P. G.; Berlinguette, C. P.; Meyer, G. J. Intramolecular Hole Transfer at Sensitized TiO_2 Interfaces. *J. Am. Chem. Soc.* **2012**, *134* (20), 8352–8355.

(36) Hu, K.; Robson, K. C. D.; Beauvilliers, E. E.; Schott, E.; Zarate, X.; Arratia-Perez, R.; Berlinguette, C. P.; Meyer, G. J. Intramolecular and Lateral Intermolecular Hole Transfer at the Sensitized TiO_2 Interface. *J. Am. Chem. Soc.* **2014**, *136* (3), 1034–1046.

(37) Howie, W. H.; Claeyssens, F.; Miura, H.; Peter, L. M. Characterization of Solid-State Dye-Sensitized Solar Cells Utilizing High Absorption Coefficient Metal-Free Organic Dyes. *J. Am. Chem. Soc.* **2008**, *130* (4), 1367–1375.

(38) Ronca, E.; Pastore, M.; Belpassi, L.; Tarantelli, F.; Angelis, F. D. Influence of the Dye Molecular Structure on the TiO_2 Conduction Band in Dye-Sensitized Solar Cells: Disentangling Charge Transfer and Electrostatic Effects. *Energy Environ. Sci.* **2012**, *6* (1), 183–193.

(39) Chen, P.; Yum, J. H.; Angelis, F. D.; Mosconi, E.; Fantacci, S.; Moon, S.-J.; Baker, R. H.; Ko, J.; Nazeeruddin, M. K.; Grätzel, M.

High Open-Circuit Voltage Solid-State Dye-Sensitized Solar Cells with Organic Dye. *Nano Lett.* **2009**, *9* (6), 2487–2492.
(40) Swords, W. B. Unpublished Data. **2015**.
(41) Robson, K. C. D.; Hu, K.; Meyer, G. J.; Berlinguette, C. P. Atomic Level Resolution of Dye Regeneration in the Dye-Sensitized Solar Cell. *J. Am. Chem. Soc.* **2013**, *135* (5), 1961–1971.

Chapter 4. Electron injection into TiO_2 after light-excitation of Cob(I)alamin

This work was done in collaboration with Darren Achey, who is now Assistant Professor of Chemistry at Kutztown University, Kutztown, PA, USA.

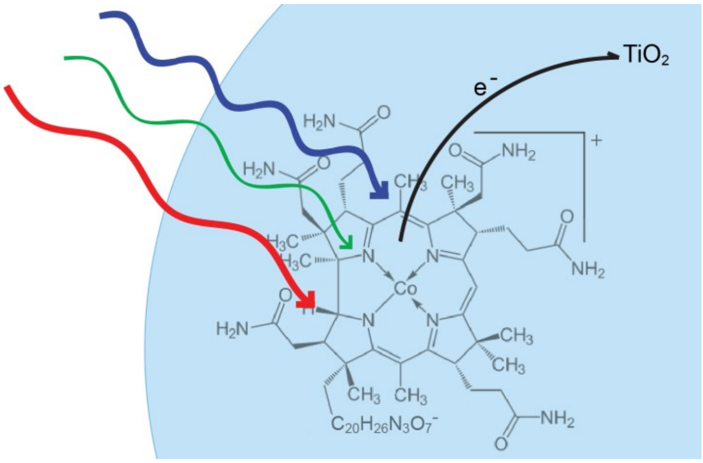

Scheme 4.1 Illustration of electron transfer after light excitation of cob(I)alamin anchored to TiO_2.

4.1 Introduction

The ubiquitous cofactor cobalamin has been of great interest since the discovery of its unique cobalt-carbon bond by Dorothy Crowfoot Hodgkin, for which she won the 1964 Nobel Prize. At the time, the cobalamin derivatives were the largest biomolecules that had ever been characterized by X-ray crystallography. Cobalamins continue to be the subject of extensive research due to their unusual ability to exist in highly reduced states and form organometallic intermediates in aerobic biological systems.[1–8] Cobalamin and cobamide dependent enzymes perform a diverse array of difficult reactions, which proceed *via* both radical and non-radical pathways, including methyl transfers, rearrangements, and dehydrations.[9,10] However, the first observation of outer sphere electron transfer from the excited state of cob(I)alamin derivatives after visible light excitation is described herein. The cobalamin derivatives used for this research are shown in Figure 4.1.

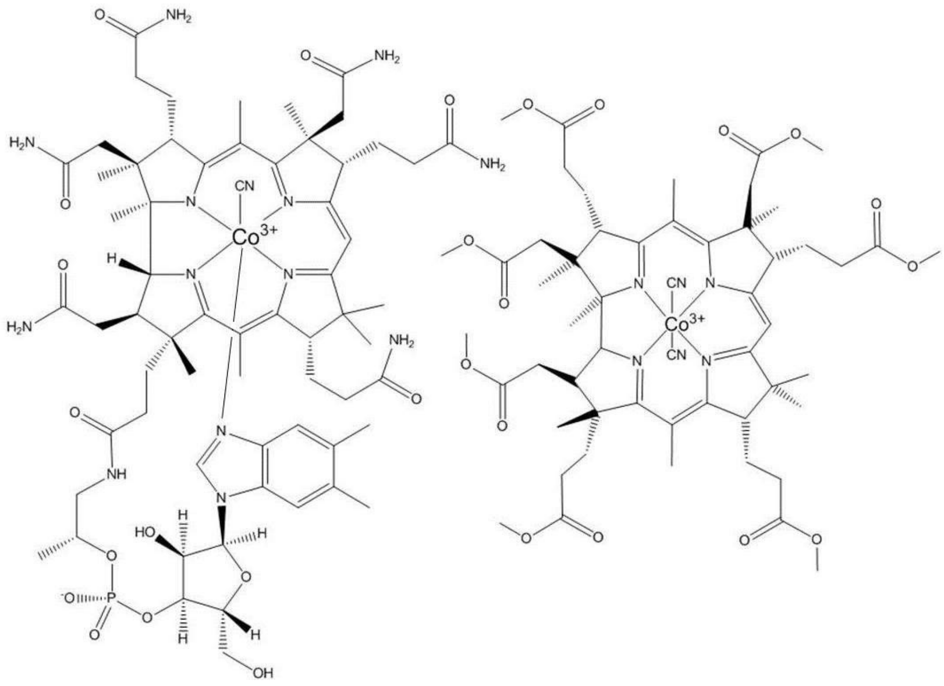

Figure 4.1 Right) The structure of cyanocob(III)alamin, also known as vitamin B_{12}. Left) The structure of dicyanocobyrinic acid heptamethyl ester, referred to herein as cobyrinate.

Recently, the Brunold and Kozlowski groups have reported on computational descriptions of the electronic structure of various cobalamin derivatives. The frontier orbitals of the electronic structure for cob(I)alamin computed by Liptak *et al.* is shown in Figure 4.2. The electronic structure and the percentage each transition contributes to the absorbance at various excitation wavelengths provided insight into the nature of the excited state involved in electron transfer.

Several other Co(I) macrocycles have recently been reported to undergo photo-induced charge separation at TiO_2 interfaces. Some examples are summarized in the following paragraphs.

4.1.1 Co(I) macrocycles: injection into TiO_2 and interfacial charge recombination

Figure 4.3A shows the absorbance of $Co(deegH)_2(py)_2$ (**1** in Scheme 4.2, where $deegH_2$ is diethylesterglyoxime and py is pyridine) anchored to the semiconductor surface before and after electrochemical reduction.[12] In this example, the $TiO_2|Co(II)$ and $TiO_2|Co(III)$ states do not have appreciable light absorbance in the visible region, while the reduction ($E_{1/2} \approx -350$ mV *vs.* NHE) to $TiO_2|Co(I)$ is accompanied by the emergence of an absorption centered at 680 nm with an extinction coefficient of 8,000 $M^{-1}cm^{-1}$ (Figure 4.3A).[12] This absorbance band has been assigned as a metal-to-ligand charge transfer (MLCT) in similar cobaloximes [13–15] as well as Co(I) polypyridyl compounds.[16–18] It is notable that the absorption band harvests light throughout the visible region extending to the near infrared region, so that the sensitized thin film appears blue in color.

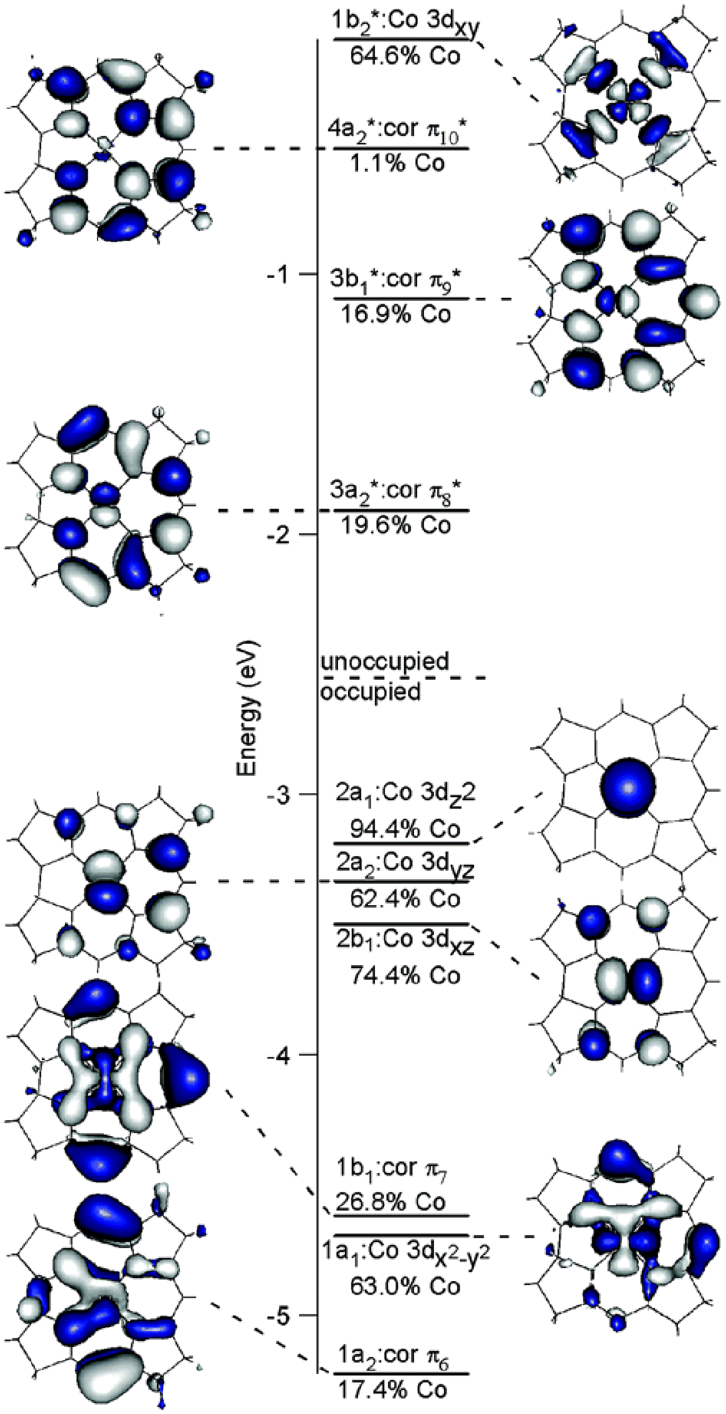

Figure 4.2 Electronic structure of cob(I)alamin according to Liptak et al. Reprinted with permission from Liptak, M. D.; Brunold, T. C. Spectroscopic and Computational Studies of Co1+Cobalamin: Spectral and Electronic Properties of the "Superreduced" B12 Cofactor. *J. Am. Chem. Soc.* 2006, *128* (28), 9144–9156. Copyright 2006 American Chemical Society.[11]

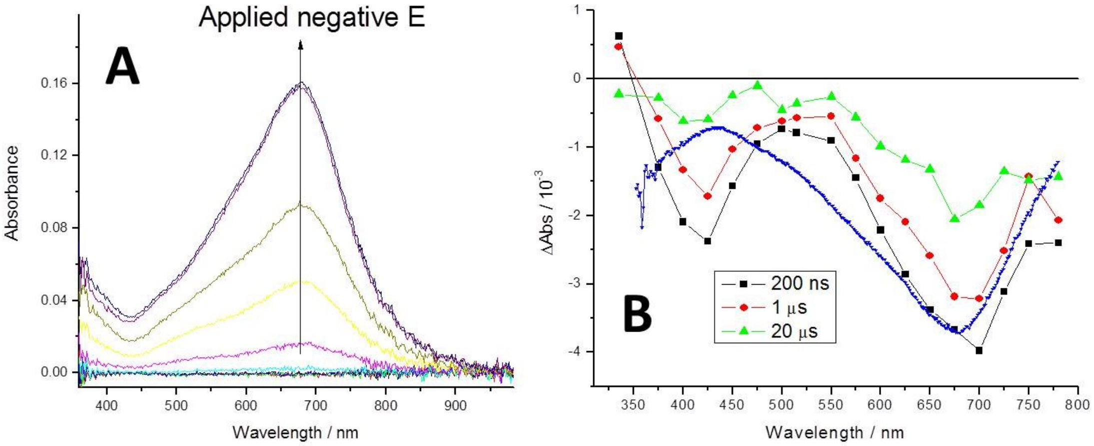

Figure 4.3 A) The absorbance of $TiO_2|Co(deegH)_2(py)_2$ with applied potential from +130 to -520 mV vs. NHE. The arrow indicates the direction of growth with increasingly negative applied potential. B) The change in absorbance after pulsed 532 nm laser excitation at the indicated delay times. The blue spectrum is the scaled difference in absorbance of Co(II) with respect to Co(I). Modified with permission from Ref.[12]

Figure 4.3B shows the absorption changes measured after pulsed 532 nm light excitation of $TiO_2|Co(I)$ in an acetonitrile electrolyte. A bleach of the MLCT absorption band was observed, which lasted for ~100 microseconds. The blue overlay in Figure 4.3B is a simulation of the spectral changes expected for excited state electron transfer to TiO_2 that would yield $TiO_2(e^-)|Co(II)$, Equation 4.1.

$$TiO_2|Co(I) + h\nu \rightarrow TiO_2(e^-)|Co(II) \tag{4.1}$$

The simulated spectrum was not exact, and the deviations between simulation and experiment may result from surface electric fields that are known to affect the absorption spectra of molecules anchored to the TiO_2 surface.[19,20] Notably, absorption measurements made before and after pulsed laser excitation showed no evidence for net photochemistry of any type. Control experiments with pulsed laser excitation of $TiO_2|Co(III)(deegH)_2$ or $TiO_2|Co(II)(deegH)_2$ under otherwise identical conditions revealed no evidence for interfacial electron transfer. Given that the major difference in the electronic absorbance between Co(III) and Co(II) compared to Co(I) was the growth of a MLCT absorbance, and the absence of absorbance change after excitation of Co(III) and Co(II), it follows that the MLCT excited state of Co(I) was likely the species responsible for electron transfer to TiO_2. The appearance of the $TiO_2(e^-)|Co(II)(deegH)_2$ product state could not be time resolved, indicating that electron transfer occurred within the instrument response time of 10 ns, $k_{et} > 10^8$ s^{-1}. Several more examples presented below demonstrate the generality of this finding, and indicate that MLCT excited state electron transfer is a general phenomenon for Co(I) macrocycles.

The other cobalt compounds reported to transfer electrons into TiO_2 after light absorption are shown in Scheme 4.2: (**2**) cobalt(III) protoporphyrin IX chloride (CoPPIX),[21] (**3**) cobalt phthalocyanine tetrasulfonic acid (CoPc),[21] (**4a**) cobalt(III) (tetracarboxyphenyl)porphyrin chloride (CoP),[12] and (**4b**) cobalt(III) meso-5,10,15,20-tetrakis(4-sulfonatophenyl)porphyrin chloride (CoTSP).[21]

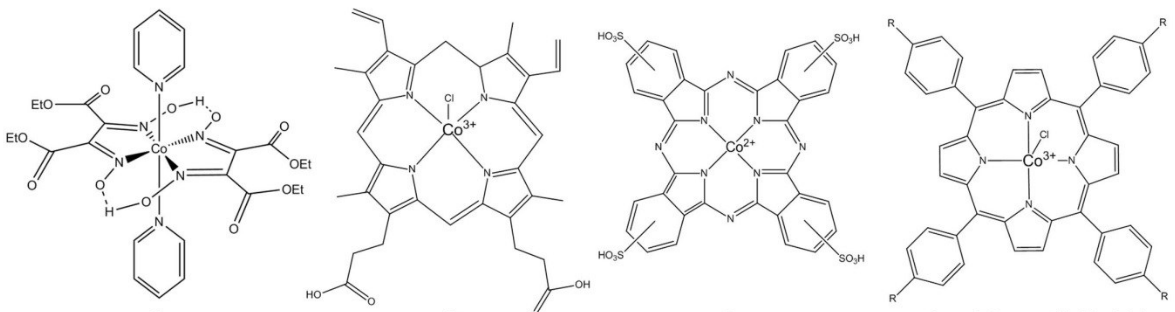

1 **2** **3** **4a R = CO_2H**
4b R = SO_3H

Scheme 4.2 The molecular structures of the cobalt complexes shown to inject electrons into TiO_2 after light absorption by their Co(I) state: 1) Co(II)(deegH)$_2$(py)$_2$ (where deegH$_2$ = diethylesterglyoxime and py = pyridine), 2) cobalt(III) protoporphyrin IX chloride (CoPPIX), 3) cobalt phthalocyanine tetrasulfonic acid (CoPc), 4a) cobalt(III) (tetracarboxyphenyl)porphyrin chloride (CoP), and 4b) cobalt(III) meso-5, 10,15,20-tetrakis(4-sulfonatophenyl)porphyrin chloride (CoTSP).

For all these compounds, evidence for excited state electron transfer was only observed when the cobalt center was in the formal oxidation state of Co(I) prior to light absorption. In this regard, all of the compounds behaved similarly. Although the nature of the anchoring groups varied between the cobalt complexes, there was not a significant effect on electron injection yield. This suggests that other factors, such as the nature of the excited state, controlled injection to a greater extent. The cob(I)aloxime had the most easily identifiable MLCT excited state of the Co(I) compounds known to undergo excited state electron transfer. In addition to an MLCT absorbance analogous to that of **1**, the macrocyclic compounds **2-4** also displayed ligand centered π→π* excited states that introduced some uncertainty into which excited state(s) were responsible for the electron transfer reactivity. To better understand the relevant excited state, three excitation wavelengths in the blue, green and red regions (436, 532 and 683 nm) were utilized and the relative injection yields (Φ_{rel}) were quantified (Table 4.1).[21] The excited state electron transfer reaction could not be time resolved, $k_{et} > 10^8$ s^{-1}, for any of the excitation wavelengths. However, it was found that the injection yields were wavelength-dependent in all cases where it as tested, which is unusual.[22] This will be discussed in a case-by-case fashion.

Table 4.1 Relative Excited State Electron Transfer Yields, Φ_{rel}, and Reduction Potentials of cobalt macrocycles.

		$E_{1/2}$		Φ_{rel}	
		V *vs.* NHE	Co(I) Injection (relative yield±0.05)		
	Compound	Co(II/I)	436 nm	532 nm	683 nm
2	CoPPIX	-0.84	----	1	----
3	CoPc	-0.16	0.30	1	0.13
4a	CoP	-0.66	0.26	1	0.26
4b	CoTSP	-0.70	----	1	----

[a] *The reported reduction potential corresponds to Co(III/I). All data was taken from Ref.*[21]

The assembly of the cobalt porphyrin, compound **4a,** anchored to TiO_2, abbreviated TiO_2|CoP, was studied in detail.[12,23] Figure 4.4 shows the spectroelectrochemical characterization of TiO_2|CoP. The compound was initially present with the cobalt in the formal oxidation state of III. Raising the Fermi level of the TiO_2 thin film toward the vacuum level with a potentiostat led to the reduction of Co(III) (black line) to Co(II) (red line), (Figure 4.4A).

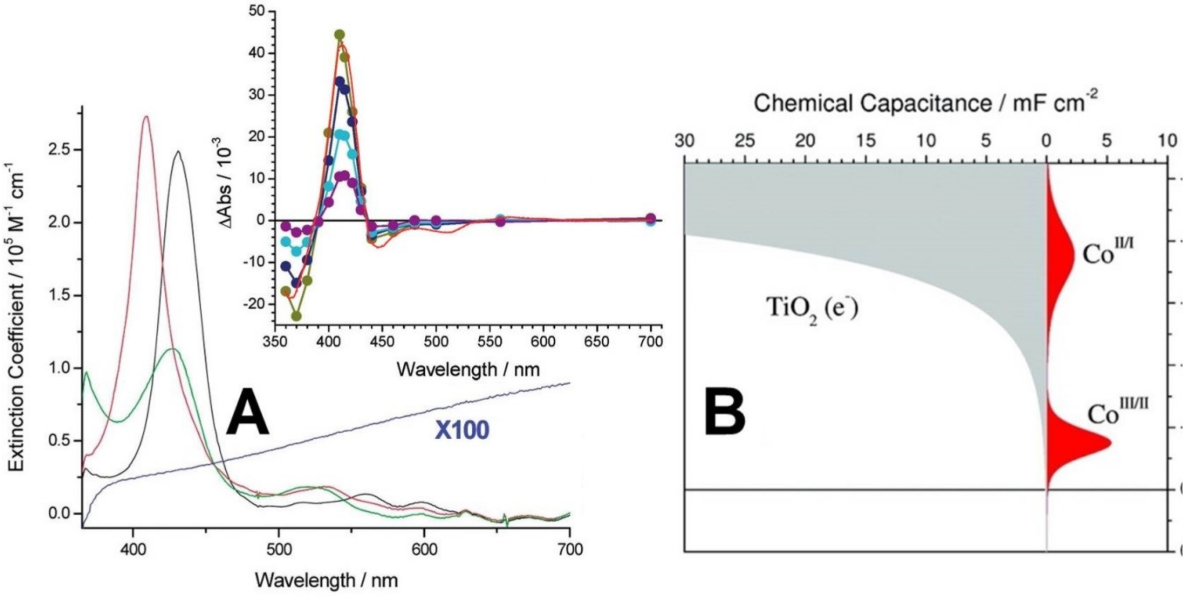

Figure 4.4 A) The absorbance of TiO_2|Co(I, II, III)P (green, red, black, respectively), and $TiO_2(e^-)$ (blue) multiplied by 100. Inset: The change in absorbance of TiO_2|Co(I)P after 532 nm pulsed laser excitation at delays times of 20 ns (olive), 500 ns (dark blue), 5.0 μs (light blue), and 60 μs (purple). The red line in the inset is the simulation of injection using the difference spectrum of Co(II) in the inset of part A of this figure. B) The chemical capacitance for Co(P)|TiO_2 thin film immersed in 0.1 M $LiClO_4/CH_3CN$ electrolyte. The Co(III/II) redox process was in reasonably modeled by the Nernst equation while the Co(II/I) redox reaction required non-ideality factors near 2. This figure was modified with permission from Refs. [12] and [24].

Increasingly negative applied potential led first to the appearance of electrons in TiO_2, $TiO_2(e^-)$s, that absorb weakly throughout the visible region. The $TiO_2(e^-)$ absorption spectrum is shown in an expanded scale in Figure 4.4A, blue line. Further reduction led to the appearance of spectral features diagnostic of Co(I) (green line). Although it was not studied in as much detail, these same redox events could be driven with bandgap excitation of TiO_2, when a few percent of methanol was included in the external CH_3CN electrolyte as a sacrificial electron donor.

The redox chemistry in itself was found to be interesting as it did not behave ideally. The Nernst equation predicts a factor of 10 change in concentration for every 59 mV potential step, but this redox chemistry at the TiO_2 interface required larger potential steps to realize the same factor of ten change in concentration. Such non-Nernstian behavior at electrode interfaces was well known, however a novel aspect of the Co redox chemistry was that *two* adjacent Co(III/II) and Co(II/I) reduction processes were quantified that provided new insights into the origins of the non-ideality. The Co(III/II) reduction process was close to Nernstian, however the Co(II/I) process was not (Figure 4.4B), particularly when the number of $TiO_2(e^-)$s was large. The non-ideality was attributed to the surface electric fields generated by these electrons that were essentially absent for the Co(III/II) process, yet were clearly present for the Co(II/I) reduction processes. In artificial photosynthetic assemblies where light is used to generate the Co(I) state, such non-ideal behavior is detrimental as the number of $TiO_2(e^-)$s, and hence, the absorbed photons necessary, is much greater than the case where the interface behaved ideally.

Pulsed laser excitation of TiO_2|Co(I)P resulted in excited state electron transfer consistent with Equation 4.1. With a TiO_2 thin film sensitized to visible light with the so-called N3 compound, *cis*-$Ru(dcb)_2(NCS)_2$, as an actinometer, the absolute excited state electron transfer quantum yield with 532 nm excitation was found to be 0.46 ± 0.06 [12]. The yields with blue or red light excitation were approximately ¼ this value. The relative quantum yields are given in Table 4.1.

It is probable that competitive light absorption by an MLCT excited state and the intraligand Q bands of the porphyrin macrocycle underlie the wavelength-dependent injection yields. Cobalt phthalocyanines, which have similar electronic structure (see below), have been shown to possess MLCT transitions at 532 nm by magnetic circular dichroism [25]. When D_{4h} symmetry of CoP is assumed, electric dipole selection rules stipulate that the MLCT must be a transition to the LUMO+1 or LUMO+2. Since the Soret and Q bands of CoP are intraligand $\pi \rightarrow \pi^*$ transitions to the LUMO,[26] it follows that the putative MLCT excited state of Co(I)P would be a stronger reductant. This energetic difference may be the cause of the higher injection yields at 532 than at 436 or 683 nm. Despite the thermodynamic favorability of injection from the $\pi \rightarrow \pi^*$ excited state, excitation of Co(III)P and Co(II)P, which lack MLCT transitions, resulted in no observable injection. The π orbitals of symmetric porphyrins are accordingly symmetric. Thus, a transition from one π orbital to another does not result in significant vectorial charge transfer toward the TiO_2 acceptor states. Given the probably short lifetime of the excited state, the directed motion of electrons in the MLCT transition may be crucial for injection. Successful injection from the $\pi \rightarrow \pi^*$ excited states of d^{10} Zn(II) porphyrins may be accounted for by their longer-lived excited states compared to Co(II)P and Co(III)P excited states. Furthermore, it has recently been shown that the addition of an internal dipole in Zn(II) porphyrins by adding donor and acceptor moieties increased the charge transfer character of one of the Soret excitations and cell efficiency.[27–29] Additionally, the d_{x2-y2} ligand field state that could result in lower injection yield is likely to be at higher energy than the LUMO + n corresponding to the MLCT, which may explain why the Co porphyrins are more efficient sensitizers than Fe compounds.[21]

The absorbance of the cobalt phthalocyanine compound anchored to TiO_2 (TiO_2|CoPc where CoPc is **3**) in the formal oxidation states of Co(I) and Co(II) are shown in Figure 4.5A [21]. Pulsed light excitation of TiO_2|Co(I)Pc resulted in the appearance of the long-lived transient species in Figure 4.5B that was well modelled by $TiO_2(e^-)$|Co(II)Pc (blue overlay).

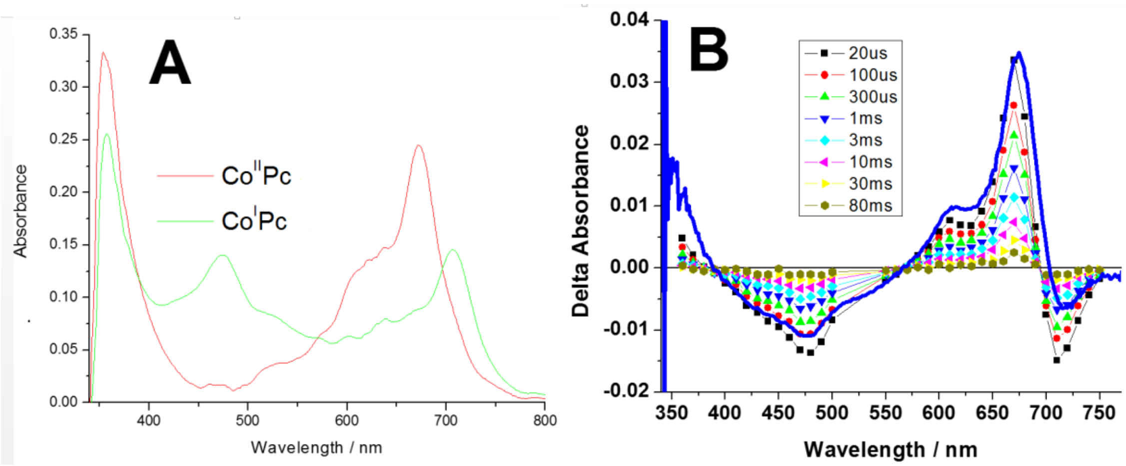

Figure 4.5 A) The absorbance of $TiO_2|CoPc$ in the Co(II) (red) and Co(I) (green) oxidation states. B) The change in absorbance of $TiO_2|Co(I)Pc$ after pulsed 532 nm laser excitation at the indicated delay times. Reproduced with permission from Ref. [21]

The relative injection yields of $TiO_2|CoPc$ (**3**) at 436, 532, and 683 nm did not follow the same energetic trend as the Co porphyrin or corrins. Instead, the yield was greatest at 532 nm, and the lowest yield was at 683 nm (0.13), while the yield at 436 nm was intermediate (0.30). This can be explained by the electronic structure of phthalocyanines, wherein the energies of electronic transitions are shifted relative to their porphyrin counterparts. In CoPc, the MLCT transition is positioned at ~470 nm, $\varepsilon \sim 80{,}000\ M^{-1}\ cm^{-1}$, between the Soret band at 310 nm and the primary Q band at 700 nm (see Figure 4A) [21,25]. Thus, the injection yield data supports injection from an MLCT excited state in this case also.

Previous results concerning recombination to Co(II) centers were summarized in section 1.5.2.b Effect of Applied Potential. In this chapter, electron injection into TiO_2 after photoexcitation of TiO_2-anchored cobalamin derivatives and applied-potential-dependent interfacial recombination from $TiO_2(e^-)$ to cob(II)alamin is described.

4.2 Experimental Methods

4.2.1 Materials

The following reagents were used as received from the indicated commercial suppliers: acetonitrile (Burdick and Jackson, spectrophotometric grade); dimethylsulfoxide (DMSO; Fisher Scientific, 99.9%); deionized water; tetra-*n*-butylammonium perchlorate ($TBAClO_4$; Fluka, >99.9%); tetra-n-butylammonium hydroxide (TBAOH; Fluka 1 M aqueous); vitamin B_{12} (cyanocobalamin, Sigma-Aldrich, >98.5%); dicyanocobyrinic acid heptamethyl ester (Sigma-Aldrich, >95%); argon gas (Airgas, >99.998%); titanium(IV)isopropoxide (Sigma-Aldrich, 97%); fluorine-doped SnO_2-coated glass (FTO; Hartford Glass Co., Inc., 2.3 mm thick, 15 Ω/□).

4.2.2 Sensitized Metal-Oxide Thin Film Electrode Preparation

Transparent TiO_2 nanocrystallites (anatase, ~15 nm diameter) were prepared by hydrolysis of Ti(*i*-OPr)$_4$ using a sol-gel technique previously described in the literature.[30] The sols were cast as mesoporous thin films (~ 5 µm thick), using Scotch tape as a spacer, by doctor blading onto transparent FTO conductive substrates. The thin films were annealed at 420^0 C for 30 min under an atmosphere of O_2 flow.

The films were pretreated with aqueous base (TBAOH, pH ~ 11) for 10 min, followed by an acetonitrile wash, and were then immersed in acetonitrile solution containing cyanocobalamin (sparingly soluble) or dicyanocobyrinic acid heptamethyl ester (soluble). Over the course of 3 or more days, the films became colored (cyanocobalamin/pink, dicyanocobyrinic acid heptamethyl ester/purple) and were washed thoroughly with 100 mM $TBAClO_4$/acetonitrile and placed diagonally in a standard 1 cm^2 quartz cuvette containing the electrolyte solution. The electrolyte solution was sparged with Ar gas for at least 30 min prior to experimentation. The surface coverage, Γ, in mol / cm^2, was quantified from the measured absorption with the modified Beer-Lambert formula given in Equation 4.2,

$$Abs = 1000 \cdot \Gamma \cdot \varepsilon \qquad 4.2$$

where ε is the molar decadic extinction (absorption) coefficient, M^{-1} cm^{-1}, that was assumed to be unchanged whether in solution or on the surface. The complexes were typically anchored to the films in coverages of $\Gamma = 2 - 5 \times 10^{-9}$ mol/cm^2.

4.2.3 Spectroscopy

Steady-state UV-visible absorption spectra were obtained on either a Varian Cary 50 spectrophotometer or a Hewlett Packard 8453 Photodiode Array spectrophotometer at room temperature. Attenuated total reflectance (ATR) Fourier transform infrared (FTIR) spectroscopy was performed on a Nexus 670 Thermo-Nicolet FTIR spectrometer coupled with a Golden Gate ATR module. Nanosecond transient absorption spectra were obtained on an apparatus similar to that which has been previously described. Samples were irradiated with 532 nm light from a frequency doubled Q-switched, pulsed Nd:YAG laser (Quantel USA (BigSky) Brilliant B; 5-6 ns full width at half-maximum, 1 Hz, ~ 10 mm in diameter) directed 45^0 to the FTO side of a TiO_2 film. The excitation fluence was measured by a thermopile power meter (Molectron) and was typically < 2 mJ / cm^2. A 150 W xenon arc lamp served as the probe beam (Applied Photophysics) that was aligned orthogonally to the laser excitation and directed to a monochromator (Spex 1702/04) optically coupled to an R928 photomultiplier tube (Hamamatsu). Transient data were acquired on a computer-interfaced 350 MHz digital oscilloscope (LeCroy 9450). In typical experiments, 30 laser pulses were averaged at each monitoring wavelength. The kinetic data were fit with the Kohlrausch Williams-Watts stretched exponential function, Equation 4.3.

$$\Delta A = A_0 \cdot e^{-(kt)^{\beta}} \tag{4.3}$$

4.2.4 Electrochemistry

Electrochemical measurements utilized a potentiostat (BAS model CV-50W or Epsilon electrochemical analyzer) in a standard three electrode arrangement with a glassy carbon disk (solution) or sensitized TiO_2 thin film deposited on FTO glass (surface) working electrode, a Pt gauze or Pt disk (Bioanalytical Scientific Instruments, Inc.) counter electrode, and aqueous Ag/AgCl (KCl saturated) reference electrode. All potentials are reported *vs.* NHE unless otherwise noted. The ferrocenium/ferrocene ($Fe(Cp)_2^{+/0}$) half-wave potential was measured both before and after experiment in a 100 mM $TBAClO_4$/acetonitrile electrolyte and was used as a standard to calibrate the reference electrode. Conversion to *vs.* NHE was achieved by correcting for the expected ferrocenium/ferrocene $E_{1/2}$ of + 310 mV *vs.* the KCl-saturated aqueous calomel electrode (SCE), where SCE is +241 mV *vs.* NHE.

The general procedure for spectroelectrochemical measurements was similar to that which has been previously reported.[24]

Spectroelectrochemistry was executed through simultaneous application of an applied potential bias while monitoring the UV-Vis absorption of the TiO_2|Cob thin film electrode which was oriented diagonally in a square quartz cuvette. The electrolyte was 100 mM tetrabutylammonium perchlorate in CH_3CN. At each potential step, a spectrum that was invariant with time was recorded. Single-wavelength absorption features plotted as a function of potential bias were proportional to the cumulative formation/loss of states. The spectra of Co(II) and Co(I) species were recorded after the associated peaks no longer grew in intensity with incrementally more negative applied bias, but before the associated peaks began to decrease in intensity with increasingly negative applied bias.

4.3 Results and Discussion

A thin film (~10 μm) of nanocrystalline, mesoporous anatase titania was deposited on a transparent conductive glass (fluorine-doped tin oxide, FTO) and sintered at 420 °C for 30 minutes. Cyanocobalamin (vitamin B_{12}) or dicyanocobyrinic acid heptamethyl ester (a B_{12} derivative herein referred to as cobyrinate) was anchored to the thin film by soaking in a dilute acetonitrile solution of the chromophore to form an electrode hereafter referred to as TiO_2|Cob(III) (see cartoon in Fig. 1 inset). It was assumed that the cobyrinate was attached to the TiO_2 in the typical way, through the ester groups. However, since cyanocobalamin contains neither esters nor carboxylate groups, the mode of attachment was not clear. The possibilities we considered include amide groups, of which there are many, the phosphate group that links the axial benzimidizole ligand, or alcohol groups. Alternatively, the cyanocoblamin may have been anchored by physisorption. The mode of attachment to the TiO_2 film for cyanoconalamin was investigated using Fourier Transform Infrared spectroscopy, see Figure 4.6. Amide and phosphate transitions are shown. There was a slight shift in the free amide peak at ~1660 cm^{-1} to ~1670 cm^{-1} in the bound forms, but this data did not provide convincing evidence for surface anchoring through the amide moieties.

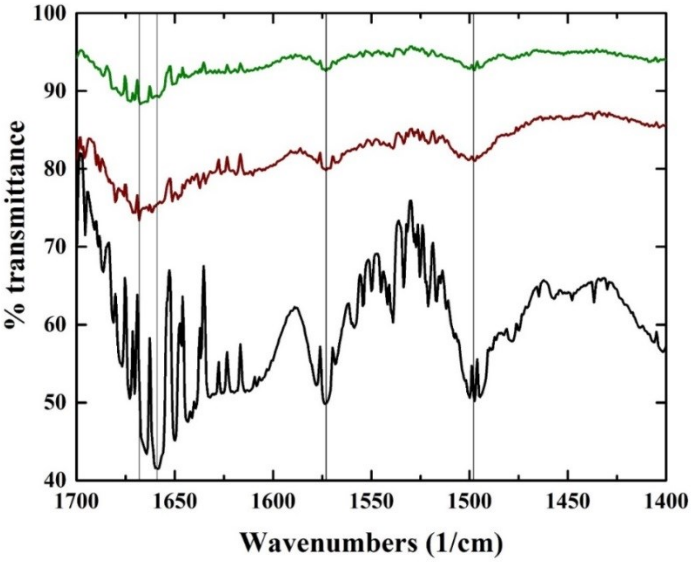

Figure 4.6 The FTIR spectra of cyanocob(III)alamin in powder form (black), a TiO_2 film sensitized by cyanocob(III)alamin (green), and TiO_2 film sensitized by cyanocob(III)alamin, and scraped off the glass substrate to form a powder (red).

In a standard 3 electrode cell under argon atmosphere, the TiO_2|Cob(III) working electrode was immersed in a 100 mM tetrabutylammonium perchlorate (TBAP) acetonitrile solution with a Pt mesh counter electrode and a Ag/AgCl reference electrode. A forward bias was applied potentiostatically to sequentially reduce TiO_2|Cob(III) to TiO_2|Cob(II) and TiO_2|Cob(I). The identity of the reduced species was verified by electronic absorbance spectra, Figure 4.7 top. The absorbance spectra of the TiO_2|Cobyrinate in the Co(I) and Co(III) oxidation states were very similar, Figure 4.7 bottom. The Co(II) spectrum was not acquired because Co(II) rapidly disproportionates to Co(I) and Co(III)$(CN)_2$ in the presence of excess cyanide. The absorbance profiles closely matched those generated by chemical reduction in solution (Figure 4.8 A vs. B) and were consistent with literature spectra.[31]

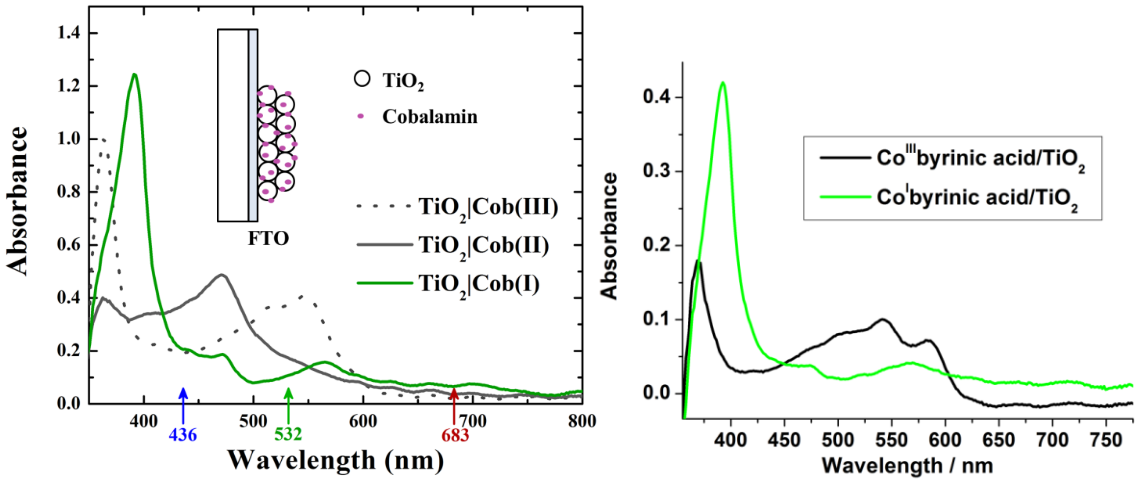

Figure 4.7 Top) The absorbance of cobalamin anchored to TiO_2 in 100 mM tetrabutylammonium perchlorate CH_3CN in the cyanocob(III)alamin (grey dotted), cob(II)alamin (grey solid), and cob(I)alamin (green) oxidation states. The inset shows a cartoon of the sample: FTO coated glass with a thin (~10 μm) film of TiO_2 nanoparticles (~20 nm diameter), to which the cyanocobalamin was anchored. The colored arrows along the horizontal axis indicate the excitation wavelengths utilized in transient absorption experiments. Bottom) The absorbance of TiO_2|Dicyanocobyrinate (black) and the electrochemically reduced TiO_2|Cob(I)yrinate (green) in 100 mM $TBAClO_4$ CH_3CN. The contributions of the TiO_2 and $TiO_2(e^-)$ present at the required applied potential have been subtracted.

In its reduced state, TiO_2|Cob(I) was irradiated with pulsed laser excitation at 1 Hz, and the time-resolved change in absorbance was monitored using a previously described apparatus[32] (cobalamin data shown in Figure 4.9). There was a decrease in absorbance centered at ~390 nm and a relatively small increase in absorbance at wavelengths lower in energy than the ~416 nm isosbestic point between TiO_2|Cob(I) and TiO_2|Cob(II), Figure 4.7 and Figure 4.9.

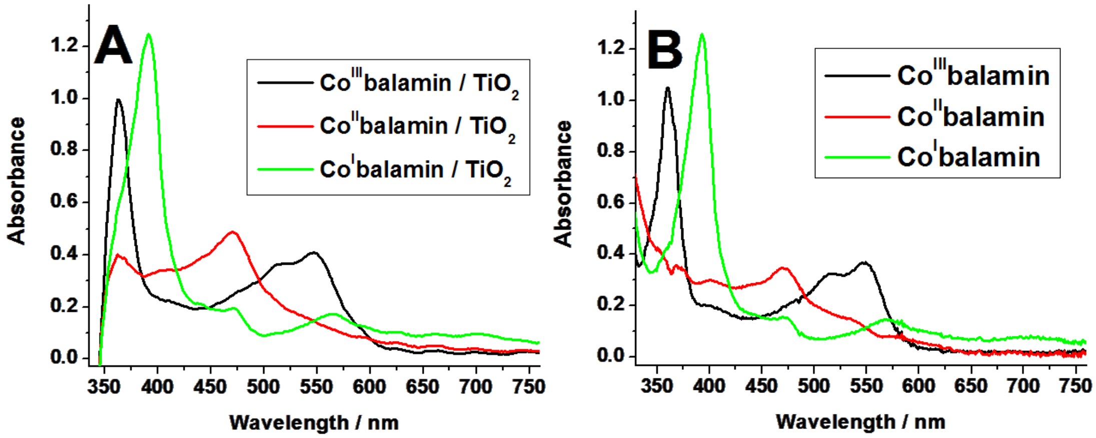

Figure 4.8 A) The absorbance of TiO_2|Cyanocob(III)alamin (black) and the electrochemically reduced TiO_2|Cob(II)alamin and TiO_2|Cob(I)alamin (red and green, respectively) in 100 mM $TBAClO_4$ CH_3CN. The contributions of the TiO_2 and $TiO_2(e^-)$ present at the required applied potential have been subtracted. B) The absorbance of cyanocob(III)alamin (black) in DMSO solution and the photochemically reduced cob(II)almin (red) and cob(I)alamin (green) in DMSO solution. The photoreduction was accomplished in DMSO using a xenon lamp, Re(4,4'-diethylester-2,2'-bipyridine)$(CO)_3$(4-ethylpyridine)(OTf^-) as a photoreductant, and triethylamine as a sacrificial reductant.

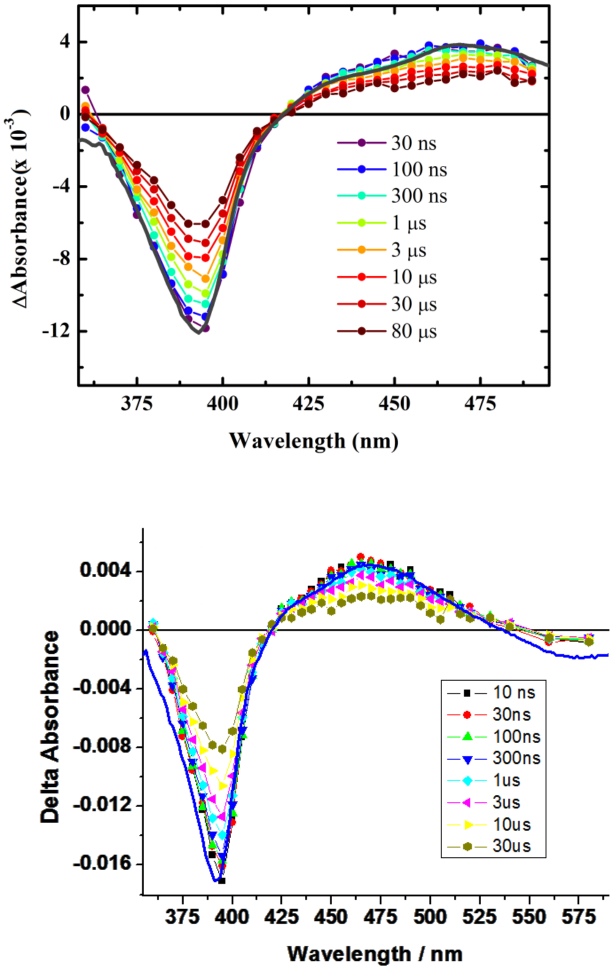

Figure 4.9 Top) The change in absorbance of TiO_2|Cob(I) in 100 mM tetrabutylammonium perchlorate CH_3CN after 532 nm pulsed laser excitation. The full-width at half maximum of the excitation beam was ~10 ns. The dark grey line overlaid is the simulated difference spectrum using the scaled difference between TiO_2|Cob(II) and TiO_2|Cob(I). Bottom) The change in absorbance of TiO_2|Cob(I)yrinate after 532 nm pulsed laser excitation as a function of wavelength, at the indicated delay times.

The overlaid solid line in Figure 4.9 is the scaled difference between the authentic spectra of TiO_2|Cob(II) and TiO_2|Cob(I). This simulation provides an excellent match to the observed spectral data, confirming that the electron transfer reaction in Equation 4.1 occurred within the instrument response time, $k_{et} > 10^8$ s^{-1}.

Cob(II) was reduced to Cob(I) on a micro- to millisecond timescale *via* interfacial charge recombination (Equation 4.4) with maintenance of isosbestic points, implying a conversion between only these two states.

$$TiO_2(e^-)|Cob(II) \rightarrow TiO_2|Cob(I) \qquad 4.4$$

The charge recombination (Equation 4.4) kinetics were non-exponential, but were well modeled by a by the Kohlrausch Williams-Watts stretched exponential function[33–35] (Equation 4.3) to obtain a pseudo first-order rate constant.[36] Similar behavior was observed for the cobyrinate (Figure 4.9, bottom), and the kinetic analysis is presented in Figure 4.10 as representative of both cobalamin derivatives. It was found that the rate constant for Equation 4.4 was exponentially dependent upon the potentiostatically controlled quasi-Fermi level, and spanned from 10^3 – 10^7 s^{-1} for the applied potential range used (Figure 4.11).

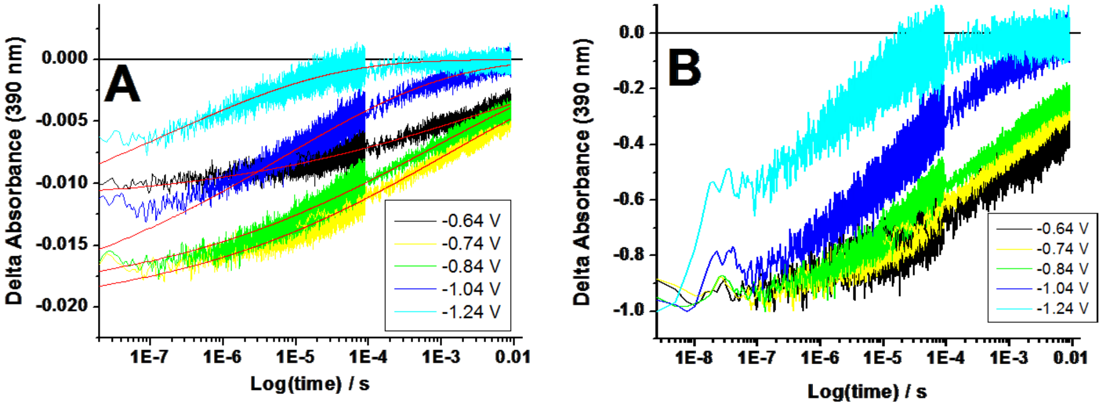

Figure 4.10 A) The change in absorbance of TiO_2|Cob(I)yrinate at 390 nm after 532 nm pulsed laser excitation as a function of time. Fits to Equation 4.3 with β = 0.19 are overlaid in red. B) The data in part A of this figure normalized to the initial absorbance change.

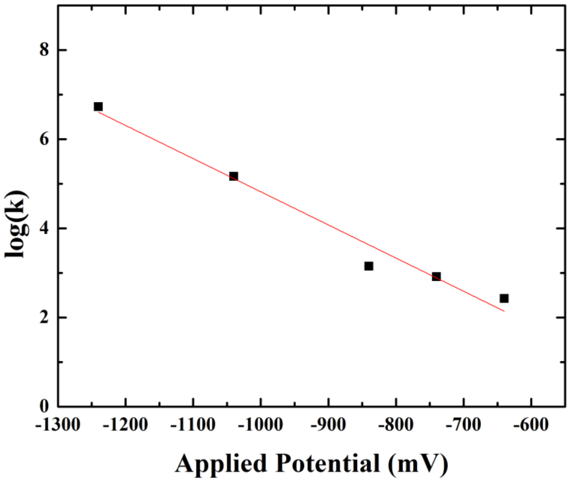

Figure 4.11 The logarithm of the rate constant *k* abstracted from the data in Figure 4.10 using the KWW function (Equation 4.3) and the reciprocal relationship between lifetime and rate constant ($1/k = \tau$) plotted as a function of the applied potential *vs*. NHE. The linear relationship, with a slope of -7.4, is similar to that seen for interfacial recombination in other TiO_2|chromophore assemblies.[12,36–38]

These observations are consistent with previously reported interfacial recombination.[12] The exact lifetimes and corresponding transient absorption data can be found in Table 4.2.

Table 4.2 Applied Bias and Average Lifetimes (τ).

Applied bias *vs.* NHE (V)	τ (KWW) (s^{-1})
-0.64	3.75×10^{-3}
-0.74	1.21×10^{-3}
-0.84	7.08×10^{-4}
-1.04	6.76×10^{-6}
-1.24	1.86×10^{-7}

The transient absorption spectra shown in Figure 4.9 were measured after 532 nm excitation, but can be taken as representative, as the transient absorbance spectra after 532, 436, and 683 nm excitation were found to be normalizable within experimental error. The excitation wavelengths are indicated by arrows on the horizontal axis of Figure 4.7, top. The relative quantum yield of excited state electron transfer was quantified by transient absorption 20 ns after excitation. The concentration of the Co(II) compound formed was quantified and divided by the number of absorbed photons at the excitation wavelength. This was repeated at all three excitation wavelengths and the highest yield was assigned a value of unity (Table 4.3).

Table 4.3 The relative quantum yields, Φ_{rel}, and reduction potentials of TiO_2|Cobalamin and TiO_2|Cobyrinate measured in 100 mM tetrabutyl ammonium perchlorate CH_3CN.

	V *vs.* NHE	Φ_{rel} ($\pm$0.05)		
Complex	Co(II/I)	436 nm	532 nm	683 nm
TiO_2|Cobalamin	-0.63	0.15	1	0.95
TiO_2|Cobyrinate‡	--	0.21	0.98	1

‡Cobyrinate = dicyanocobyrinic acid heptamethyl ester, the Co(II/I) reduction potential for TiO_2|Cobyrinate was not directly observed as the presence of cyanide causes Co(II) to rapidly disproportionate, however it is expected to be similar to TiO_2|Cobalamin.[**11,19**]

It was found that the relative excited state electron transfer yield was wavelength-dependent, 532 and 683 nm excitation were within error of unity, but the yield for 436 nm excitation was only ~0.2. The reason for this is uncertain. The difference cannot be attributed to photo-decomposition as there was no change in the visible absorbance spectrum after laser irradiation of any wavelength used. The visible absorption spectrum of cob(I)alamin has been attributed to corrin-localized π→π* excitations.[39,40] However, recent computational and spectroscopic studies point toward considerable metal-to-ligand charge transfer (MLCT) character in the lower energy transitions.[11,41–44] The calculations of Brunold and coworkers indicate that the absorption at 436 nm consists of only 20% MLCT character, compared to 70% and >99% at 532 and 683 nm.[11] Thus, competitive absorption from π→π* transitions may account for the significantly lower electron transfer yield measured after 436 nm excitation. Although the computed excited state energy of the π→π* transition is thermodynamically capable of electron transfer to the acceptor states of TiO_2,[43] the MLCT is likely to be more directed, with a large change in the dipole moment. We note that the π→π* excited states of other open-shell macrocycles, such as hemes, do not undergo excited state electron transfer reactions.[45]

The excited state reduction potential of cob(II/I*)alamin can be estimated from the measured Co(II/I) reduction potential and the free energy stored in the excited state.[46] The $E^0(Co^{II/I})$ was measured by spectroelectrochemistry, Table 4.3. As the free energy in the excited state is not known, the longest wavelength where MLCT transitions are expected to be significant by Brunold et al. (950 nm) was used as an estimate. This calculation yielded $E^0(Co^{II/I*}) \approx -1900$ mV *vs.* NHE, a very potent reductant. The low energy absorption of the biomolecule raises the question of the consequences of possible *in vivo* excitation of cob(I)alamin to transiently form such a potent reductant.

Electron transfer from the excited state of an open-shell, first-row metal is uncommon behaviour, the absence of which is frequently explained by thermal deactivation of the excited state *via* low lying ligand field states preventing injection. However, photo-induced electron transfer from d^8 transition metals has previously been observed, suggesting that this deactivation pathway does not kinetically out-compete excited state electron transfer.[47] Although the photo-induced cleavage of the Co(III)-C bond in cobalamins has been known for some time, to our knowledge photo-induced outer sphere electron transfer has not been reported for any cob(I)alamin species.[24,48–55]

4.4 Conclusions

Vitamin B_{12} was anchored to TiO_2 and the cob(I)alamin state was produced electrochemically. Upon light excitation, excited state electron transfer yielded $TiO_2(e^-)|$cob(II)alamin with $k_{et} > 10^8$ s^{-1}. The excitation wavelength dependence suggested electron transfer from an MLCT excited state rather than a ligand localized $\pi \rightarrow \pi^*$ excited state. Despite the long fascination of biochemists and inorganic chemists alike, the essential cofactor cob(I)alamin has not previously been observed to undergo excited state electron transfer.

Although the cobalt sensitizers discussed here do not have appropriate Co(II/I) potentials for use in existing DSSCs, it may be possible to stabilize the Co(I) state by tuning the electron withdrawing ability of the macrocycle ligand. Additionally, it is possible that the ability to efficiently sensitize TiO_2 to visible light is not limited to cobalt complexes. In the future, other square planar complexes of d^8 first-row metals should be investigated. If an injecting complex with a d^8 oxidation state that is stable in the presence of oxygen can be identified, these complexes may find useful application in more cost-effective DSSCs. In such a device, the employment of an optimized axial base may hinder recombination to the oxidized sensitizer, improving the efficiency of the cell.

4.5 References

(1) Banerjee, R. Radical Carbon Skeleton Rearrangements: Catalysis by Coenzyme B_{12}-Dependent Mutases. *Chem. Rev.* **2003**, *103* (6), 2083–2094.

(2) Kräutler, B.; Arigoni, D.; Golding, B. T. *Vitamin B_{12} and B_{12}-Proteins*; Wiley-VCH, 1998.

(3) Toraya, T. Radical Catalysis in Coenzyme B_{12}-Dependent Isomerization (Eliminating) Reactions. *Chem. Rev.* **2003**, *103* (6), 2095–2128.

(4) Buckel, W.; Golding, B. T. Glutamate and 2-Methyleneglutarate Mutase: From Microbial Curiosities to Paradigms for Coenzyme B12-Dependent Enzymes. *Chem. Soc. Rev.* **1996**, *25* (5), 329–337.

(5) Matthews, R. G. Cobalamin-Dependent Methyltransferases. *Acc. Chem. Res.* **2001**, *34* (8), 681–689.

(6) Thauer, R. K. Biochemistry of Methanogenesis: A Tribute to Marjory Stephenson:1998 Marjory Stephenson Prize Lecture. *Microbiology* **1998**, *144* (9), 2377–2406.

(7) Lenhert, P. G.; Hodgkin, D. C. Structure of the 5,6-Dimethylbenzimidazolylcobamide Coenzyme. *Nature* **1961**, *192* (4806), 937–938.

(8) Hodgkin, D. C.; Pickworth, J.; Robertson, J. H.; Trueblood, K. N.; Prosen, R. J.; White, J. G. Structure of Vitamin B_{12} : The Crystal Structure of the Hexacarboxylic Acid Derived from B_{12} and the Molecular Structure of the Vitamin. *Nature* **1955**, *176* (4477), 325–328.

(9) Banerjee, R.; Ragsdale, S. W. The Many Faces of Vitamin B12: Catalysis by Cobalamin-Dependent Enzymes 1. *Annu. Rev. Biochem.* **2003**, *72*, 209–247.

(10) Bertini, I.; Gray, H. B.; Stiefel, E. I.; Valen, J. S. *Biological Inorganic Chemistry: Structure and Reactivity*; University Science Books: Sausalito, Calif., 2007.

(11) Liptak, M. D.; Brunold, T. C. Spectroscopic and Computational Studies of Co^{1+} Cobalamin: Spectral and Electronic Properties of the "Superreduced" B_{12} Cofactor. *J. Am. Chem. Soc.* **2006**, *128* (28), 9144–9156.

(12) Achey, D.; Ardo, S.; Xia, H.-L.; Siegler, M. A.; Meyer, G. J. Sensitization of TiO_2 by the MLCT Excited State of CoI Coordination Compounds. *J. Phys. Chem. Lett.* **2011**, *2* (4), 305–308.

(13) Gupta, B. D.; Qanungo, K. Pyrazine Bridged Organodicobaloximes: A Convenient One Pot Synthesis and Cis Influence Studies. *J. Organomet. Chem.* **1998**, *557* (2), 243–249.

(14) Endres, H.; Keller, H. J.; Lehmann, R.; Poveda, A.; Rupp, H. H.; van de Sand, H. *Z. Für Naturforschung B* **1968**, *11*, 61–70.

(15) Schrauzer, G. N.; Parshall, G. W.; Wonchoba, E. R. Bis(Dimethylglyoximato)Cobalt Complexes: ("Cobaloximes"). In *Inorganic Syntheses*; Jolly, W. L., Ed.; John Wiley & Sons, Inc., 1968; pp 61–70.

(16) Fitzgerald, R. J.; Hutchinson, B. B.; Nakamoto, K. Contact Shift Studies and Spin Delocalization in cobalt(I)-tris(2,2'-Bipyridine) Complexes. *Inorg. Chem.* **1970**, *9* (11), 2618–2621.

(17) Kaizu, Y.; Torii, Y.; Kobayashi, H. Electronic Absorption Spectrum of Tris(2,2′-Bipyridine)-cobalt(I) Complex. *Bull. Chem. Soc. Jpn.* **1970**, *43* (10), 3296–3297.

(18) Szalda, D. J.; Creutz, C.; Mahajan, D.; Sutin, N. Electron-Transfer Barriers and Metal-Ligand Bonding as a Function of Metal Oxidation State. 2. Crystal and Molecular Structures of tris(2,2'-bipyridine)cobalt(II) Dichloride-2-Water-Ethanol and tris(2,2'-bipyridine)cobalt(I) Chloride-Water. *Inorg. Chem.* **1983**, *22* (17), 2372–2379.

(19) Ardo, S.; Sun, Y.; Staniszewski, A.; Castellano, F. N.; Meyer, G. J. Stark Effects after Excited-State Interfacial Electron Transfer at Sensitized TiO_2 Nanocrystallites. *J. Am. Chem. Soc.* **2010**, *132* (19), 6696–6709.

(20) Cappel, U. B.; Feldt, S. M.; Schöneboom, J.; Hagfeldt, A.; Boschloo, G. The Influence of Local Electric Fields on Photoinduced Absorption in Dye-Sensitized Solar Cells. *J. Am. Chem. Soc.* **2010**, *132* (26), 9096–9101.

(21) Achey, D. C. Cobalt and Nickel Macrocycles Anchored to Nanocrystalline Titanium Dioxide Thin Films: Sensitization, Catalysis, and Ligand Association. Ph.D., The Johns Hopkins University: United States -- Maryland, 2013.

(22) Ferrere, S.; Gregg, B. A. Photosensitization of TiO_2 by $[Fe^{II}(2,2'$-Bipyridine-4,4'-Dicarboxylic acid$)_2(CN)_2]$: Band Selective Electron Injection from Ultra-Short-Lived Excited States. *J. Am. Chem. Soc.* **1998**, *120* (4), 843–844.

(23) Achey, D.; Ardo, S.; Meyer, G. J. Increase in the Coordination Number of a Cobalt Porphyrin after Photo-Induced Interfacial Electron Transfer into Nanocrystalline TiO_2. *Inorg. Chem.* **2012**, *51* (18), 9865–9872.

(24) Ardo, S.; Achey, D.; Morris, A. J.; Abrahamsson, M.; Meyer, G. J. Non-Nernstian Two-Electron Transfer Photocatalysis at Metalloporphyrin–TiO_2 Interfaces. *J Am Chem Soc* **2011**, *133* (41), 16572–16580.

(25) Musil, Z.; Zimcik, P.; Miletin, M.; Kopecky, K.; Petrik, P.; Lenco, J. Influence of Electron-Withdrawing and Electron-Donating Substituents on Photophysical Properties of Azaphthalocyanines. *J. Photochem. Photobiol. Chem.* **2007**, *186* (2–3), 316–322.

(26) Gouterman, M. Study of the Effects of Substitution on the Absorption Spectra of Porphin. *J. Chem. Phys.* **1959**, *30* (5), 1139–1161.

(27) Yella, A.; Mai, C.-L.; Zakeeruddin, S. M.; Chang, S.-N.; Hsieh, C.-H.; Yeh, C.-Y.; Grätzel, M. Molecular Engineering of Push-Pull Porphyrin Dyes for Highly Efficient Dye-Sensitized Solar Cells: The Role of Benzene Spacers. *Angew. Chem. Int. Ed.* **2014**, *53* (11), 2973–2977.

(28) Yella, A.; Lee, H.-W.; Tsao, H. N.; Yi, C.; Chandiran, A. K.; Nazeeruddin, M. K.; Diau, E. W.-G.; Yeh, C.-Y.; Zakeeruddin, S. M.; Grätzel, M. Porphyrin-Sensitized Solar Cells with Cobalt (II/III)–Based Redox Electrolyte Exceed 12 Percent Efficiency. *Science* **2011**, *334* (6056), 629–634.

(29) Mathew, S.; Yella, A.; Gao, P.; Humphry-Baker, R.; Curchod, B. F. E.; Ashari-Astani, N.; Tavernelli, I.; Rothlisberger, U.; Nazeeruddin, M. K.; Grätzel, M. Dye-Sensitized Solar Cells with 13% Efficiency Achieved through the Molecular Engineering of Porphyrin Sensitizers. *Nat. Chem.* **2014**, *6* (3), 242–247.

(30) Heimer, T. A.; D'Arcangelis, S. T.; Farzad, F.; Stipkala, J. M.; Meyer, G. J. An Acetylacetonate-Based Semiconductor−Sensitizer Linkage. *Inorg. Chem.* **1996**, *35* (18), 5319–5324.

(31) Lexa, D.; Sayeant, J. M.; Zickler, J. Electrochemistry of Vitamin B_{12}. 5. Cyanocobalamins. *J. Am. Chem. Soc.* **1980**, *102* (8), 2654–2663.

(32) Argazzi, R.; Bignozzi, C. A.; Heimer, T. A.; Castellano, F. N.; Meyer, G. J. Enhanced Spectral Sensitivity from Ruthenium(II) Polypyridyl Based Photovoltaic Devices. *Inorg. Chem.* **1994**, *33* (25), 5741–5749.

(33) Kohlrausch, R. Theorie Des Elektrischen Rückstandes in Der Leidener Flasche. *Ann. Phys. Chem. Leipz.* **1854**, *91*, 56–82.

(34) Williams, G.; Watts, D. C. Non-Symmetrical Dielectric Relaxation Behaviour Arising from a Simple Empirical Decay Function. *Trans. Faraday Soc.* **1970**, *66* (0), 80–85.

(35) Scher, H.; Montroll, E. W. Anomalous Transit-Time Dispersion in Amorphous Solids. *Phys. Rev. B* **1975**, *12* (6), 2455–2477.

(36) Brigham, E. C.; Meyer, G. J. Ostwald Isolation to Determine the Reaction Order for $TiO_2(e^-)|S^+ \rightarrow TiO_2|S$ Charge Recombination at Sensitized TiO_2 Interfaces. *J. Phys. Chem. C* **2014**, *118* (15), 7886–7893.

(37) Haque, S. A.; Tachibana, Y.; Klug, D. R.; Durrant, J. R. Charge Recombination Kinetics in Dye-Sensitized Nanocrystalline Titanium Dioxide Films under Externally Applied Bias. *J. Phys. Chem. B* **1998**, *102* (10), 1745–1749.

(38) Nelson, J.; Haque, S. A.; Klug, D. R.; Durrant, J. R. Trap-Limited Recombination in Dye-Sensitized Nanocrystalline Metal Oxide Electrodes. *Phys. Rev. B* **2001**, *63* (20), 205321.

(39) Giannotti, C. *B12*; Dolphin, D., Ed.; Wiley, 1982.

(40) Pratt, J. M. *Chemistry and Biochemistry of B_{12}*; Banerjee, R., Ed.; Wiley: New York, 1999.

(41) Stich, T. A.; Brooks, A. J.; Buan, N. R.; Brunold, T. C. Spectroscopic and Computational Studies of Co^{3+}-Corrinoids: Spectral and Electronic Properties of the B_{12} Cofactors and Biologically Relevant Precursors. *J Am Chem Soc* **2003**, *125* (19), 5897–5914.

(42) Stich, T. A.; Yamanishi, M.; Banerjee, R.; Brunold, T. C. Spectroscopic Evidence for the Formation of a Four-Coordinate Co^{2+} Cobalamin Species upon Binding to the Human ATP:Cobalamin Adenosyltransferase. *J Am Chem Soc* **2005**, *127* (21), 7660–7661.

(43) Park, K.; Brunold, T. C. Combined Spectroscopic and Computational Analysis of the Vibrational Properties of Vitamin B_{12} in Its Co^{3+}, Co^{2+}, and Co^{1+} Oxidation States. *J. Phys. Chem. B* **2013**, *117* (18), 5397–5410.

(44) Kornobis, K.; Ruud, K.; Kozlowski, P. M. Cob(I)alamin: Insight Into the Nature of Electronically Excited States Elucidated via Quantum Chemical Computations and Analysis of Absorption, CD and MCD Data. *J. Phys. Chem. A* **2013**, *117* (5), 863–876.

(45) Morris, A. J.; Stromberg, J. R.; Meyer, G. J. Dynamics and Equilibrium of Heme Axial Ligation in Mesoporous Nanocrystalline TiO_2 Thin Films. *Inorg. Chem.* **2010**, *49* (1), 29–37.

(46) Juris, A.; Balzani, V.; Barigelletti, F.; Campagna, S.; Belser, P.; von Zelewsky, A. Ru(II) Polypyridine Complexes: Photophysics, Photochemistry, Eletrochemistry, and Chemiluminescence. *Coord. Chem. Rev.* **1988**, *84*, 85–277.

(47) Lexa, D.; Saveant, J. M. The Electrochemistry of Vitamin B_{12}. *Acc. Chem. Res.* **1983**, *16* (7), 235–243.

(48) Sension, R. J.; Harris, D. A.; Stickrath, A.; Cole, A. G.; Fox, C. C.; Marsh, E. N. G. Time-Resolved Measurements of the Photolysis and Recombination of Adenosylcobalamin Bound to Glutamate Mutase. *J Phys Chem B* **2005**, *109* (38), 18146–18152.

(49) Cole, A. G.; Yoder, L. M.; Shiang, J. J.; Anderson, N. A.; Walker, L. A.; Banaszak Holl, M. M.; Sension, R. J. Time-Resolved Spectroscopic Studies of B_{12} Coenzymes: A Comparison of the Primary Photolysis Mechanism in Methyl-, Ethyl-, N-Propyl-, and 5‘-Deoxyadenosylcobalamin. *J Am Chem Soc* **2001**, *124* (3), 434–441.

(50) Sension, R. J.; Harris, D. A.; Cole, A. G. Time-Resolved Spectroscopic Studies of B_{12} Coenzymes: Comparison of the Influence of Solvent on the Primary Photolysis Mechanism and Geminate Recombination of Methyl-, Ethyl-, N-Propyl-, and 5‘-Deoxyadenosylcobalamin. *J Phys Chem B* **2005**, *109* (46), 21954–21962.

(51) Yoder, L. M.; Cole, A. G.; Walker, L. A.; Sension, R. J. Time-Resolved Spectroscopic Studies of B_{12} Coenzymes: Influence of Solvent on the Photolysis of Adenosylcobalamin. *J Phys Chem B* **2001**, *105* (48), 12180–12188.

(52) Walker, L. A.; Jarrett, J. T.; Anderson, N. A.; Pullen, S. H.; Matthews, R. G.; Sension, R. J. Time-Resolved Spectroscopic Studies of B_{12} Coenzymes: The Identification of a Metastable Cob(III)alamin Photoproduct in the Photolysis of Methylcobalamin. *J Am Chem Soc* **1998**, *120* (15), 3597–3603.

(53) Walker, L. A.; Shiang, J. J.; Anderson, N. A.; Pullen, S. H.; Sension, R. J. Time-Resolved Spectroscopic Studies of B_{12} Coenzymes: The Photolysis and Geminate Recombination of Adenosylcobalamin. *J Am Chem Soc* **1998**, *120* (29), 7286–7292.

(54) Shiang, J. J.; Walker, L. A.; Anderson, N. A.; Cole, A. G.; Sension, R. J. Time-Resolved Spectroscopic Studies of B_{12} Coenzymes: The Photolysis of Methylcobalamin Is Wavelength Dependent. *J Phys Chem B* **1999**, *103* (47), 10532–10539.

(55) Shiang, J. J.; Cole, A. G.; Sension, R. J.; Hang, K.; Weng, Y.; Trommel, J. S.; Marzilli, L. G.; Lian, T. Ultrafast Excited-State Dynamics in Vitamin B_{12} and Related Cob(III)alamins. *J Am Chem Soc* **2005**, *128* (3), 801–808.

Chapter 5. TiO_2 Sensitized to Long Wavelengths of Light by an Asymmetric Phlorin Macrocycle

Allen J. Pistner synthesized the phlorin molecule for this work in the laboratory of Joel Rosenthal of the Department of Chemistry and Biochemistry at the University of Delaware, Newark, Delaware 19716, United States.

5.1 Introduction

There is a great need to find less expensive and more efficient materials for solar power conversion and storage. The dye-sensitized solar cell is one of many attempts to create less expensive photovoltaics, enlisting a molecular sensitizer, to absorb in the visible region, bound to the exceptionally large surface area of a low-purity, wide band gap semiconductor. So far, the most typical successful molecular sensitizers have been ruthenium polypyridyl compounds. However, ruthenium is both expensive and scarce. Free-base porphyrin sensitizers have also been used as molecular sensitizers, but generally perform poorly unless they are highly derivatized with electron donating groups.[1–3] Very recently it was found that highly asymmetric zinc porphyrins achieved a high efficiency of >12% in TiO_2-based DSSCs.[4,5] Organic sensitizers have the advantage of being composed of abundant elements, but generally speaking the expense of the synthesis increases with the complexity of the molecule. Thus, the advantage of an organic system is at its highest when the synthesis is the most simple. Although the complexity of their fabrication renders them impractical, much can be learned from derivatized porphyrin sensitizers in the design of future organic sensitizers. For example, in contrast to the poorly functioning, non-derivatized porphyrins, porphyrins with electron donating moieties have multiple electron redox chemistry in an accessible potential range. This is related to their stronger absorption in the lower energy region of the visible spectrum. Looking forward, it would be advantageous to use a sensitizer that is simply synthesized, asymmetric, capable of multi-electron redox reactions, and has an absorption profile roughly matching that of the solar irradiance spectrum.

Phlorins are tetrapyrrole macrocycles with a porphyrinoid backbone, except one *meso*-carbon is tetrahedral. The phlorin discussed herein is shown in Scheme 5.1.

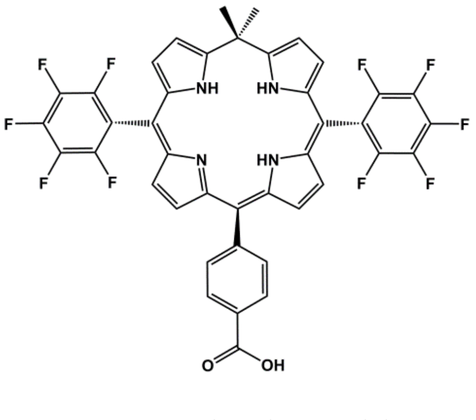

Scheme 5.1 The structure of the phlorin (5,5-dimethyl-10,20-bis(pentafluorophenyl)-15-(4-carboxyphenyl)phlorin) utilized in this work.

In the past, phlorins were a nearly synthetically inaccessible class of porphyrinoids, but in recent years a simple synthesis of phlorins has been developed[6] and expanded[7,8]. The modular nature of the newly formulated synthesis allows the *meso* substituents of these inherently asymmetric macrocycles to be varied with relative ease. Their unique structure stabilizes the phlorin to multi-electron redox reactions, and gives a favorable absorption profile, most having appreciable absorption to wavelengths of ~750 nm. Furthermore, because a wide variety of substituents are possible, the electronic characteristics of the macrocycle are highly tunable.[7]

The purpose of this work was to evaluate the potential of a phlorin as a sensitizer for mesoporous, nanocrystalline, anatase TiO_2.

5.2 Experimental

5.2.1 Materials

The following substances were used as received from the provider: acetonitrile (Burdick and Jackson, spectrophotometric grade), lithium perchlorate (Aldrich, 99.99%), titanium(IV) isopropoxide (Aldrich, 97%), nitric acid (Macron Fine Chemicals, ACS Reagent grade), polyethylene glycol bisphenol A epichlorohydrin copolymer 15,000-20,000 Da (Sigma), fluorine-doped tin oxide coated glass (Hartford Glass Company, Inc., 15

Ω/□, 2.3 mm thick), 5,5-Dimethyl-10,20-bis(pentafluorophenyl)-15-(4-carboxyphenyl)phlorin (abbrev. phlorin, used as provided by Allen Pistner).

5.2.2 Titania thin film preparation

TiO_2-anatase nanocrystallites were prepared from titanium(IV) isopropoxide using a previously described sol-gel process and stored in the dark.[9] The sols were cast as mesoporous thin films by doctor blading onto glass slides with a conductive layer of fluorine-doped tin oxide (FTO), using clear cellophane tape as a spacer (~10 μm thick). After drying in the dark for 30 minutes, the cellophane was removed and the films were sintered at 450°C under a flow of O_2 at ~1 atm. The films were then stored in an oven at ~75°C. In the case of films used in IPCE measurements, the films were treated with $TiCl_4$ in a procedure modified from the literature.[10] The films were heated at 70°C in aqueous 40 mM $TiCl_4$ solution for 30 minutes, then rinsed with water and ethanol and sintered a second time at 450°C for 30 minutes. The phlorin was anchored to the film by immersing the film in a μM CH_3CN solution of the phlorin under inert atmosphere for approximately 30 minutes. In the cases of IPCE and spectroelectrochemical measurements, the samples remained in the phlorin solution for several days to achieve high surface coverage.

5.2.3 Spectroscopic measurements

Unless otherwise noted, all measurements were recorded under argon.

5.2.3.1 *UV-visible electronic absorption spectroscopy*

Absorption spectra were measured using a Varian Cary 50 spectrophotometer. All measurements were taken at ambient temperature using 1 cm path-length cuvettes. In the case of samples on FTO, the probe beam first illuminated the glass side of the FTO|TiO_2 at a 45° angle.

5.2.3.2 *Measurement of the molar absorptivity of the phlorin on the TiO_2 surface*

The molar absorptivity of the phlorin on the TiO_2 surface was measured by immersing the film into a CH_3CN solution of the phlorin of known volume and concentration and monitoring the change in absorption spectrum. The absorption change was monitored 1) through the solution and FTO|TiO_2, and 2) through the solution and a portion of the FTO with no TiO_2. The FTO in neat CH_3CN served as the blank, and the absorption of the TiO_2 was measured and subtracted from the absorbance measurements through FTO|TiO_2. The volume of the glass excluded the solution of phlorin, so upon immersion of the glass substrate the path length of the phlorin solution was modified from the width of the cuvette

(1 cm). The thickness of the glass slide was measured using calipers, and the distance the probe beam traveled through glass was calculated assuming that the beam passed at exactly 45° to the surface of the glass. Subtracting this length from the original path length of 1 cm yielded the new path length. Argon flowed through the cuvette headspace, but the volume of the phlorin solution was kept constant by saturating the argon with CH_3CN by bubbling it through neat CH_3CN before it entered the headspace of the cuvette. The change in concentration of the phlorin solution was calculated based on the change in absorbance through the FTO (no TiO_2 film) and the measured molar extinction of the phlorin in CH_3CN solution (37900 $M^{-1}cm^{-1}$ at 418 nm). The change in concentration of the solution was converted to a change in moles of phlorin molecules in solution based on the known volume. It was assumed that all phlorin molecules no longer in solution were adsorbed to the TiO_2 thin film. The geometrical surface area of the TiO_2 film was measured using calipers, allowing a surface coverage (Γ) in moles/cm^2 to be calculated. Using the absorbance change through FTO|TiO_2 and subtracting the contribution of the change in solution absorbance gave the absorbance of phlorin molecules on the TiO_2 surface (TiO_2|phlorin). The molar absorptivity (ε) of TiO_2|phlorin was calculated using the modified Beer's Law (Equation 5.1), where A is the absorbance and 1000 is a conversion factor.

$$\varepsilon = \frac{A}{1000 \cdot \Gamma} \tag{5.1}$$

The determination of molar absorptivity on TiO_2 was repeated in the presence of a 10 fold excess chenodeoxycholic acid to test for aggregation effects on the absorption profile of the phlorin.

5.2.3.3 ***Nanosecond transient absorption spectroscopy***

Measurements were made in an arrangement previously described in the literature.[11] The excitation source was a pulsed, Q-switched Nd:YAG (Quantel USA (BigSky) Brilliant B) with a full width at half maximum of 5-6 ns and a beam diameter of approximately 10 mm. In all experiments, the laser excitation occurred at 1 Hz and was incident at 45° through the glass side of the sample. The excitation fluence was measured using a thermopile power meter (Molectron). The excitation wavelength was tuned using the appropriate non-linear optics to achieve a 532 nm beam, followed by Raman shifting using a pressurized tube of hydrogen gas (400 psi) and the appropriate filters to isolate the 683 nm Stokes-shifted beam. The probe beam, a 150 W Xenon lamp (Applied Photophysics) pulsed at 1 Hz, was also incident on the glass side of the sample at 45° and arranged perpendicular to the excitation beam. The bean was directed to a monochromator (Spex) which was optically coupled to a photomultiplier tube (R928 Hammatsu). The transient signal was recorded by an optically triggered oscilloscope with 2.5 ns resolution (LeCroy 9450). The overall instrument response time was ~10 ns. The transient absorption data was fit to the Kohlrausch-Williams-Watts

(KWW)[12–14] stretched exponential function (Equation 5.4) using the Levenburg-Marquardt iteration method in Origin 8.1. Average lifetime values, τ, were calculated through the relationship in Equation 5.5, which gives the first moment of the underlying Lèvy distribution.[15] Equation 5.6 was used in order to calculate the regeneration yield, Φ_{reg}, of the TiO_2|phlorin in the presence of $[Co(bpy)_3][ClO_4]_2$.

5.2.3.4 ***Incident photon conversion efficiency (IPCE)***

The FTO|TiO_2|phlorin was illuminated through the FTO side with monochromatic light in the presence of either $Co(bpy)_3^{3+/2+}$ or I^-/I_3^- mediator with a platinum wire counter electrode. The electrolyte solution was acetonitrile with 200 mM $LiClO_4$, 220 mM $[Co(II)(bpy)_3][ClO_4]$, and 20 mM $NOBF_4$ or 200 mM LiI with 20 mM I_2. The photocurrent density (J_{sc}, mA/cm^2) at each excitation wavelength was recorded using a CEP-2000 system (Bunkoh-Keiki Co. Ltd.). The IPCE was calculated with Equation 5.2, where P_0 is the incident radiative flux in W/m^2, q is the elementary charge, and λ is the excitation wavelength in nm.

$$IPCE(\lambda) = 1240 \cdot \frac{J_{sc}}{q\lambda P_0} \qquad 5.2$$

5.2.3.5 ***Photoluminescence***

The photoluminescence of all samples was recorded using a Spex Fluorolog spectrophotometer with a 450 W Xenon lamp as the excitation beam. In the case of solution samples, the photoluminescence was detected at a right angle to the excitation beam. In the case of FTO|TiO_2|phlorin samples, the photoluminescence was detected in a front-facing manner to decrease the detection of scattered excitation light. The quantum yield of the phlorin was measured with reference to $Os(bpy)_3^{2+}$ in CH_3CN ($\Phi = 0.005$) using the optically dilute method.[16,17]

5.2.4 Spectroelectrochemistry and electrochemistry

All experiments were performed in 300 mM $LiClO_4$ CH_3CN electrolyte. Electrochemical experiments were conducted using BAS CV50W potentiostat in a standard 3-electrode cell. For measurements of the phlorin in solution, a Pt disk working electrode was employed, whereas for measurements of the phlorin anchored to TiO_2 the working electrode was FTO|TiO_2. In all cases the counter electrode was either a platinum gauze or disk, and the non-aqueous reference electrode (Bioanalytical Scientific Instruments, Inc.) was Ag/AgCl in 300 mM $LiClO_4$ CH_3CN. In the case of the measurement of the first oxidation of the phlorin in CH_3CN solution, a Pt microelectrode was employed. The reference electrode was calibrated with ferrocenium/ferrocene (Fc^+/Fc) before and after experiments. The potential was converted to NHE using E^0 = 630 mV *vs.* NHE for Fc^+/Fc in CH_3CN.[18] The scan rate was 100 mV/s for all cyclic voltammetry experiments, and 20 mV/s with 50 mV pulses for all differential pulse voltammetry experiments.

Spectroelectrochemical experiments were conducted in a standard 3-electrode cell as described for electrochemical measurements using FTO|TiO_2 as the working electrode. Experiments proceeded by applying a potential to the FTO|TiO_2 electrode and simultaneously monitoring the UV-visible absorbance. Typically the potential was stepped in 25, 50, or 100 mV increments. Each potential was held until the change in absorption was complete, at minimum 3 minutes. The spectrum of each species present was used in a standard addition global fit of the sample spectrum at each potential using a Least Squares analysis in Wolfram Mathematica 9. This analysis yielded a fractional abundance of each species (x) at each potential. This data was fit in Origin 8 using Equation 5.3, which is the Nernst relationship between fractional abundance, applied potential, and reduction potential.

5.3 Results

After immersing optically transparent TiO_2 thin films in a CH_3CN solution of the phlorin, the films became colored (green). Upon rinsing and immersion of the films in neat CH_3CN, no loss in film coloration was observed. The surface coverage ranged from 0.8-7.7 x 10^{-8} moles/cm^2, depending on the reaction time and the solution concentration. Figure

5.1A shows the molar absorptivity spectra of the phlorin in CH_3CN solution (red) and anchored to a TiO_2 thin film and immersed in CH_3CN (black, abbrev. TiO_2|phlorin). The normalized fluorescence of the phlorin in CH_3CN (blue) is also shown. The fluorescence quantum yield in solution was calculated to be $\Phi = 0.001$ using the dilution method, which is described in the literature.[16,17] In solution, there were two Soret-type peaks of similar molar absorptivity at 417 and 436 nm, whereas TiO_2|phlorin displayed bathochromically shifted peaks centered at 421 and 440 nm. In addition, the molar absorptivity of the Soret-type peaks increased upon anchoring to TiO_2, with the peak at 440 nm intensifying more than the peak at 421 nm. In the 550-800 nm range, the Q-type bands were broadened and shifted from 663 nm in solution to 667 nm on TiO_2. The absorptivity increased in the long wavelength region, $\lambda > 725$ nm. Integration of the area under each spectrum between 355-1000 nm indicated a 30% increase in molar absorptivity upon anchoring to TiO_2. By eye, the CH_3CN solution was emerald green, and the TiO_2|phlorin was a brownish green color. When a ~10 fold excess of chenodeoxycholic acid was present in the phlorin dying solution, TiO_2|phlorin absorption spectra were similar to that measured without chenodeoxycholic acid, but the molar absorptivity was ~2 times as intense (see Figure 5.2). Furthermore, the Soret-type bands were not intensified as much, in proportion to the Q-type bands, as they were in the case where chenodeoxycholic acid was absent. There was also a small shoulder on the lower energy side of the Q-type bands, which was not present without chenodeoxycholic acid.

Figure 5.1B shows the effect of the addition of $LiClO_4$ to the CH_3CN solvent surrounding the TiO_2|phlorin film. When Li^+ was added, the Soret-type and Q-type peaks shifted bathochromically with maintenance of isosbestic points. The change in the maximum of the Soret-type peak was ~1100 cm^{-1}, and the change in the maximum of the Q-type peak was ~1900 cm^{-1}. The inset of Figure 5.1B shows the change in absorbance at 466 nm as a function of added $LiClO_4$ concentration with an overlaid fit to the Langmuir equation. For this data, the equilibrium constant abstracted from the fit was 32(±4) M^{-1}; however, the magnitude of the change in the absorbance of the TiO_2|phlorin was variable from sample to sample. The change in absorbance could be reversed by applying a small forward bias, as can be seen in Figure 5.6. Control experiments showed that there was no significant change in the absorbance spectrum of the phlorin in CH_3CN solution upon addition of 300 mM $LiClO_4$.

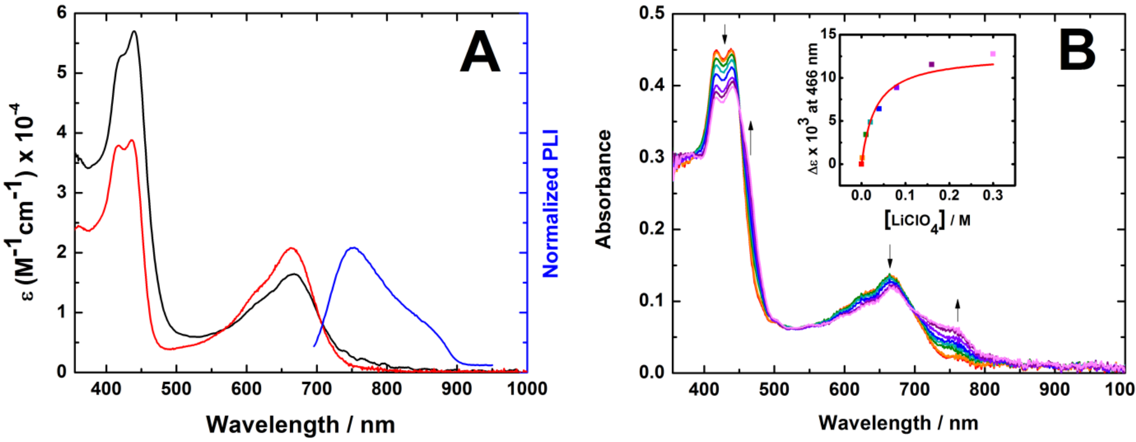

Figure 5.1 A) The molar absorptivity of the phlorin in CH_3CN solution (red), and anchored to the TiO_2 surface (abbrev. TiO_2|phlorin) and immersed in CH_3CN (black). B) The absorbance spectra of TiO_2|phlorin immersed in CH_3CN with varied amounts of added $LiClO_4$. Arrows indicate the direction of change with increasing added $LiClO_4$. The inset shows the change in absorbance at 466 nm as a function of added [$LiClO_4$]. The overlaid fit (red) indicates an equilibrium constant of 32(±4) M^{-1}.

The effect of aggregation on the molar absorptivity of the phlorin anchored to TiO_2 was evaluated by repeating the experiment described above in the presence of tenfold excess chenodeoxycholic acid, which is believed to prevent aggregation. The molar absorptivity (Figure 5.2) was roughly double that without the found without the aggregation blocker. There was also a small shoulder in the low energy region of the Q-type bands, which resembles the effect of $LiClO_4$ addition. The origin of this shoulder is unknown, and could be the product of interactions with the aggregation blocker, which has many alcohol groups on one side.

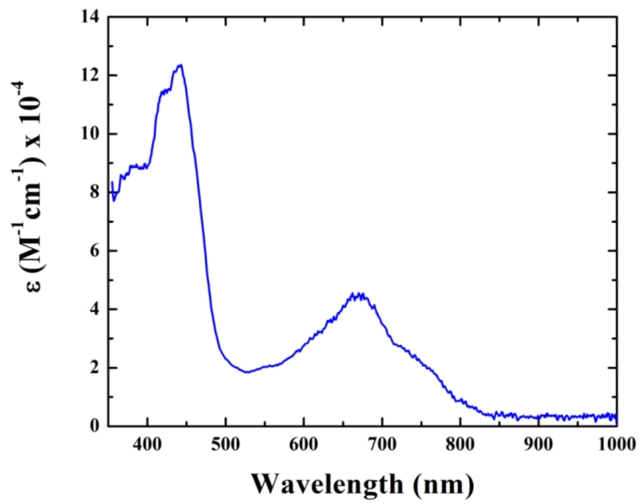

Figure 5.2 The molar absorptivity (ε) of the phlorin adsorbed onto TiO_2 in the presence of 10 fold excess chenodeoxycholic acid.

Cyclic voltammetry experiments in 300 mM $LiClO_4$ CH_3CN revealed a quasi-reversible oxidation of the phlorin in solution at 720 mV *vs.* NHE, Figure 5.3.

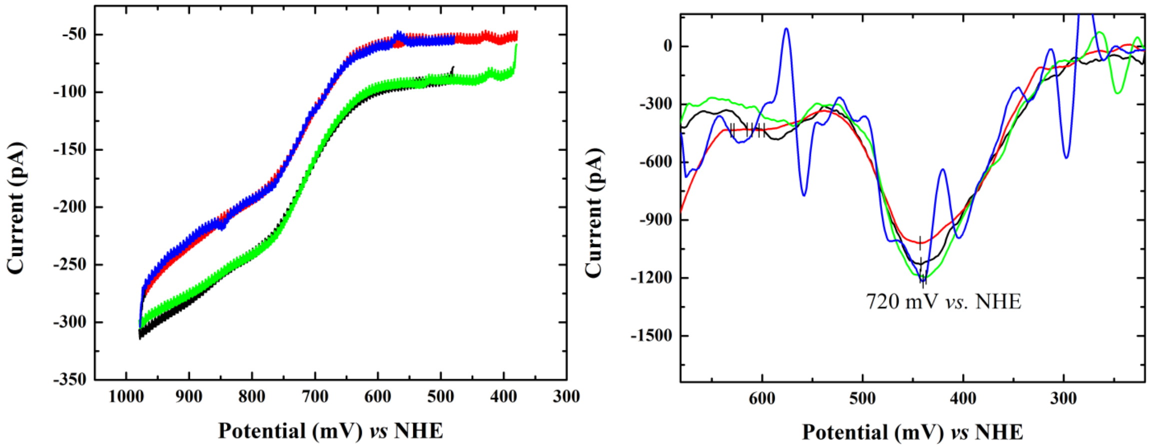

Figure 5.3 A) Cyclic voltammograms of the phlorin in 300 mM $LiClO_4$ CH_3CN solution taken with a platinum microelectrode at 100 mV/s. B) The smoothed derivative of the data in part A of this figure, which allows the determination of peak current at 720 mV *vs*. NHE.

Spectroelectrochemical experiments were employed to determine the reduction potential of the first oxidation of TiO_2|phlorin. Figure 5.4 shows the absorption spectra in the Q-type region at the indicated applied potentials. The surface coverage (5.6×10^{-8} moles/cm^2) was such that the absorbance in the Soret-type region was greater than 2. These spectra were used to calculate the fractional amount (x) of each species at each applied potential, shown in the inset of Figure 5.4. The fits of these data to Equation 5.3 are overlaid.

$$\chi = \frac{1}{1 + 10^{\frac{E - E_{1/2}}{i \cdot 59}}} \qquad 5.3$$

The sigmoidal fits yielded an $E_{1/2}$ of TiO_2|phlorin$^{+/0}$ equal to 640 mV *vs.* NHE, with an ideality factor of i = 1.06. The $E_{1/2}$ obtained using cyclic voltammetry and differential pulse voltammetry (Figure 5.5 and Figure 5.3) were within error of the spectroelectrochemical result. This data indicates a -80 mV shift from the solution value.

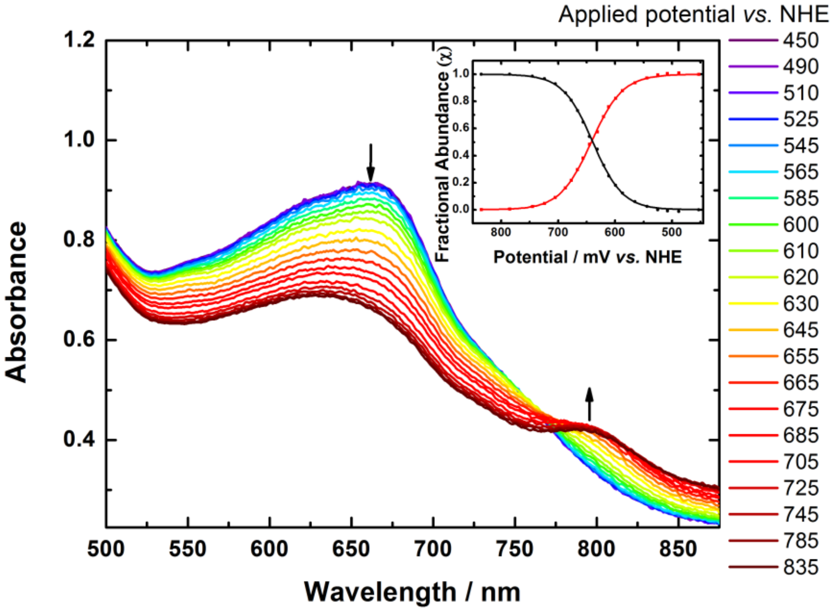

Figure 5.4 The absorption of TiO$_2$|phlorin in 300 mM LiClO$_4$ CH$_3$CN at the indicated applied potentials. Arrows indicate the direction of changes associated with oxidation. Inset: The fractional abundance of the TiO$_2$|phlorin (red) and TiO$_2$|phlorin$^+$ (black) at each potential. An average $E_{½}$ = 640 mV and i = 1.06 were abstracted from the fits to Equation 5.3 (overlaid).

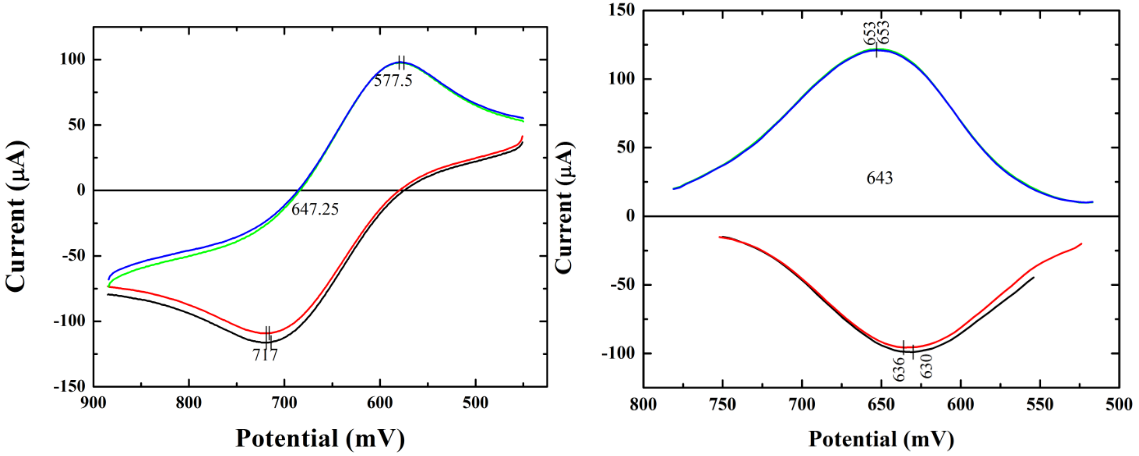

Figure 5.5 A) Cyclic voltammograms of the TiO$_2$|phlorin in 300 mM LiClO$_4$ CH$_3$CN at a scan rate of 100 mV/s. B) Differential pulse voltammograms of the TiO$_2$|phlorin in 300 mM LiClO$_4$ CH$_3$CN at a scan rate of 20 mV/s with 50 mV pulses.

Figure 5.6 shows the absorbance spectra of TiO_2|phlorin at the indicated applied potentials (A), as well as the unique absorption features assigned to TiO_2|phlorin, the neutral phlorin with electrons in the titania (abbrev. $TiO_2(e^-)$|phlorin), and the reduced phlorin with electrons in the titania (abbrev. $TiO_2(e^-)$|phlorin$^-$) (B).

The colors of the spectral data reflect the color of the sample. Global fitting of the data in Figure 5.6A using the spectra in Figure 5.6B yielded a plot of the fractional abundance of each species at every potential considered (Figure 5.6B inset). The sigmoidal fit of the fraction of $TiO_2(e^-)$|phlorin$^-$ (Equation 5.3) yielded an ideality factor of $i = 2.4$ and $E_{½} = -120$ mV, which was a +330 mV shift from the solution value of -450 mV *vs.* NHE (Figure 5.7).

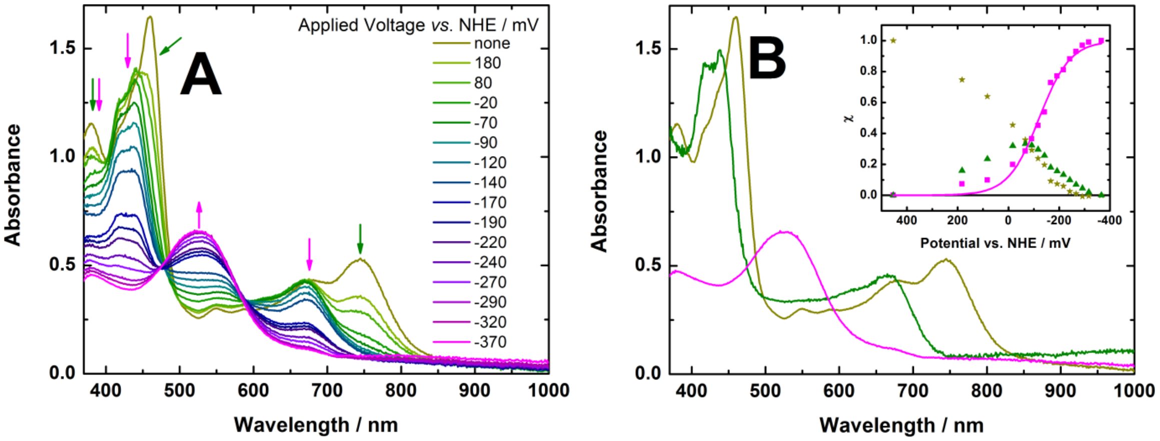

Figure 5.6 A) The absorption of TiO$_2$|phlorin in 300 mM LiClO$_4$ CH$_3$CN at the indicated applied potentials. The green arrows indicate the changes associated with an initial process, and the magenta arrows indicate the changes associated with the reduction of the phlorin. B) The absorption spectra of the initial species (olive), the intermediate species (green), and the reduced species (magenta) that were used in global modeling of spectra in A to determine the fractional abundance (x) of each species at every potential. Inset: The x of initial TiO$_2$|phlorin + LiClO$_4$ (olive), the intermediate TiO$_2$(e$^-$)|phlorin + LiClO$_4$ (green), and TiO$_2$(e$^-$)|phlorin$^-$ (magenta). The sigmoidal fit of the data yielded E$_{1/2}$ (phlorin$^{0/-}$) of -120 mV *vs.* NHE and an ideality factor of 2.4.

In order to characterize the photo-induced electron transfer reactions of this phlorin, transient absorption experiments were performed.

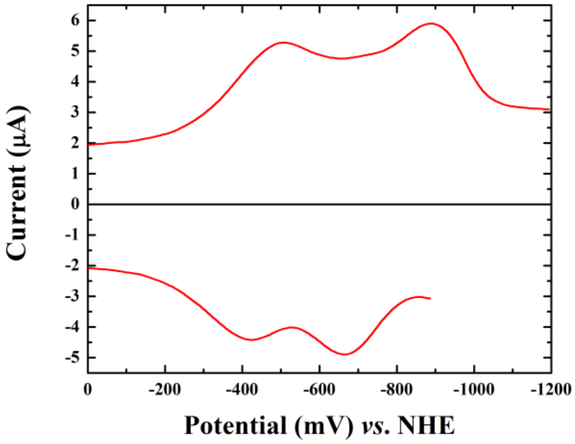

Figure 5.7 The differential pulse voltammogram of the phlorin in 300 mM $LiClO_4$ CH_3CN at a scan rate of 20 mV/s with 50 mV pulses.

Figure 5.8A shows the change in absorbance at various time points after pulsed 683 nm laser excitation of the TiO_2|phlorin in 300 mM $LiClO_4$ CH_3CN.

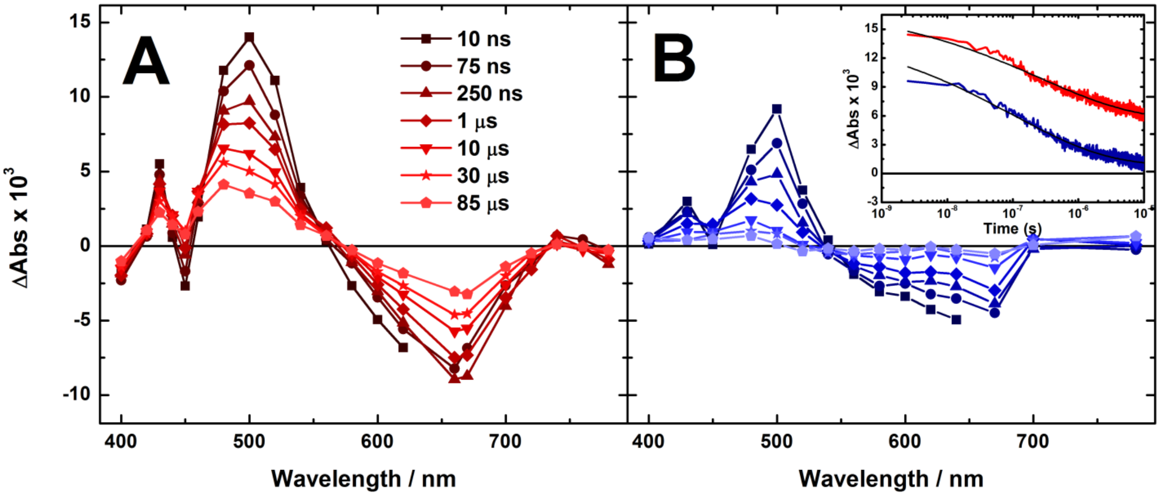

Figure 5.8 The absorption change of TiO_2|phlorin at the indicated times after pulsed 683 nm light excitation with no applied voltage (A) and with an applied voltage of -200 mV vs. NHE (B). Inset: transient absorption change at 500 nm with no applied voltage (red) and with -200 mV applied voltage (blue). Overlaid are fits to the KWW function (Equation 5.4), yielding rate constants of 3.8×10^6 and 1×10^7 s^{-1}, respectively.

There was a bleach in the Q-type region, and a growth centered at 500 nm. To ensure that this change in absorption was representative of the charge separated $TiO_2(e-)$|phlorin$^+$ state, transient absorption experiments were performed under the same conditions except with an applied voltage of -200 mV *vs.* NHE (Figure 5.8B). The change in absorbance was similar in shape, with a bleach in the Q-type region and a growth centered at 500 nm. In contrast, the growth at 510 nm and the bleach at 660 nm were proportionally smaller in magnitude than in the spectra without an applied potential. Furthermore, the amplitudes of the absorbance change were decreased by ~ 40% compared to the data measured without an applied potential.

The kinetics under all conditions were wavelength-dependent, and some wavelengths exhibited complicated behavior. The inset of Figure 5.8B shows the absorbance change at the peak of the growth (500 nm) for with (blue) and without (red) a negative applied potential. Fits of to the Kohlrausch Williams-Watts (KWW) function (Equation 5.4) are overlaid.[12–14]

$$\Delta A = A_0 e^{\left(\frac{-t}{\tau_0}\right)^{\beta}} \tag{5.4}$$

In the KWW function, ΔA is the change in absorbance at time t, A_0 is the change in absorbance at t = 0, τ_0 is a time constant, and β is a number from 0 to 1 that reflects the underlying Lèvy distribution of time constants. The average time constant, τ, was calculated from Equation 5.5, which gives the first moment of the Lèvy distribution.[15]

$$\tau = \frac{\tau_0}{\beta} \Gamma\left(\frac{1}{\beta}\right) \tag{5.5}$$

The average rate constant $k = \tau^{-1}$. The rate constant calculated from the change in absorbance at 500 nm increased from 3.8×10^6 to 1×10^7 s^{-1} upon the application of a -200 mV bias. The absorption spectra of the sample after pulsed laser excitation exhibited a slight decrease in absorbance.

The sensitizing capability of the phlorin was evaluated by measuring the incident photon-to-current conversion efficiency (IPCE). Figure 5.9 shows the IPCE spectra measured from 390 to 730 nm with $Co(bpy)_3^{3+/2+}$ or I^-

$/I_3^-$ redox mediators (A) and from 500 to 1000 nm with Co(bpy) $_3^{3+/2+}$ as the mediator. The IPCE was significantly higher with the Co(bpy)$_3^{3+/2+}$ redox mediator relative to I^-/I_3^- (Figure 5.9A). Additionally, the phlorin was capable of sensitizing TiO_2 with photons of energy as low as 800 nm (Figure 5.9B). Additionally, the photocurrent action spectra were taken with the cell exposed to the atmosphere, unlike all other experiments. Absorbance spectra of the TiO_2|phlorin sample measured before and after IPCE measurements revealed a decrease in the absorbance spectrum after IPCE measurements.

Figure 5.10 shows the normalized absorption change monitored at 500 nm after pulsed, 683 nm laser excitation of a sample of TiO_2|phlorin immersed in 300 mM $LiClO_4$ CH_3CN in the presence and absence of 50 mM Co(bpy)$_3^{2+}$. Overlaid on the data are the KWW fits (Equation 5.4) from which the rate constant of the decay of the transient species was abstracted. The rate constant was increased from 2.0 x 10^4 to 1.0 x 10^5 s^{-1} upon the addition of 50 mM Co(bpy)$_3^{2+}$. Based on the kinetic data, a regeneration yield of $\Phi_{reg} = 0.21$ was calculated from Equation 5.6, where k_{reg} is the rate constant in the presence of a donor D, and k_{cr} is the rate constant of charge recombination in the absence of the donor, [Co(bpy)$_3$][ClO_4]$_2$.

$$\Phi_{reg} = \frac{k_{reg}[D]}{k_{cr} + k_{reg}[D]} \qquad 5.6$$

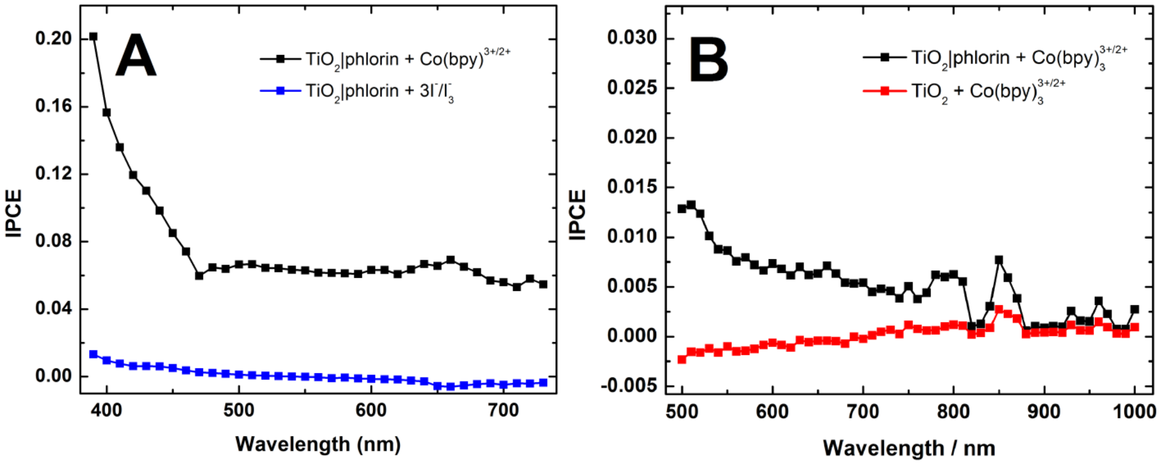

Figure 5.9 A) The IPCE (incident photon conversion efficiency) of the TiO_2|phlorin system A) with Co(bpy) $_3^{3+/2+}$ (red) or I^-/I_3^- (black) as the redox mediator. B) The IPCE of bare TiO_2 (black) and of TiO_2|phlorin (red) in the red and near-infrared regions of the electromagnetic spectrum with Co(bpy) $_3^{3+/2+}$ as the redox mediator.

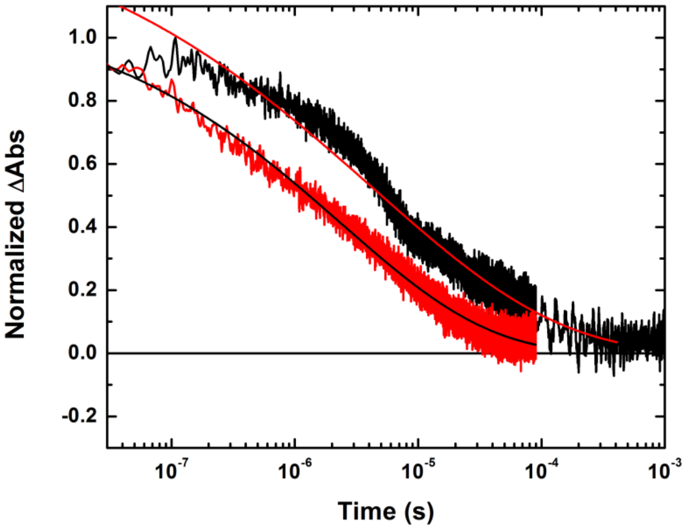

Figure 5.10 The transient change in absorbance of TiO_2|phlorin at 500 nm after pulsed 683 nm light excitation in 300 mM $LiClO_4$ acetonitrile (black), and the same sample with 50 mM $Co(bpy)_3(ClO_4)_2$ (red). Overlaid are fits to the KWW function (Equation 5.4), from which lifetimes of 4.9 and 1.0 x 10^{-5} s were abstracted, respectively.

5.4 Discussion

To our knowledge, this is the first reported measurement of the molar absorptivity of a compound bound to TiO_2. It is a common practice to assume that the molar absorptivity of a compound anchored to TiO_2 is approximately the same as it is in solution. It is likely that this is a sound assumption for many molecules. The cause of the change in molar absorptivity observed in the case of the phlorin is not clear. It is possible that the change arises from the dipole of the phlorin, or a change in the conformation of the phlorin from saddle-shaped in solution to more flattened when anchored to TiO_2. The further change in the absorption spectrum of the TiO_2|phlorin in the presence of a lithium salt may be due to the Li^+ screening of the electric field emanating from the TiO_2 particles. It has been observed that lithium salts cause spectral shifts in compounds anchored to TiO_2, and the phenomenon has been referred to as a Stark effect due to the similarity it bears to the changes in absorption observed in Stark spectroscopy.[19–26] The bathochromic shifts reported for ruthenium polypyridyl molecules[19–21,27] is on the order of 50-200 cm^{-1}, and 285-870 cm^{-1} for triphenylamine-based sensitizers.[10,28] The spectral shift on the order of 10^3 cm^{-1} observed for the phlorin is, to our knowledge, the largest reported bathochromic shift due to charge screening by lithium salts. However, these large Li^+-induced shifts may be a fairly common phenomenon that has gone unreported, especially for organic sensitizers with dipoles aligned with the local electric field emanating from the TiO_2 particles. Molecules of the phlorin family are known to bind ions,[8] so it is possible that the enhancement of the bathochromic shift is due to a specific interaction between the phlorin and Li^+. However, there was no evidence for a specific interaction, given that 1) Li^+ causes no change in the UV-visible absorbance of the phlorin in CH_3CN solution, 2) the measured adduct formation constant of 32 M^{-1} is consistent with previous measurements of the binding of Li^+ to sensitized TiO_2 in CH_3CN[19,20] and other solvents,[29] and 3) the effect of Li^+ was reversed by a slight negative applied bias (Figure 5.6). If a specific interaction with the phlorin that might cause larger shifts than expected for screening exists, it must have an insignificant driving force compared to the binding of Li^+ to TiO_2.

Spectroelectrochemical oxidation of the phlorin on TiO_2 required very high surface coverage in order to allow holes to hop quickly from the FTO to all of the $TiO_2|$phlorins. Because of the high absorptivity of the phlorin, only the Q-type band could be used for analysis. The -80 mV shift from phlorin in solution to $TiO_2|$phlorin is within shifts reported for other sensitizers. The near-Nernstian behavior of this redox couple is in stark contrast to the ideality factor of 2.4 necessary to fit the $TiO_2|$phlorin$^{0/-}$. Furthermore, the spectroelectrochemical reduction of $TiO_2|$phlorin yielded a strongly shifted $E_{1/2}$ = -120 mV for the first reduction of the phlorin, in contrast to the solution value of -450 mV. The origin of this unprecedentedly (?) large 330 mV shift is unclear, but it may be that Li^+ brought into close proximity by its attraction to the TiO_2 surface stabilizes the negative charge of the phlorin$^-$. The ideality factor of 2.4 is large, but larger have been reported.[27,30]

The decrease in amplitude of the change in absorbance of TiO_2|phlorin after pulsed laser excitation and decrease in lifetime brought on by the application of a negative bias was taken as evidence that the transient spectrum at least in part due to the charge separated $TiO_2(e^-)$|phlorin$^+$ (Figure 5.8). As ~75% of the phlorin would have been reduced at -200 mV (Figure 5.6), it is possible that the proportionally small growth at 520 nm was due to a decrease in the number of $TiO_2(e^-)$|phlorin$^-$, which had higher molar extinction at 520 nm than the TiO_2|phlorin.

The increased IPCE with a cobalt mediator *vs.* iodide mediator can be explained in thermodynamic terms. The reduction potential of the first oxidation of the phlorin is more negative than those of typical ruthenium polypyridyl sensitizers, thus the $Co(bpy)_3^{3+/2+}$ mediator is a more potent reductant for the oxidized phlorin by virtue of having a more negative potential than I^-/I_3^-.

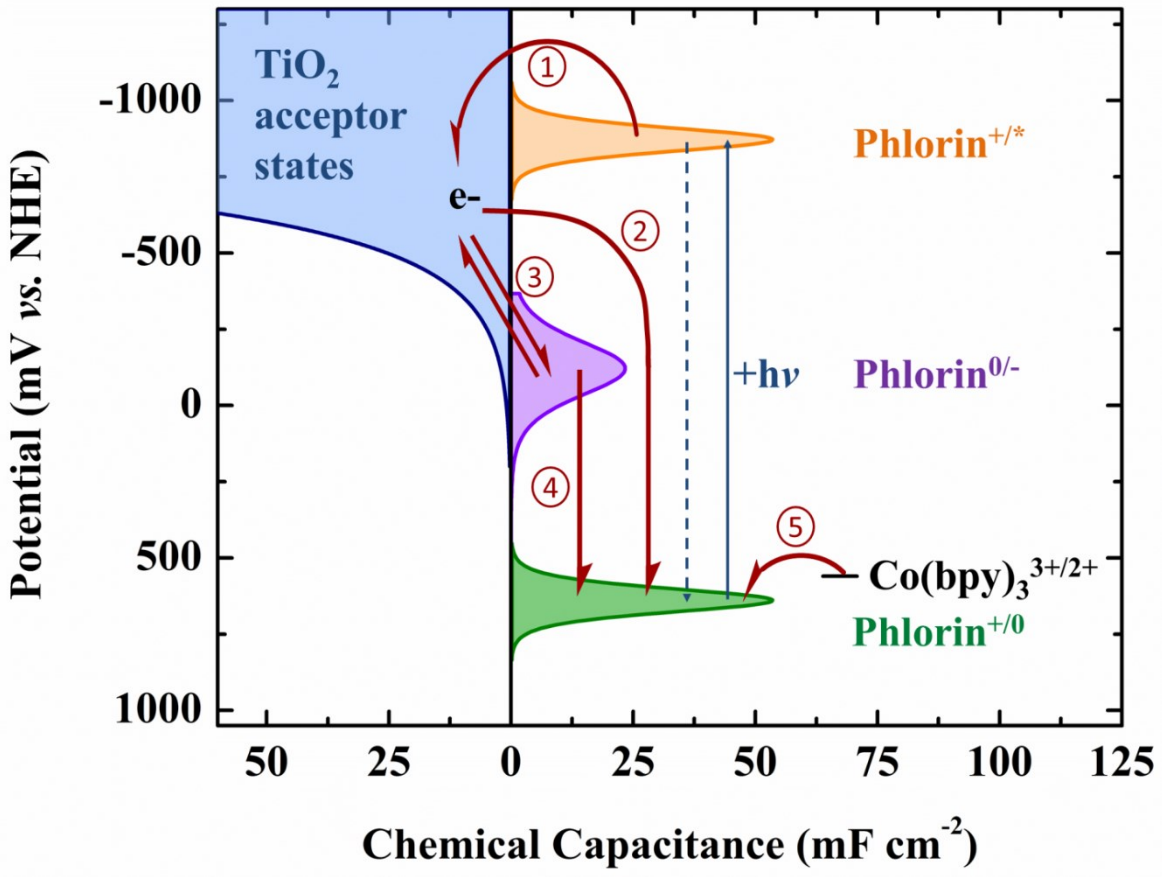

Figure 5.11 The density of states in free energy of the TiO$_2$|phlorin in 300 mM LiClO$_4$ CH$_3$CN measured in chemical capacitance as a function of potential. Red arrows indicate possible electron transfer pathways: 1) excited state electron injection, 2) recombination to the oxidized sensitizer, 3) the hypothetical equilibrium between the TiO$_2$ acceptor states and the reduced sensitizer, 4) electron transfer from reduced sensitizers to oxidized sensitizers, and 5) regeneration by a mediator in solution.

The low regeneration yield of 0.21 is consistent with the low IPCE. Interestingly, the change in absorption of TiO_2|phlorin after pulsed laser excitation became more exponential in shape in the presence of the cobalt mediator.

The spectroelectrochemical data was compiled to show the energetics of the electron transfer processes in the TiO_2|phlorin system (Figure 5.11). The favorability of the injection process (1) can be evaluated using the estimated excited state reduction potential $E^{*/+}$, the minimum energy between the ground and excited states $E_{0\text{-}0}$, as in Equation 5.7.

$$E^{*/+} = E^{0/+} - E_{0-0} \qquad 5.7$$

$E_{0\text{-}0}$ was estimated to be 709 nm = 1749 meV from the absorbance and emission spectra (Figure 5.1A). Combined with the measured TiO_2|phlorin$^{0/+}$ reduction potential (640 mV *vs.* NHE, Figure 5.4), the excited state reduction potential was calculated to be approximately -1100 mV *vs.* NHE. Thus, the injection from the excited state is expected to be thermodynamically favorable. Pathway 2 is the interfacial electron recombination reaction shown in Equation 5.8.

$$TiO_2(e^-)|phlorin^+ \rightarrow TiO_2|phlorin \qquad 5.8$$

This recombination pathway is expected to be in or near the Marcus inverted region, as the conduction band of TiO_2 is at approximately -0.5 V *vs.* NHE, yielding ΔE ≈ 1.14 V. Pathway 3 is drawn as an equilibrium because the TiO_2|phlorin$^{0/-}$ reduction potential was measured to be -120 mV such that the exchange with the lower energy acceptors of TiO_2 had a very small free energy change. Pathway 4 represents the hypothetical electron transfer from one anchored phlorin in the -1 oxidation state to another anchored phlorin in the +1 oxidation state. Pathways 3 and 4 were not directly confirmed, but they could be partially responsible for the low IPCE and Φ_{reg} = 0.21 observed here. The regeneration pathway 5 may also contribute, as the driving force is only 90 mV with the $Co^{III/II}$ potential at ~550 mV *vs.* NHE.

5.5 Conclusions

While we found that the free-base phlorin is not a good candidate for sensitizing TiO_2 in DSSCs, metallating the phlorin might solve many of the problems by pushing the reduction potential more positive to avoid an equilibrium with the $TiO_2(e^-)$ and making the phlorin less reactive with oxygen. The phlorin may also be promising for electrochromic devices, and for catalytic reactions. In both cases, it would be of interest to also test the behavior of metallated phlorins.

5.6 References

(1) Hagfeldt, A.; Boschloo, G.; Sun, L.; Kloo, L.; Pettersson, H. Dye-Sensitized Solar Cells. *Chem. Rev.* **2010**, *110* (11), 6595–6663.

(2) Campbell, W. M.; Burrell, A. K.; Officer, D. L.; Jolley, K. W. Porphyrins as Light Harvesters in the Dye-Sensitised TiO_2 Solar Cell. *Coord. Chem. Rev.* **2004**, *248* (13–14), 1363–1379.

(3) Eric Wei-Guang Diau; Lu-Lin Li. Porphyrin-Sensitized Solar Cells. In *Handbook of Porphyrin Science (Volume 28)*; Handbook of Porphyrin Science; World Scientific Publishing Company, 2013; Vol. Volume 28, pp 279–317.

(4) Yella, A.; Lee, H.-W.; Tsao, H. N.; Yi, C.; Chandiran, A. K.; Nazeeruddin, M. K.; Diau, E. W.-G.; Yeh, C.-Y.; Zakeeruddin, S. M.; Grätzel, M. Porphyrin-Sensitized Solar Cells with Cobalt (II/III)–Based Redox Electrolyte Exceed 12 Percent Efficiency. *Science* **2011**, *334* (6056), 629–634.

(5) Yella, A.; Mai, C.-L.; Zakeeruddin, S. M.; Chang, S.-N.; Hsieh, C.-H.; Yeh, C.-Y.; Grätzel, M. Molecular Engineering of Push-Pull Porphyrin Dyes for Highly Efficient Dye-Sensitized Solar Cells: The Role of Benzene Spacers. *Angew. Chem. Int. Ed.* **2014**, *53* (11), 2973–2977.

(6) Hong, S.-J.; Ka, J.-W.; Won, D.-H.; Lee, C.-H. Novel Synthesis of Phlorin Derivatives and Their Anion Binding Properties. *Bull. Korean Chem. Soc.* **2003**, *24* (5), 661–663.

(7) Pistner, A. J.; Lutterman, D. A.; Ghidiu, M. J.; Ma, Y.-Z.; Rosenthal, J. Synthesis, Electrochemistry, and Photophysics of a Family of Phlorin Macrocycles That Display Cooperative Fluoride Binding. *J. Am. Chem. Soc.* **2013**, *135* (17), 6601–6607.

(8) Pistner, A. J.; Yap, G. P. A.; Rosenthal, J. A Tetrapyrrole Macrocycle Displaying a Multielectron Redox Chemistry and Tunable Absorbance Profile. *J. Phys. Chem. C* **2012**, *116* (32), 16918–16924.

(9) Heimer, T. A.; D'Arcangelis, S. T.; Farzad, F.; Stipkala, J. M.; Meyer, G. J. An Acetylacetonate-Based Semiconductor−Sensitizer Linkage. *Inorg. Chem.* **1996**, *35* (18), 5319–5324.

(10) Teng, C.; Yang, X.; Li, S.; Cheng, M.; Hagfeldt, A.; Wu, L.; Sun, L. Tuning the HOMO Energy Levels of Organic Dyes for Dye-Sensitized Solar Cells Based on Br^-/Br^{3-} Electrolytes. *Chem. – Eur. J.* **2010**, *16* (44), 13127–13138.

(11) Argazzi, R.; Bignozzi, C. A.; Heimer, T. A.; Castellano, F. N.; Meyer, G. J. Enhanced Spectral Sensitivity from Ruthenium(II) Polypyridyl Based Photovoltaic Devices. *Inorg. Chem.* **1994**, *33* (25), 5741–5749.

(12) Scher, H.; Montroll, E. W. Anomalous Transit-Time Dispersion in Amorphous Solids. *Phys. Rev. B* **1975**, *12* (6), 2455–2477.

(13) Kohlrausch, R. Theorie Des Elektrischen Rückstandes in Der Leidener Flasche. *Ann. Phys. Chem. Leipz.* **1854**, *91*, 56–82.

(14) Williams, G.; Watts, D. C. Non-Symmetrical Dielectric Relaxation Behaviour Arising from a Simple Empirical Decay Function. *Trans. Faraday Soc.* **1970**, *66* (0), 80–85.

(15) Lindsey, C. P.; Patterson, G. D. Detailed Comparison of the Williams–Watts and Cole–Davidson Functions. *J. Chem. Phys.* **1980**, *73* (7), 3348.

(16) Kober, E. M.; Caspar, J. V.; Lumpkin, R. S.; Meyer, T. J. Application of the Energy Gap Law to Excited-State Decay of Osmium(II)-Polypyridine Complexes: Calculation of Relative Nonradiative Decay Rates from Emission Spectral Profiles. *J. Phys. Chem.* **1986**, *90* (16), 3722–3734.

(17) Crosby, G. A.; Demas, J. N. Measurement of Photoluminescence Quantum Yields. Review. *J. Phys. Chem.* **1971**, *75* (8), 991–1024.

(18) Pavlishchuk, V. V.; Addison, A. W. Conversion Constants for Redox Potentials Measured versus Different Reference Electrodes in Acetonitrile Solutions at 25°C. *Inorganica Chim. Acta* **2000**, *298* (1), 97–102.

(19) Ardo, S.; Sun, Y.; Staniszewski, A.; Castellano, F. N.; Meyer, G. J. Stark Effects after Excited-State Interfacial Electron Transfer at Sensitized TiO_2 Nanocrystallites. *J. Am. Chem. Soc.* **2010**, *132* (19), 6696–6709.

(20) Rowley, J. G.; Ardo, S.; Sun, Y.; Castellano, F. N.; Meyer, G. J. Charge Recombination to Oxidized Iodide in Dye-Sensitized Solar Cells. *J. Phys. Chem. C* **2011**, *115* (41), 20316–20325.

(21) Staniszewski, A.; Ardo, S.; Sun, Y.; Castellano, F. N.; Meyer, G. J. Slow Cation Transfer Follows Sensitizer Regeneration at Anatase TiO_2 Interfaces. *J. Am. Chem. Soc.* **2008**, *130* (35), 11586–11587.

(22) Cappel, U. B.; Feldt, S. M.; Schöneboom, J.; Hagfeldt, A.; Boschloo, G. The Influence of Local Electric Fields on Photoinduced Absorption in Dye-Sensitized Solar Cells. *J. Am. Chem. Soc.* **2010**, *132* (26), 9096–9101.

(23) Krawczyk, S.; Zdyb, A. Electronic Excited States of Carotenoid Dyes Adsorbed on TiO_2. *J. Phys. Chem. C* **2011**, *115* (45), 22328–22335.

(24) Sarhangi, O. (Setare) M.; Hashemianzadeh, S. M.; Waskasi, M. M.; Harzandi, A. P. A High-Light-Harvesting-Efficiency of NKX-2593 and NKX-2883 Coumarin Dyes in a Local Electric Field: Can a Local Electric Field Enhance Dye Sensitizer Solar Cells Efficiently? *J. Photochem. Photobiol. Chem.* **2011**, *225* (1), 95–105.

(25) Meister, M.; Baumeier, B.; Pschirer, N.; Sens, R.; Bruder, I.; Laquai, F.; Andrienko, D.; Howard, I. A. Observing Charge Dynamics in Surface Reactions by Time-Resolved Stark Effects. *J. Phys. Chem. C* **2013**, *117* (18), 9171–9177.

(26) Burdziński, G.; Karolczak, J.; Ziółek, M. Dynamics of Local Stark Effect Observed for a Complete D149 Dye-Sensitized Solar Cell. *Phys. Chem. Chem. Phys.* **2013**, *15* (11), 3889–3896.

(27) Johansson, P. G.; Kopecky, A.; Galoppini, E.; Meyer, G. J. Distance Dependent Electron Transfer at TiO_2 Interfaces Sensitized with

Phenylene Ethynylene Bridged Ru^{II}–Isothiocyanate Compounds. *J. Am. Chem. Soc.* **2013**, *135* (22), 8331–8341.

(28) Robson, K. C. D.; Hu, K.; Meyer, G. J.; Berlinguette, C. P. Atomic Level Resolution of Dye Regeneration in the Dye-Sensitized Solar Cell. *J. Am. Chem. Soc.* **2013**, *135* (5), 1961–1971.

(29) Song, W.; Luo, H.; Hanson, K.; Concepcion, J. J.; Brennaman, M. K.; Meyer, T. J. Visualization of Cation Diffusion at the TiO_2 Interface in Dye Sensitized Photoelectrosynthesis Cells (DSPEC). *Energy Environ. Sci.* **2013**, *6* (4), 1240–1248.

(30) Abrahamsson, M.; Johansson, P. G.; Ardo, S.; Kopecky, A.; Galoppini, E.; Meyer, G. J. Decreased Interfacial Charge Recombination Rate Constants with N3-Type Sensitizers. *J. Phys. Chem. Lett.* **2010**, *1* (11), 1725–1728.

Biography

Erinn Brigham was born on March 5th, 1989 in Nürnberg, Germany. She attended Kimball Wiles Elementary for first through fourth grades, and Lawton Chiles Elementary for fifth grade. She then attended the Lyceum at Lincoln Middle School for sixth through eighth grades, and graduated from Eastside High School with an International Baccalaureate degree with specialization in the visual arts, history, and English literature.

Curriculum Vitae

ERINN BRIGHAM

Permanent: 71-17 Woodside Ave, #2d, Queens, NY 11377 | 1.352.870.4211 | erinn.brigham@gmail.edu
Institutional: 1305 Walt Whitman Road, Suite 300, Melville, NY 11747

EDUCATION

Johns Hopkins University, Baltimore, MD
Ph.D. in Chemistry **2015**
Dissertation: *Fundamental Electron Transfer Processes in Dye-Sensitized Solar Cells*
Advisor: Dr. Gerald J. Meyer

Johns Hopkins University, Baltimore, MD
M.A. in Chemistry **2013**
Advisor: Dr. Gerald J. Meyer

New College of Florida, Sarasota, FL
B.A. in Chemistry **2011**
Thesis: *TACN and Jibing Toward Synthetic Models of Oxalate Degrading Metalloenzymes*
Advisor: Dr. Suzanne E. Sherman

TEACHING EXPERIENCE

Johns Hopkins University, Baltimore, MD
Faculty – Intersession and Summer Programs
Global Energy Resources for the Future **2014**

Past, present, and future energy resources were discussed in terms of their scope and limitations. The fundamental operating principles of each energy technology were studied and policies regarding energy consumption and its environmental consequences were evaluated in political context. Topics included global warming and climate change, emissions regulations, fossil fuels, alternative energies, and energy security and productivity.

Graduate Teaching Assistant
Organic Chemistry I & II **2012 – 2013**
Advanced Inorganic Laboratory **2011**

New College of Florida, Sarasota, FL
Teaching Assistant
Structure and Reactivity in Organic Chemistry I & II **2010 – 2011**

Time Management Coach **2010**

Explorama Lodges, Iquitos, Perú
Teacher
English as a Second Language **2008**

RESEARCH EXPERIENCE

University of North Carolina at Chapel Hill, Chapel Hill, NC
Continued Dissertation Research
Graduate Research Assistant **2014 – 2015**
Advisor: Dr. Gerald J. Meyer
Continuation of dissertation research at Johns Hopkins University (described below) after Professor G. J. Meyer moved his laboratory to the University of North Carolina at Chapel Hill.

Johns Hopkins University, Baltimore, MD
Dissertation Research: Dye Sensitized Solar Cells
Graduate Research Assistant **2012 – 2014**
Advisor: Dr. Gerald J. Meyer
Fundamental electron transfer processes key to understanding and optimizing the performance of DSSCs were studied using transient absorbance spectroscopy, electronic spectrophotometry, photoluminescence spectroscopy, time-dependent photoluminescence spectroscopy, incident photon-to-current efficiency measurements, surface and solution electrochemistry, and surface and solution spectroelectrochemistry.

New College of Florida, Sarasota, FL
Thesis Research in Bioinorganic Chemistry

Thesis Research Student **2010 – 2011**
Advisor: Dr. Suzanne E. Sherman
Synthesis of the target structural and potentially catalytic small molecule model of the manganese-containing active sites of oxalate oxidase and/or oxalate decarboxylase. The target complex was $[Mn(H_2O)_2(R_2TCMA)]^+$ where R_2TCMA is 1,4-diR-1,4,7- triazacyclononane-N-acetate and R = isopropyl or benzyl. The penultimate step in ligand synthesis was realized. The many synthetic intermediates were each characterized by ^{1}HMNR,^{13}CNMR, FTIR, and in some cases elemental analysis. A comprehensive thesis was written.

University of Minnesota, Minneapolis, MN
Lando/NSF Summer Research Program
Research Student **June 2010 – August 2010**
Advisor: Dr. William B. Tolman
Synthesis of a novel ligand for use in a Nitrous Oxide Reductase model complex. Experience with anaerobic techniques using Schlenk manifold and glove box.

University of Florida, Gainesville, FL
Research in Neurology for Young Students
Research Volunteer **June 2009 – August 2009**
Advisor: Dr. Firas H. Kobeissy
Collaborative work employing LC-MS and gel electrophoresis on trypsin digests of the protein extracts of heart and cortex tissues of mice to discover that creatine kinase is upregulated as a result of regular exposure to cigarette smoke.

New College of Florida, Sarasota, FL
"The Ecology of Extreme Environments; Ethnobotany in the Amazon"
Independent Study Project Student **January 2008**
Advisor: Drs. Margaret "Meg" D. Lowman and Elzie McCord, Jr.
Field work in the Amazon Rainforest of Northern Perú utilizing the canopy walkways and other research facilities of Explorama Lodges to gather and analyze leaf samples for Dr. Lowman's longitudinal study of insect herbivory.

RELATED EXPERIENCE

American Institute of Physics Publishing, Melville, NY
Assistant Journal Manager **July 2015**

Gordon Research Conferences
Gordon Research Seminar on Photochemistry 2015, Easton, MA
Associate Chair **2015**

American Journal Experts
Chemistry and Materials Science
Contract Editor **2015 – present**

Science Writing and Communication Club – UNC-CH
The PipettePen, science blog
Editor in Chief **2015 – present**

AFFILIATIONS

UNC-CH Science Writing and Communication Club	**2015 - present**
UNC-CH Science Education and Policy Society	**2014 - present**
UNC-CH Science Policy Advocacy Group	**2014 - present**
American Physical Society	**2014 - present**
Association for Women in Science	
The Electrochemical Society	**2014 - present**
American Chemical Society	**2010 - present**

PUBLICATIONS

Brigham, E. C.; Meyer, G. J. Ostwald Isolation to Determine the Reaction Order for $TiO_2(e^-)|S^+ \rightarrow TiO_2|S$ Charge Recombination at Sensitized TiO_2 Interfaces. *J. Phys. Chem. C.* **2014**, *118,* 7886–7893.

Achey, D.; **Brigham, E. C.**; DiMarco, B. N.; Meyer, G. J. Excited State Electron Transfer after Visible Light Absorption by the Co(I) State of Vitamin B_{12}. *Chem. Commun.* **2014**, *50,* 13304-13306.

Brigham, E. C.; Achey, D.; Meyer, G. J. Excited State Electron Transfer from Cobalt Coordination Compounds Anchored to TiO_2. *Polyhedron* **2014**, *82*, 181-190.

Brigham, E. C. TACN and Jibing toward Synthetic Models of Oxalate Degrading Metalloenzymes, New College of Florida: Sarasota, FL, USA, **2011**.

SELECTED PRESENTATIONS

Brigham, E. C.; *Electron Transfer Reactions in the Dye-Sensitized Solar Cell: Kinetics and Mechanisms*
Oral Presentation, Scudderfest: 35 Years of Advances in Chemistry and Chemical Education, a symposium in honor of Prof. Paul H. Scudder, Sarasota, FL 2015

Brigham, E. C.; Meyer, G. J.; *Ostwald Isolation to Determine the Rate Law of Interfacial Charge Recombination in a DSSC Model System*
Poster, Applied Functional Materials Chemistry Conference, Thuwal, Saudi Arabia 2014

Brigham, E. C.; Meyer, G. J.; *Determining the reaction order for $TiO_2(e^-)|S^+ \rightarrow TiO_2|S$ charge recombination at sensitized TiO_2 interfaces with Ostwald Isolation.*

Paper orally presented at 248th ACS National Meeting,
San Francisco, CA 20785 2014

Brigham, E. C.; Meyer, G. J.; *Ostwald Isolation to Determine the Rate Law of Interfacial Charge Recombination in a DSSC Model System.*
Poster, Gordon Research Conference & Seminar:
Electron Donor-Acceptor Interactions, *Newport, RI.* 2014

Brigham, E. C.; *Recent Advances in Photoelectrochemical Reduction of* CO_2 *for Solar Fuel*
Presentation at Johns Hopkin University Chemistry
Seminar, Baltimore, MD 2013

Brigham, E. C.; Pistner, A. J.; Rosenthal, J.; Meyer, G. J.; *Near-Infrared Sensitization of* TiO_2 *with a Novel Organic Sensitizer*
Poster, Gordon Research Conference & Seminar:
Photochemistry, Easton, MA 2013

Brigham, E. C.; Achey, D.; Meyer, G. J.; *Photoelectrocatalysis on* TiO_2 *Nanocrystalline Films: Cobalt Porphyrin Reactivity with Alkyl Halides and Hydrohalic Acid.*
Poster, Gordon Research Conference & Seminar:
Electron Donor-Acceptor Interactions, Newport, RI. 2012